Doklady Physics, Vol. 46, No. 9, 2001, pp. 609–611. Translated from Doklady Akademii Nauk, Vol. 380, No. 1, 2001, pp. 31–33.

PHYSICS

A Generalized Kargin–Slonimskiĭ–Rouse Model for Oligomeric Chains

V. I. Irzhak

Presented by Academician V.B. Timofeev March 17, 2001

Received April 12, 2001

The Kargin–Slonimskiĭ–Rouse model is often used for the description of the relaxation behavior of polymers [1, 2]. A chain whose links are modeled by identical Maxwell elements (according to their properties) is assumed to be sufficiently long. Therefore, the discrete system of differential-difference equations describing the chain displacement $\mathbf{x}_i$ is represented in the continuous form [3, 4] as a single equation in partial derivatives of the second order. It is evident that this approach is unsuitable for short chains, and in order to solve a problem involving a relatively small number of equations it is necessary to take into account the relaxation of end chains in explicit form. In addition, the generalization of the model necessitates the admission of an arbitrary distribution of relaxation characteristics for chain links. The solution to this problem is the goal of the present paper.

Let an *i*th link be characterized by the relaxation time τ_i.

In this case, the relaxation of a system containing n links and removed from the equilibrium state by a force F applied to the first link is described by the following system of $n + 1$ equations:

$$\begin{aligned}
\tau_1\dot{F} &= -\mathbf{F} + \mathbf{E}(x_1 - x_2),\\
\tau_1\dot{x}_1 &= \frac{\mathbf{F}}{\mathbf{E}} - x_1 + x_2,\\
\tau_2\dot{x}_2 &= x_1 - 2x_2 + x_3,\\
&\cdots\\
\tau_i\dot{x}_i &= x_{i-1} - 2x_i + x_{i+1},\\
&\cdots\\
\tau_n\dot{x}_n &= x_{n-1} - x_n.
\end{aligned} \tag{1}$$

Here, **E** is the elasticity modulus for a Maxwell element. We suppose, for simplicity, that this quantity is the same for all links, whereas their difference in relaxation times is caused by the difference in their friction coefficients, i.e., the interaction of these links with matter.

The solution to the system of equations (1) in the form of a combination of exponential functions

$$F = F_0\sum_{i=1}^{n} h_i \exp\{-\mathbf{p}_i t\}$$

is determined by the roots of the polynomial [5]:

$$D_n = \begin{vmatrix}
z_1-2 & 1 & 0 & 0 \ldots 0 & 0 & 0\\
1 & z_2-2 & 1 & 0 \ldots 0 & 0 & 0\\
0 & 1 & z_3-2 & 1 \ldots 0 & 0 & 0\\
\cdots & & & & & \\
0 & 0 & 0 & 0 \ldots 1 & z_{n-1}-2 & 1\\
0 & 0 & 0 & 0 \ldots 0 & 1 & z_n-1
\end{vmatrix} = 0. \tag{2}$$

It is easy to obtain the numerical solution to Eq. (2) on the basis of the fact that the determinant D_n can be represented in the form of the recurrence series

$$\begin{aligned}
D_1 &= z_n - 1,\\
D_2 &= (z_{n-1} - 2)D_1 - 1,\\
D_3 &= (z_{n-2} - 2)D_2 - D_1,\\
&\cdots\\
D_i &= (z_i - 2)D_{i-1} - D_{i-2},\\
&\cdots\\
D_n &= (z_1 - 2)D_{n-1} - D_{n-2}.
\end{aligned} \tag{3}$$

The solution of the equation $D_n = 0$ makes it possible to find n roots $\mathbf{p}_1, \mathbf{p}_2, \ldots, \mathbf{p}_n$. These roots correspond to inverse values of relaxation times that characterize the relaxation behavior of the system as a whole.

As an example, the results of the analysis of the relaxation spectrum for oligomeric chains with a length of 10 are given in Table 1. Chains were considered

Institute for Problems of Chemical Physics, Russian Academy of Sciences, Institutskaya ul., Chernogolovka, Moscow oblast, 142432 Russia

1028-3358/01/4609-0609$21.00

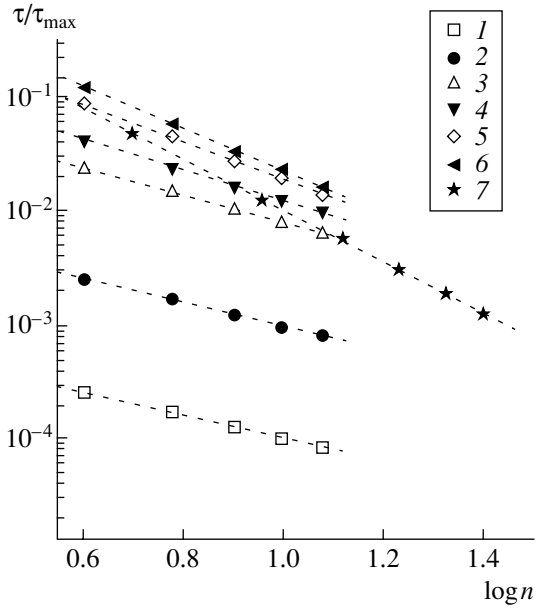

Fig. 1. Maximum relaxation time $\tau\mathbf{p}_1$ as a function of the chain length: (*1*–*6*) chains with an **a**-type end link; (*7*) chains with a block structure. The relaxation times τ_1/τ of the **a**-type links are: (*1*) 1000; (*2*) 100; (*3*, *7*) 10; (*4*) 5; (*5*) 2; and (*6*) 1.

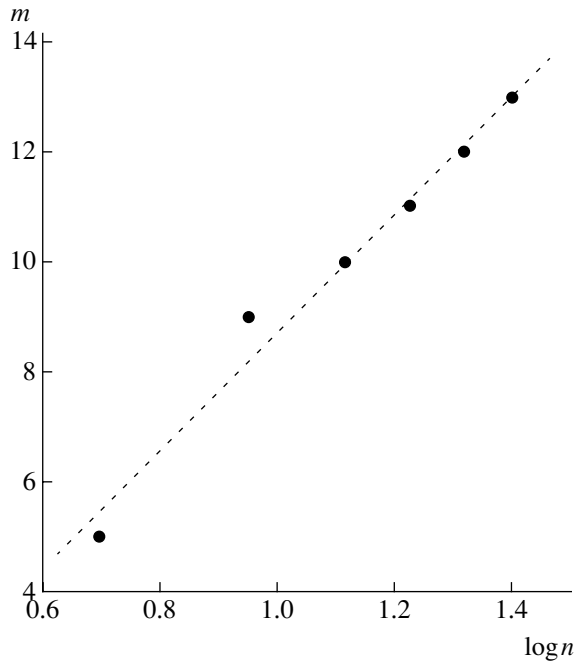

Fig. 2. Correlation between the chain length *n* and the mode number *m*.

whose end links (of the **a** type) are featured by relaxation times τ_1 and τ_n, whereas the others (of the **b** type) are characterized by the relaxation time τ.

As is seen from the data presented in Table 1, an increase in τ_1 and τ_n is accompanied by a considerable rise in the maximum relaxation time (a decrease in $\mathbf{p}_1$). In this case, the value of the maximum relaxation time is weakly dependent on whether one or both chain ends are modified; although the first link directly subjected to the action of the applied force has a weaker influence than the end one. The modification of the second end leads to a sharp increase (in its magnitude) in the second relaxation time (i.e., to a decrease in $\mathbf{p}_2$). The other

Table 1. Relaxation properties of oligomeric chains ($n = 10$) as functions of the oligomeric properties of end links τ_1/τ and τ_n/τ

τ_n/τ	τ_1/τ	$\tau\mathbf{p}_1$	$\tau\mathbf{p}_2$	$\tau\mathbf{p}_3$	$\tau\mathbf{p}_4$	$\tau\mathbf{p}_5$	$\tau\mathbf{p}_6$	$\tau\mathbf{p}_7$	$\tau\mathbf{p}_8$	$\tau\mathbf{p}_9$	$\tau\mathbf{p}_{10}$
1	1	0.022	0.198	0.534	1.000	1.555	2.149	2.731	3.247	3.652	3.911
2	1	0.0187	0.170	0.474	0.915	1.461	2.062	2.662	3.202	3.630	3.905
5	1	0.0123	0.134	0.420	0.859	1.410	2.021	2.633	3.185	3.622	3.903
10	1	7.7×10^{-3}	0.117	0.401	0.841	1.396	2.010	2.625	3.179	3.620	3.903
100	1	9.7×10^{-4}	0.100	0.384	0.826	1.383	2.001	2.619	3.176	3.618	3.902
1000	1	1.00×10^{-4}	0.098	0.382	0.825	1.382	2.000	2.618	3.176	3.618	3.902
1	2	0.022	0.190	0.477	0.849	1.343	1.936	2.557	3.132	3.596	3.896
1	5	0.022	0.157	0.323	0.699	1.235	1.863	2.510	3.105	3.583	3.893
1	10	0.021	0.106	0.273	0.667	1.213	1.847	2.500	3.099	3.581	3.892
1	100	8.87×10^{-3}	0.030	0.243	0.647	1.198	1.836	2.492	3.094	3.579	3.892
1	1000	9.9×10^{-4}	0.0275	0.241	0.646	1.197	1.835	2.491	3.094	3.578	3.892
2	2	0.0185	0.164	0.427	0.781	1.254	1.842	2.478	3.078	3.568	3.889
5	5	0.0122	0.117	0.268	0.570	1.079	1.713	2.389	3.025	3.544	3.882
10	10	7.6×10^{-3}	0.0819	0.1838	0.513	1.036	1.681	2.367	3.012	3.538	3.881
100	100	9.6×10^{-4}	0.011	0.125	0.472	1.003	1.655	2.349	3.001	3.533	3.880
1000	1000	9.8×10^{-5}	$1.12 \cdot 10^{-3}$	0.121	0.468	1.000	1.653	2.347	3.000	3.534	3.879

relaxation times vary relatively little compared to those in the case of an unmodified chain. For the Rouse model, the maximum relaxation time as a function of the chain length is described by the law $\mathbf{p}_1 \backsim n^{-\varepsilon}$, where $\varepsilon = 2$. This dependence, however, becomes weaker with an increase in τ_n and drops to unity as seen from the data plotted in Fig. 1.

The introduction of several **a**-type links into the chain changes the entire relaxation spectrum considerably. Table 2 shows relaxation features of block-structure chains: the first and the last **a**-type links are characterized by relaxation times equal to 10τ. These links are introduced into the chain after each three links of the **b** type, which have a relaxation time τ. Thus, the chains possess a periodic structure. A chain consisting of five links has three **b**-type and two **a**-type links, while a chain consisting of nine links has six and three **b**-type and **a**-type links, respectively.

As is seen from the data presented in Table 2, with an increase in the chain length and a corresponding proportional increase in the number of **a**-type links, the maximum relaxation time rises higher than that which is characteristic of the Rouse chain: $\varepsilon = 2.26$ (Fig. 1). Relaxation times intrinsic to a minimum-size chain are present in a virtually unchanged form in longer chains. At the same time, a whole set of additional modes appears while increasing the chain length. The number of modes being featured by relatively long times increases proportionally to the number of **a**-type links introduced (from 2 to 7). At the same time, modes appear which are characterized by shorter relaxation times. In a 9-link chain, these are numbers 5, 7, and 9. In longer chains, modes with similar relaxation times arise. In a 13-link chain, these are numbers 6 and 7, 9 and 10, and 12 and 13. In a 17-link chain, three packets are present: numbers 7, 8, and 9; 11, 12, and 13; and 15, 16, and 17. The same packets are met in longer chains: 8, 9, 10, and 11; 13, 14, 15, and 16; 18, 19, and 20 in a 21-link chain; 10, 11, 12, and 13; 15, 16, 17, 18, and 19; 21, 22, and 23 in a 25-link chain; etc. The total number of modes in long chains turns out to be smaller than the number of links. Apparently, this is associated with the fact that certain modes possess relaxation times which are so close to each other that they are virtually indistinguishable. At the same time, in the case of a sufficiently rough experimental determination, modes composing a packet manifest themselves as a single mode, and the relation between the number of links and modes becomes nonlinear. Indeed, as is shown in Fig. 2, this dependence is close to a logarithmic one.

Thus, we may conclude that the consideration of chains with a nonuniform structure shows that their relaxation behavior considerably deviates from that predicted by the Kargin–Slonimskiĭ–Rouse model.

Table 2. The effect of the oligomeric-chain structure on the spectrum of relaxation times

i	$\tau\mathbf{p}_i$					
	$n = 5$	$n = 9$	$n = 13$	$n = 17$	$n = 21$	$n = 25$
1	0.0495	0.0123	0.0054	0.0030	0.0019	0.0013
2	0.112	0.081	0.044	0.026	0.017	0.012
3	0.338	0.123	0.087	0.063	0.043	0.031
4	1.631	0.318	0.125	0.089	0.073	0.056
5	3.270	0.682	0.318	0.125	0.090	0.079
6		1.628	0.636	0.318	0.125	0.091
7		2.055	0.718	0.615	0.318	0.125
8		3.27	1.628	0.678	0.605	0.318
9		3.43	2.028	0.733	0.651	0.599
10			2.080	1.628	0.702	0.633
11			3.27	2.017	0.740	0.677
12			3.42	2.054	1.628	0.717
13			3.44	2.091	2.011	0.745
14				3.27	2.038	1.628
15				3.42	2.070	2.008
16				3.43	2.096	2.028
17				3.44	3.27	2.054
18					3.425	2.080
19					3.435	2.098
20					3.442	3.269
21						3.430
22						3.438
23						3.443

REFERENCES

1. V. A. Kargin and G. L. Slonimskiĭ, Dokl. Akad. Nauk SSSR **62**, 239 (1948).
2. P. E. Rouse, J. Chem. Phys. **21**, 1272 (1953).
3. A. Yu. Grossberg and A. R. Khokhlov, *Statistical Physics of Macromolecules* (Nauka, Moscow, 1989).
4. M. Doi and S. Edwards, *Theory of Polymer Dynamics* (Clarendon Press, Oxford, 1986; Mir, Moscow, 1998).
5. E. Kamke, *Differentialgleichungen. Lösungsmethoden und Lösungen*, Bd. 1: *Gewöhnliche Differentialgleichungen* (Geest and Portig, Leipzig, 1959; Fizmatgiz, Moscow, 1961).

Translated by G. Merzon

Doklady Physics, Vol. 46, No. 9, 2001, pp. 612–614. Translated from Doklady Akademii Nauk, Vol. 380, No. 2, 2001, pp. 176–178.

PHYSICS

Flicker-Noise in a Jet of Superheated Liquid

A. V. Reshetnikov, N. A. Mazheĭko, Corresponding Member of the RAS V. P. Koverda, V. N. Skokov, Academician V. P. Skripov, and A. A. Uĭmin

Received April 10, 2001

Fluctuations play a substantial role in the relaxation of a metastable boiling-up fluid. Usual thermal fluctuations in a molecular system initiate the nucleation of vapor bubbles. The nucleation process is irreversible. It arises against the background of stationary white noise. The following growth of vapor bubbles can introduce new features into the nature of the fluctuation process.

Homogeneous nucleation has a threshold nature [1]. The subsequent growth of the vapor phase proceeds very fast. This makes it possible to observe the boiling-up of a superheated liquid even in the case of a high space–time concentration of the phase transition, in particular, when the jet flows though a short channel [2, 3]. In this channel, the thermodynamically nonequilibrium flow of a boiling-liquid jet is realized. Under conditions of intense homogeneous nucleation, critical locking of the channel occurs. The jet shape beyond the channel end varies depending on the degree of the superheating of the fluid [3]. Under high superheating, the observed flow instability manifests itself in the jet-shape fluctuations.

The intense fluctuation boiling-up of the superheated-fluid jet can be considered as a peculiar crisis in the flow, which is somewhat similar to the heat-transfer crisis associated with the passage from nucleate boiling to film boiling. In [4, 5], it was experimentally shown that in the case of the crisis of water boiling in a vertical-wire heater, intense thermal fluctuations with the spectral power inversely proportional to the frequency (flicker noise) occur. The flicker noise ($1/f$ noise) found in [4, 5] is associated with nonequilibrium phase transitions in the system.

As was shown theoretically in [6–9], the origin of the $1/f$ noise may be caused by the superimposition and interaction of two nonequilibrium phase transitions. If white noise exists in a system, this interaction can lead to a self-organization of the critical state of the system that manifests itself in the divergence of the spectral characteristics of the fluctuations.

Institute of Thermal Physics, Ural Division, Russian Academy of Sciences, ul. Amundsena 106, Ekaterinburg, 620016 Russia

In addition to the boiling crisis modes, flicker-noise was also found experimentally in other nonequilibrium phase transitions, in particular, in combustion [10] and in arc discharge [11]. The intense fluctuation boiling of the superheated-liquid jet can also be considered a nonequilibrium phase transition.

In this study, we experimentally investigate phase transitions in a superheated liquid and reveal conditions for the appearance of the flicker noise.

Our experiments were carried out using a laboratory setup that provided a steady outflow of a superheated liquid into the atmosphere for several tens of seconds. The working chamber was a cylindrical steel vessel with a volume of 600 cm^3 and with an electric heater wound around it. In these experiments, we used a short cylindrical channel with a diameter of 0.5 mm and a length of 0.7 mm. As a working liquid, we used Freon-11, which has a low boiling temperature (23°C). The initial pressure in the chamber varied along the saturation curve within the temperature range $50 \le T_0 \le 165$°C and the pressure range $0.24 \le P_0 \le 2.78$ MPa. Significant superheating in the flow was attained by using short channels in which high pressure-drop rates (on the order of 10^6 MPa/s) are realized.

In [3], the jet shape for boiling-up superheated water was investigated. The jet shape of superheated Freon-11 passed through the same stages of evolution as the water jets. For low initial parameters, no boiling-up occurred and the jet shape was close to the cylindrical one. As the initial temperature (and pressure) increased, isolated occurrences of boiling-up were observed in the jet. Beginning from the temperatures $T_0 \ge 90$°C (and the corresponding pressures $P_0 \ge 0.66$ MPa), the principal factor influencing the jet shape was intense bulk boiling. The boiling-up occurred beyond the channel outlet. In this case, the jet had a hollow-cone shape. At the temperature $T_0 \ge 150$°C, the boiling-up mechanism changed. At these temperatures, the boiling-up was distinguished by a higher intensity and concentration (explosive boiling-up). Explosive boiling-up with a predominantly homogeneous nucleation mechanism leads to the shifting of the cross section of intense vaporization towards the channel interior. In this case, the jet shape was almost parabolic.

1028-3358/01/4609-0612$21.00

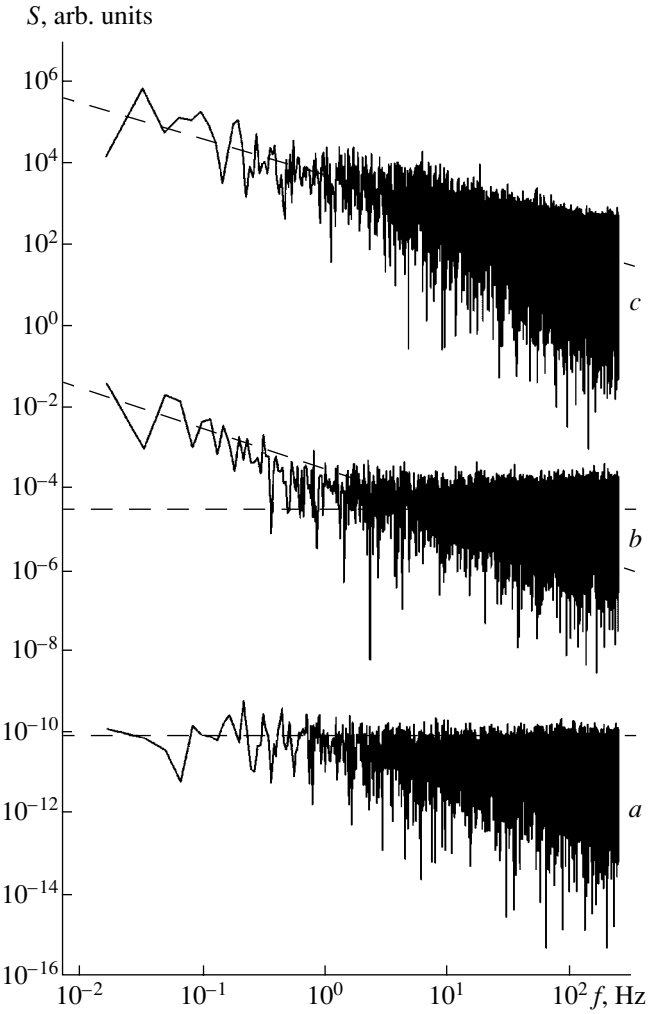

Fig. 1. Fluctuation-power spectra for the boiling-up of a superheated Freon-11 jet: (*a*) cold jet; (*b*) boiling-up beyond the channel outlet; (*c*) explosive boiling-up in the channel.

The boiling-jet shape fluctuated severely. In this study, the fluctuations were investigated using transmitted laser radiation photometry. A laser beam with an $\simeq$1 mm diameter and with an laser-radiation wavelength of 0.65 μm was transmitted through the jet of the outflow liquid. The laser-beam intensity was measured using an FD256 photodiode with a sensitivity of 0.5 A/W. Signals were digitized by a 12-bit analog-to-digital converter and read out to the personal-computer memory. The photocurrent fluctuations were measured when the beam was transmitted through various jet sections at a distance of 0 to 10 mm from the boiling spot. The results presented below are virtually independent of the choice of the distance.

Using the fast Fourier transform method for data processing, we found the fluctuation-power spectra. In the case of the outflow of a cold jet ($T_0 \le 90$°C), the fluctuation-power spectrum had the shape of white noise with a uniform frequency distribution for the fluctuation intensity. This spectrum is shown in Fig. 1*a*.

By increasing the initial temperature and with the onset of bulk boiling-up, we observed an increase in the low-frequency spectral component in the jet (Fig. 1*b*). In the low-frequency region, the frequency dependence of the fluctuation-power spectral density was close to $1/f$. With an increase in the temperature T_0 in the chamber, the intense-boiling spot (the cone vertex) approached the channel outlet. In this case, the boundary of the transition from white noise to $1/f$ behavior was shifted towards higher frequencies; in other words, the frequency range for the flicker noise broadened. At temperatures $T_0 \ge 150$°C and under explosive-boiling conditions for the superheated liquid, the flicker-noise was observed in the channel with the frequency variation extended over a range of more than four orders of magnitude (Fig. 1*c*). In Fig. 2, we show a typical pattern

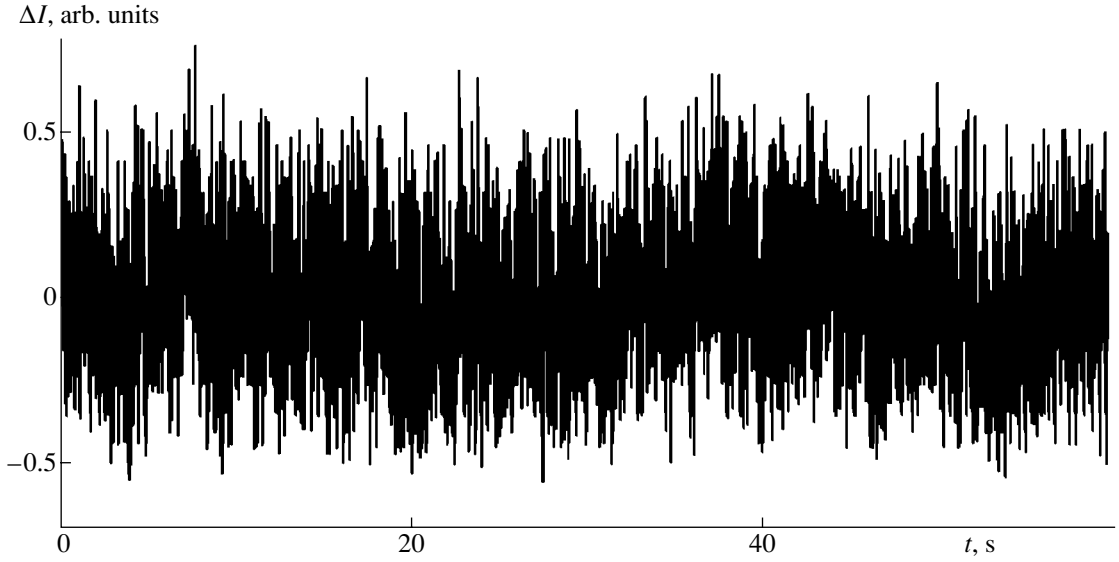

Fig. 2. Fluctuations of the transmitted laser-radiation intensity in the case of the boiling-up of a superheated Freon-11 jet.

of photocurrent fluctuations in the channel wherein the broadband flicker-noise was observed under explosive boiling-up conditions. The lower limit of the flicker-noise was restricted by the time of the steady outflow of fluid (i.e., by the chamber sizes).

Thus, we experimentally observed fluctuations in the boiling-up of superheated-liquid jets. The power spectrum of these fluctuations varies according to the $1/f$ law. The presence of flicker-noise implies the possibility of large-scale catastrophic ejections in the system. These catastrophic ejections arise as a result of energy transfer from high-frequency degrees of freedom to low-frequency ones. The flicker noise found is induced by the nonequilibrium phase transitions in superheated-fluid jets, which are associated with explosive boiling-up.

ACKNOWLEDGMENTS

This work was supported by the Russian Foundation for Basic Research, projects nos. 00-02-16288 and 00-15-96719.

REFERENCES

1. V. P. Skripov, *Metastable Liquid* (Nauka, Moscow, 1972).
2. N. A. Shuravenko, O. A. Isaev, and V. P. Skripov, Teplofiz. Vys. Temp. **13**, 896 (1975).
3. A. V. Reshetnikov, N. A. Mazheĭko, and V. P. Skripov, Prikl. Mekh. Tekh. Fiz. **41**, 125 (2000).
4. V. N. Skokov, V. P. Koverda, and A. V. Reshetnikov, Pis'ma Zh. Éksp. Teor. Fiz. **69**, 590 (1999) [JETP Lett. **69**, 636 (1999)].
5. V. N. Skokov, A. V. Reshetnikov, and V. P. Koverda, Teplofiz. Vys. Temp. **38**, 786 (2000).
6. V. P. Koverda, V. N. Skokov, and V. P. Skripov, Zh. Éksp. Teor. Fiz. **113**, 1748 (1998) [JETP **86**, 953 (1998)].
7. V. P. Koverda and V. N. Skokov, Physica A (Amsterdam) **262**, 376 (1999).
8. V. P. Koverda, V. N. Skokov, and V. P. Skripov, Dokl. Akad. Nauk **356**, 614 (1997) [Phys. Dokl. **42**, 532 (1997)].
9. V. N. Skokov and V. P. Koverda, Pis'ma Zh. Tekh. Fiz. **26** (20), 13 (2000) [Tech. Phys. Lett. **26**, 900 (2000)].
10. A. V. Reshetnikov, A. V. Vinogradov, V. P. Koverda, and V. N. Skokov, Dokl. Akad. Nauk **374**, 481 (2000) [Dokl. Phys. **45**, 515 (2000)].
11. V. N. Skokov, V. P. Koverda, and A. V. Reshetnikov, Zh. Éksp. Teor. Fiz. **119**, 535 (2001) [JETP **92**, 535 (2001)].

Translated by V. Bukhanov

Doklady Physics, Vol. 46, No. 9, 2001, pp. 615–618. Translated from Doklady Akademii Nauk, Vol. 380, No. 2, 2001, pp. 179–182.

PHYSICS

The Polarization of a Radio-Frequency Electromagnetic Field in Lanthanum Manganite

Corresponding Member of the RAS V. V. Ustinov*, A. P. Nosov*, A. B. Rinkevich*, and V. G. Vasil'ev**

Received April 27, 2001

The effect of the rotation of a polarization plane and the ellipticity of electromagnetic waves have become powerful tools in the investigation of magneto-ordered media. They can be used, in principle, for studying the spectra of both spin and magnetostatic waves, for determining the dielectric and magnetic dynamic tensors, and for establishing general relations between the polarizability and magnetization of a medium [1]. In the optical range, as a rule, such investigations are carried out in transparent media that also have a large quantity of magneto-optic properties. Usually, the skin depth in a sample is significantly larger than its thickness.

Under the doping of a conducting ferromagnetic oxide (e.g., lanthanum manganite), its conductivity and Curie temperature in the radio-frequency range may be altered significantly and, thus, the relationship between the skin depth and the thickness of a sample may be arbitrary. Because of the colossal magneto-resistance effect, the doped lanthanum manganites have become a subject of thorough investigation [2]. Electromagnetic properties of this class of compounds are being intensively studied in the microwave range [3–5]. The practical applications of the electromagnetic properties of lanthanum manganites in this range were considered in [6].

In this work, we study features of electromagnetic field transmission through lanthanum manganites. At low frequencies in the range under consideration, the skin depth in a sample is much greater than its thickness, whereas at frequencies of tens of MHz, it is approximately equal to, or less than, the thickness. We carried out the experiments at frequencies that are much less than the ferromagnetic resonance and antiresonance frequencies. Therefore, the features of transmitting the radio-frequency electromagnetic field were determined by domain-wall displacements and the rotation of the magnetization vector. For doped manganites, the description of the field transmission becomes more complicated because of the presence of a granular structure and the spatial nonuniformity of conductivity. The experiments were carried out in a layout corresponding to the Cotton–Mouton effect. Unlike the usual conditions for observing this effect in magneto-polarized media [1], the real and imaginary components of the wave number in a conducting manganite are of the same order of magnitude. In principle, it was possible to observe both the magneto-optic effect and the dichroism.

A magnetic field was generated and recorded by exciting and receiving coils, which were on both sides of a thin plate made of a manganite. The coil axis and, hence, the variable magnetic field vector $\mathbf{H}_\sim$ lay in the plane of the plate. In addition, a constant magnetic field $\mathbf{H}$ parallel to this plane was applied. The wave number $\mathbf{k}$ and the constant magnetic field were always mutually perpendicular; thus, the layout of the Cotton–Mouton effect was realized. The amplitude of the applied constant magnetic field was always sufficiently large ($|\mathbf{H}| \gg |\mathbf{H}_\sim|$). Therefore, the magnetic state of the sample was determined by the field $\mathbf{H}$. By rotating the axis of the receiving coil, we determined the polarization of the radio-frequency magnetic field transmitted through the plate under investigation.

The original powders of manganites with the nominal composition $La_{0.63}Y_{0.07}Ba_{0.30}MnO_3$ were prepared by coprecipitation from solutions. The samples of bulk polycrystalline manganites were obtained by a 6-hour heat treatment of the pressed powders in an oxygen flow at a temperature of 1200°C. The density of the samples obtained was 60% of the roentgen one, and the Curie temperature was equal to 346 K. At $T = 293$ K, the specific resistance was 1.5 Ω cm and the relative magnetoresistance in the magnetic field $\mathbf{H} = 10$ kOe was –5.7%. In the experiments, we used manganite plates with a thickness of $d = 0.54$ mm. At a frequency of $f = 1$ MHz and magnetic permeability of $\mu = 1$, we evaluated the skin depth δ_1, which turned out to be 0.8 mm. The experiments were carried out in the frequency range from 20 kHz to 60 MHz.

* *Institute of Physics of Metals, Ural Division, Russian Academy of Sciences, ul. S. Kovalevskoĭ 18, Ekaterinburg, 620219 Russia*

** *Institute of Solid-State Chemistry, Ural Division, Russian Academy of Sciences, ul. Pervomaĭskaya 91, Ekaterinburg, 620219 Russia*

1028-3358/01/4609-0615$21.00

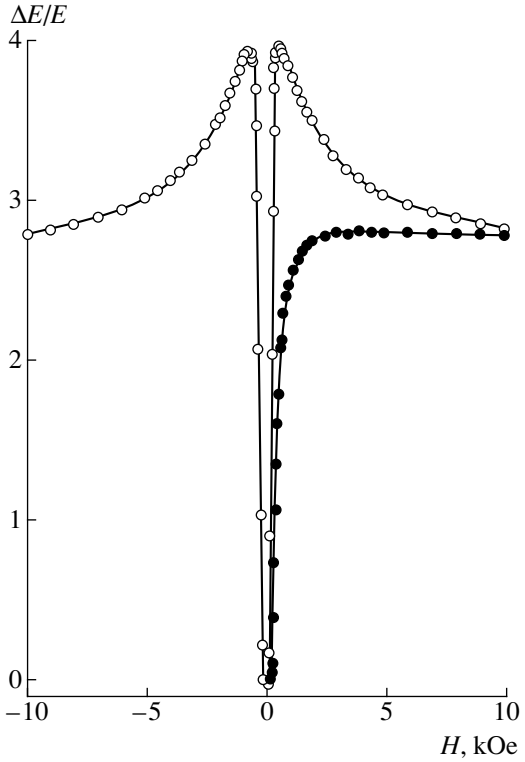

Fig. 1. Transmission of the electromagnetic field at the frequency of 30 MHz through a plate made of lanthanum manganite. Open and filled circles denote the transmission coefficients for $\mathbf{H} \parallel \mathbf{H}_\sim$ and $\mathbf{H} \perp \mathbf{H}_\sim$, respectively.

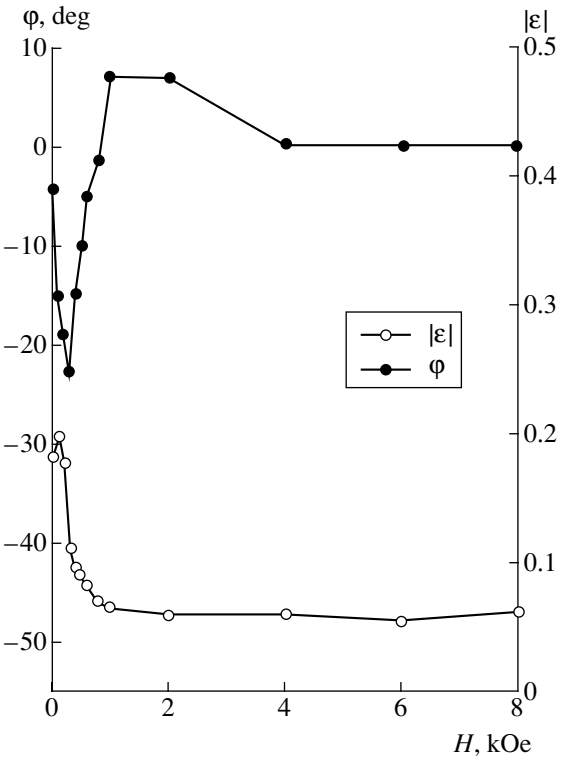

Fig. 2. Ellipticity ε and the Faraday rotation angle φ for the variable electromagnetic field $\mathbf{H}_\sim$ making the angle θ = −45° with the constant external magnetic **H** (f = 20 MHz).

In general, a sufficiently strong magnetic field leads to a significant increase (up to ten times) in the amplitude of the transmitted electromagnetic field. Figure 1 shows the relative change in the electromotive force (EMF), $\frac{\Delta E}{E} = \frac{E(H) - E(0)}{E(0)}$, measured in the receiving coil as a function of the magnetic field strength at $\mathbf{H}_\sim \perp \mathbf{H}$ and $\mathbf{H} \parallel \mathbf{H}_\sim$. Here, $E(H)$ and $E(0)$ are the values of EMF in the receiving coil with and without the magnetic field **H**, respectively. In the case of $\mathbf{H}_\sim \perp \mathbf{H}$, EMF was observed to increase monotonically with **H** up to the saturation field. In the case of $\mathbf{H} \parallel \mathbf{H}_\sim$, the dependence of $\frac{\Delta E}{E}$ measured at a frequency of 30 MHz has its maximum at field strengths approximately equal in magnitude to the anisotropy field strength; beyond this, the EMF value slowly decreases. This dependence is even with respect to the direction of the applied magnetic field with an insignificant hysteresis.

The experimental dependences of the Faraday rotation angle φ and the ellipticity ε on the external magnetic field strength are shown in Fig. 2. The ellipticity was defined as the ratio of the small and large semiaxes of the polarization ellipse for the transmitted electromagnetic field. These experimental results were obtained at a frequency of f = 30 MHz, with the angle θ between the exciting-coil axis and **H** equal to −45°. It is observed that most changes in polarization occur in fields less than 1 kOe, with |ε| and φ amounting to ~−0.2 and ≈–24°, respectively. In stronger near-saturation fields, the Faraday rotation angle is close to zero and the ellipticity decreases considerably.

We now introduce a field transmission coefficient for the plate, $D = \frac{\dot{H}_\sim^{\text{out}}}{\dot{H}_\sim^{\text{in}}}$, where $\dot{H}_\sim^{\text{in}}$ and $\dot{H}_\sim^{\text{out}}$ are complex amplitudes of the fields leading into and coming out of the plate, respectively. EMF in a coil is $E \sim \omega \dot{H}_\sim^{\text{in}} |\mathbf{D}| wS$, where S and w are the cross section and the number of turns in the coil, respectively, and $\omega = 2\pi f$. Provided that $\mathbf{H} \perp \mathbf{k}$, two waves whose field strengths are determined by the skin effect are normal modes. For the first mode, the variable magnetic field vector is parallel to the external magnetic field vector, $\mathbf{H}_\sim \parallel \mathbf{H}$; for another mode, it is perpendicular the later, $\mathbf{H}_\sim \perp \mathbf{H}$. For the transmission coefficients of these waves, $D_{\parallel,\perp}$, we have [7]

$$D_{\parallel,\perp} = |D_{\parallel,\perp}| e^{i\phi_{\parallel,\perp}} = \frac{2(1+i)}{Z\sigma_{\parallel,\perp}\delta_{\parallel,\perp}} \times \frac{1}{\sinh t_{\parallel,\perp} \cos t_{\parallel,\perp} + i \sin t_{\parallel,\perp} \cosh t_{\parallel,\perp}}. \quad (1)$$

Here, $\sigma_{\parallel,\perp}$ and $\delta_{\parallel,\perp}$ are the conductivity and the skin depth for $\mathbf{H}_\sim \parallel \mathbf{H}$ and $\mathbf{H}_\sim \perp \mathbf{H}$, respectively; $\delta_{\parallel,\perp} = (2/\omega\mu_0\mu_{rev(\parallel,\perp)}\sigma_{\parallel,\perp})^{1/2}$, $\mu_{rev(\parallel,\perp)}$ is the relative reversible permeability; $t_{\parallel,\perp} = \dfrac{d}{\delta_{\parallel,\perp}}$; and $Z = 120\pi$ is the characteristic impedance of a vacuum. Expression (1) is valid if $d \gg \dfrac{2}{Z\sigma_{\parallel,\perp}}$; this condition was satisfied in our experiments. A difference in the transmission coefficients $D_\parallel$ and $D_\perp$, which is due to anisotropy of material constants in a magnetic field, leads to a change in the polarization of the electromagnetic field because of the interference of proper waves transmitted through the plate. It can be shown that the Faraday rotation angle and the ellipticity angle $\gamma = \arctan\varepsilon$ are given by the formulas

$$\varphi = \frac{1}{2}\arctan\frac{1-\xi^2b^2-b(1-\xi^2)\cos\phi}{2\xi b\cos\phi}, \quad (2)$$

$$\gamma = \frac{1}{2}\arcsin\frac{2\xi b\sin\phi}{1+\xi^2b^2}. \quad (3)$$

Here, $b = \dfrac{|D_\parallel|}{|D_\perp|}$, $\phi = \phi_\parallel - \phi_\perp$, $\xi = \tan\theta$, and θ is the angle between the exciting-coil axis and the vector **H**. The quantities of b and ϕ entering in (2) and (3) define the dependence of the polarization of the transmitted field on the field strength.

In the extreme case of low frequencies, $t_{\parallel,\perp} \ll 1$, the relative variation in the transmission coefficient with the magnetic field is expressed in the following way:

$$\left|\frac{\Delta D_{\parallel,\perp}(H)}{D(0)}\right| = \frac{\mu_{rev}(0)}{\mu_{rev(\parallel,\perp)}(H)}\left(1+\frac{\Delta\rho_{\parallel,\perp}(H)}{\rho(0)}\right)-1, \quad (4)$$

where $\dfrac{\Delta\rho(H)}{\rho}$ is the relative magnetoresistance. Since the relative manganite magnetoresistance in the fields $H \le 10$ kOe does not exceed –5.7%, the behavior of the transmission coefficient is basically determined by the variation in the magnetic permeability with the field strength. In a sufficiently strong magnetic field, the condition $\dfrac{\mu_{rev}(0)}{\mu_{rev}(H)} > 1$ is valid. Therefore, we can expect an increase in the amplitude of the transmitted signal, which is due to varying the permeability. The different curves in the cases of $\mathbf{H}_\sim \parallel \mathbf{H}$ and $\mathbf{H}_\sim \perp \mathbf{H}$ are related to differences in the types of dynamic permeability, on which field transmission depends. According to the classification of V.K. Arkad'ev [8], the dynamic permeability in these cases is either transverse or longitudinal magnetic permeability, $\mu_{rev\perp}$ and $\mu_{rev\parallel}$, respectively. These permeabilities are not identical, because the processes of rotation make different contributions to them. In the case of $\mathbf{H}_\sim \parallel \mathbf{H}$, the contribution to magnetic permeability increases from zero at $\mathbf{H} = 0$ to the value corresponding to the anisotropy field. Further, it decreases monotonically to $\mu_{rev} \longrightarrow 1$ at saturation. Therefore, the maximum for fields of ~500–700 Oe is observed in the case of $\mathbf{H}_\sim \parallel \mathbf{H}$. For such field strengths, the difference in the transmission coefficients for the two orientations is largest, the ratio of the transmitted-field amplitudes is maximal, and the estimate $\dfrac{\mu_{rev\parallel}}{\mu_{rev\perp}} \sim 2$ is valid. From (4) and the experimental results shown in Fig. 1, it is possible to estimate the initial reversible permeability $\mu_{rev}(0)$. For $\left|\dfrac{\Delta\rho(H)}{\rho}\right| \ll 1$,

$$\left|\frac{\Delta D_\parallel(H\longrightarrow\infty)}{D(0)}\right| = \left|\frac{\Delta D_\perp(H\longrightarrow\infty)}{D(0)}\right| \approx \mu_{rev}(0)-1.$$

Hence, as follows from the data shown in Fig. 1, $\mu_{rev}(0) \approx 3.8$ at the frequency $f = 30$ MHz for $La_{0.63}Y_{0.07}Ba_{0.30}MnO_3$ manganite.

In the experiment with a transversely magnetized medium under skin-effect conditions (see Fig. 2), the polarization vector for the excited wave makes an angle $\theta = -45°$ with the external magnetic field vector. The structure of the excitation field differs from that of normal wave fields. As a result, the transformation of the polarization is similar to that in the Cotton–Mouton effect. It is worth noting that the experimental conditions for observing polarization phenomena in conducting manganites differ from those for observing the Cotton–Mouton effect in microwave and optical ranges. In the first place, the transformation of polarization is observed here for the fields whose spatial distribution is defined by the skin effect rather than by running electromagnetic waves. In this case, the real and imaginary components of the wave number are of the same order of magnitude. Secondly, since the condition $\delta_1 \gg d$ is satisfied at low frequencies in the range under consideration, the amplitude of the transmitted field basically depends on the ratio between the impedances of the ferromagnetic and the environment. Since the impedance of normal waves in a ferromagnetic is proportional to $\sqrt{\mu_{\parallel,\perp}}$, a contribution in the polarization appears, which is due to the difference in the longitudinal $\mu_\parallel$ and transverse $\mu_\perp$ permeabilities. Due to the fact that the impedance of a conducting medium preserves both the real and imaginary parts of the wave number, the interference results in both the rotation of the polarization plane and the ellipticity of the transmitted field.

Thus, in a plate made of conducting ferromagnetic lanthanum manganite and with a layout corresponding to the Cotton–Mouton effect, we observed the magneto-optic effect and dichroism, which manifested themselves in the rotation of the polarization plane and in the ellipticity of a radio-frequency field. These variations in polarization are basically caused by the anisot-

ropy of the dynamic permeability in an external magnetic field.

ACKNOWLEDGMENTS

This work was supported in part by the Russian Foundation for Basic Research.

REFERENCES

1. R. V. Pisarev, *Physics of Magnetic Dielectrics*, Ed. by G. A. Smolenskiĭ (Nauka, Leningrad, 1974).
2. É. L. Nagaev, Usp. Fiz. Nauk **166**, 833 (1996) [Phys. Usp. **39**, 781 (1996)].
3. S. Lofland, V. Ray, P. Kim, *et al.*, Phys. Rev. B **55**, 2749 (1997).
4. S. Tyagi, S. Lofland, M. Dominguez, *et al.*, Appl. Phys. Lett. **68**, 2893 (1996).
5. S. Lofland, S. Bhagat, S. Tyagi, *et al.*, J. Appl. Phys. **80**, 3592 (1996).
6. F. Owens, J. Appl. Phys. **82**, 3054 (1997).
7. R. A. Semenov, *Technical Electrodynamics* (Svyaz', Moscow, 1972).
8. V. K. Arkad'ev, *Electromagnetic Processes in Metals* (ONTI, Moscow, 1936), Part 2.

Translated by Yu. Vishnyakov

Doklady Physics, Vol. 46, No. 9, 2001, pp. 619–623. Translated from Doklady Akademii Nauk, Vol. 380, No. 3, 2001, pp. 323–327.

PHYSICS

A Model of Transverse Flame Propagation in Alternating Layers of Combustible and Inert Solid Substances

Academician A. G. Merzhanov*, P. M. Krishenik*, and K. G. Shkadinskiĭ**

Received February 9, 2001

In papers [1–3], the transverse flame propagation in a system of homogeneous combustible solid layers was theoretically analyzed while making allowance for the thermal resistance of the interfaces, under the assumption that the interfaces have no thermal inertness and that thermal gradients in the layers vanish. The authors of the works [1–3] confirmed the results of experimental study [4] concerning the existence of two limiting modes of flame propagation, which were called quasi-homogeneous and express-delivery regimes.

In this paper, we propose and numerically analyze a more general model, free from the restrictions mentioned above. The model completely describes the behavior of discrete combustion waves in heterogeneous media.[1]

We consider combustion in a system of alternating layers of combustible and inert substances (see Fig. 1). This combustion involves reaction transfer in sequential layers of the system via heat transfer. We make the following assumptions: the combustion is catalytic, the thermal properties of a combustible layer are independent of temperature and depth and may differ greatly from those of an inert layer, heat loss through the lateral surface of the system is negligible, the layers are opaque to thermal radiation, and the chemical reactions are governed by the simplest kinetic law of the first order.

We will describe the model under consideration by the following system of equations in dimensionless variables:

heat conduction and macrokinetic equations for the ith combustible layer $[(i-1)(d+\delta) < \xi < id + (i-1)\delta]$,

$$\partial_\tau \theta = \partial_{\xi\xi}\theta + \gamma^{-1}\partial_\tau \eta,$$

$$\partial_\tau \eta = (1-\eta)\exp(\theta/(1+\beta\theta)) = \gamma F(\theta, \eta);$$

heat conduction equation for the ith inert layer $[id + (i-1)\delta < \xi < i(d+\delta)]$,

$$\sigma_{c\rho}\partial_\tau \theta = \sigma_\lambda \partial_{\xi\xi}\theta;$$

thermal matching conditions,

$$\theta|_{\text{comb}} = \theta|_{\text{in}}, \quad \partial_\xi \theta|_{\text{comb}} = \sigma_\lambda \partial_\xi \theta|_{\text{in}};$$

thermal initiation conditions ($\tau > 0$, $\xi = 0$),

$$\theta = \theta_{\text{in}};$$

and initial conditions ($\tau = 0$, $\xi > 0$),

$$\theta = \theta_0, \quad \eta = 0.$$

Here, we introduce the following scale quantities and dimensionless variables:

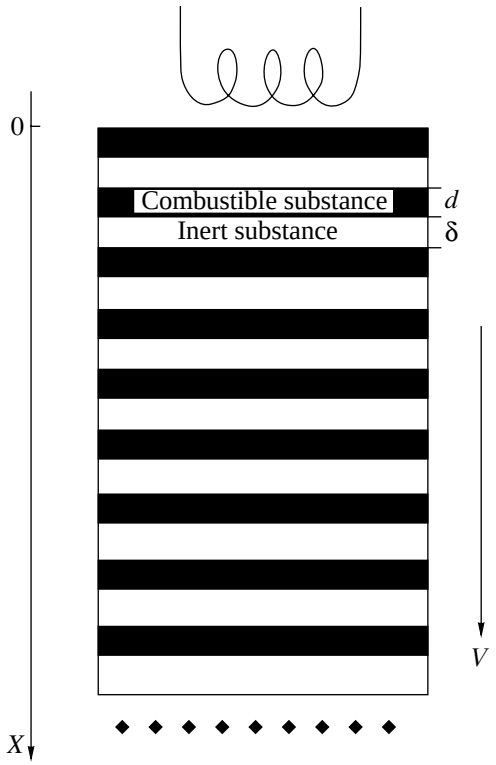

Fig. 1. Model heterogeneous system.

[1] The term "discrete combustion waves" was introduced in [5], where previous studies of this problem (see papers [1–4] and others) were generalized.

* *Institute of Structural Macrokinetics and Problems of Materials Technology, Russian Academy of Sciences, Chernogolovka, Moscow oblast, 142432 Russia*

** *Institute of Problems of Chemical Physics, Russian Academy of Sciences, Chernogolovka, Moscow oblast, 142432 Russia*

1028-3358/01/4609-0619$21.00

time $t_* = RT_*^2 k^{-1}\exp(E/RT_*)c_R/QE$,

length $x_* = [(\lambda_R/c_R\rho_R)t_*]^{0.5}$,

characteristic temperature T_*,

$$\tau = t/t_*, \quad \xi = x/x_*, \quad \theta = (T - T_*)E/RT_*^2.$$

It should be noted that there are two adiabatic temperatures in this problem, which can be chosen as T_*: the adiabatic-combustion temperature $T_{ad}^{(1)}$ for the combustible (reactive) layer,

$$T_{ad}^{(1)} = T_0 + Q/c_R,$$

and the adiabatic steady-state temperature, which is established after temperature equalization in the system of combustible and inert layers,

$$T_{ad}^{(2)} = T_0 + Q\rho_R d/(c_R\rho_R d + c_I\rho_I\delta).$$

Here, R is the gas constant; E is the activation energy; k is the pre-exponential factor; and c_R, c_I, ρ_R, ρ_I, λ_R, and λ_I are the specific heats, densities, and heat conductivity coefficients, respectively.

We use the following dimensionless parameters:

the ratio of the thicknesses of the reaction and heating zones in the combustion wave,

$$\gamma = RT_*^2 c_R/EQ;$$

the factor in the temperature dependence of the reaction rate,

$$\beta = RT_*/E;$$

the ratio of the specific heats (per unit volume) of the combustible and inert layers,

$$\sigma_{c\rho} = (c_I\rho_I)/(c_R\rho_R);$$

and the ratio of the heat conductivity coefficients of the combustible and inert layers,

$$\sigma_\lambda = \lambda_I/\lambda_R.$$

If the scale of heterogeneity of a multilayer system, $d + \delta$, tends towards zero, the system should pass into a homogeneous medium described by averaged characteristics:

$$\lambda^* = (d + \delta)\lambda_I\lambda_R/(\lambda_R\delta + \lambda_I d),$$
$$(c\rho)^* = (c_R\rho_R d + c_I\rho_I\delta)/(d + \delta).$$

The thermal diffusivity is $a = \lambda^*/(c\rho)^*$. In such a medium, the typical combustion front thickness is $L_f = a/V$, whereas the burning velocity V can be estimated according to [6]:

$$V^2 = ak\exp(-E/RT_*)RT_*^2/E(T_* - T_0).$$

Therefore, we are dealing with a multiparameter problem. The model described in [1] corresponds to the limiting case

$$\sigma_{c\rho} \longrightarrow 0 \quad \text{and} \quad (d + \delta)/L_f < 1.$$

The model under consideration describes a considerable number of new effects, the analysis of which enriches combustion theory. In this paper, we confine our consideration to only a few examples illustrating capabilities of the model.

The mathematical model represents a stiff set of partial differential equations. This set was numerically analyzed using implicit finite-difference schemes and a nonequidistant computational grid adapted to the solution.

General case. Let both thermal characteristics and sizes of the combustible and inert layers be commensurate. The commensurability of sizes of inert and fuel particles are rather common in experiments on the combustion of mixtures. This is the case, for example, under a consistent change of sizes of fuel particles, when the degree of dilution (or porosity) remains constant. Temperature profiles in the layered system under consideration at consecutive time instants are shown in Fig. 2. We see that in the steady-state combustion regime the temperature distribution in each inert–fuel pair (periods *1*, *2*, *3*, and *4* in Fig. 2) is repeated with a time lag τ_1 [1]. In this example, $\tau_1 \approx 5262$. When calculating this combustion regime, we assumed that $T_* = T_0 + Q/c_R$.

Analyzing the profiles, we come to the following conclusions:

1. Each combustible layer burns up in accordance with the frontal regime; its temperature exceeds the adiabatic temperature $T_{ad}^{(1)}$.

2. A burnt layer induces the unsteady-state heating of both fresh (sequent) and preceding (already heated) inert layers; the latter effect is due to superadiabatic temperatures.

3. Heat transfer through an inert layer leads to the heating up of the sequent combustible layer and to its ignition.

4. When the combustion front approaches the opposite surface of a combustible layer, a temperature surge (as a manifestation of the enthalpy effect [7]) can appear near this surface.

It should be noted that the reaction in a combustible layer causes its ignition only after the burning up of the preceding combustible layer. Hence, this example corresponds to the express-delivery regime of heterogeneous combustion [1, 2]. In this case, the shock-wave-front travel time for a period $(d + \delta)$ coincides, in essence, with the initiation time, whereas the combustion duration is negligible. Heat transfer becomes a determining factor depending on the structure of the heterogeneous system and the thermal properties of the medium.

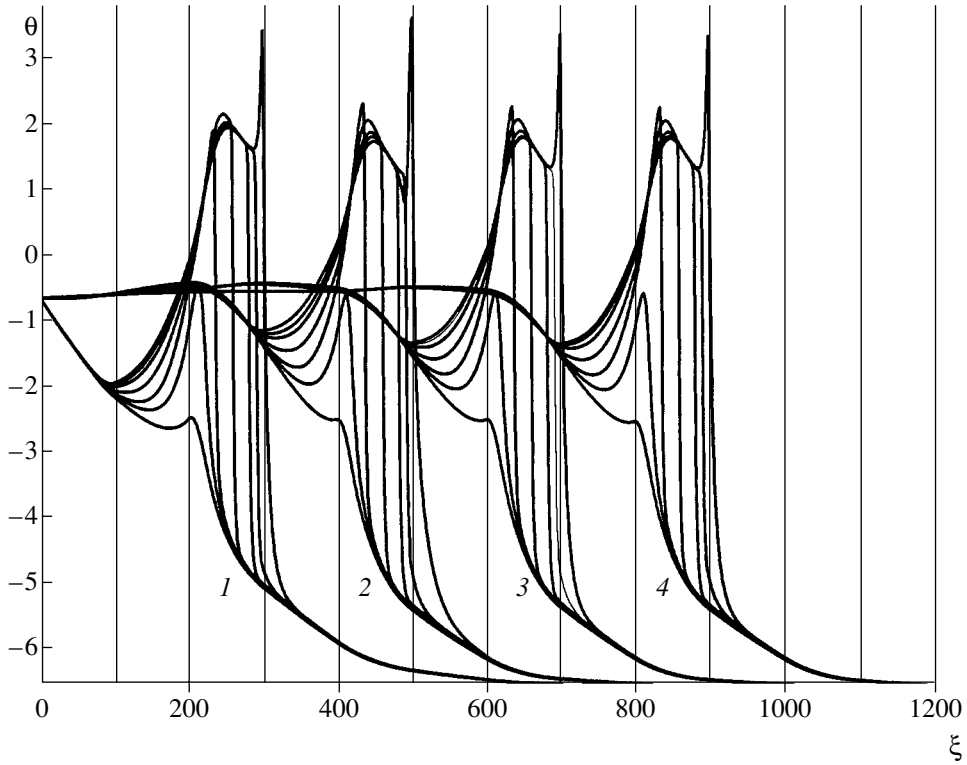

Fig. 2. Space–time distribution of temperature in the multilayer system under the express-delivery regime: $d = \delta = 100$, $\sigma_{c\rho} = 0.1$, $\sigma_\lambda = 1.0$, $\gamma = 0.1534$, $\beta = 0.118$, $\theta_0 = -6.508$, and $\theta_\infty = \theta_{ini} = -0.65$.

The case of small thermal inertness of an inert layer ($\sigma_{c\rho} \longrightarrow 0$) and a thin combustible layer ($d \ll L_f$ or $d < L_f$ and $\lambda \ll 1$). This case simulates a variant previously considered in [1–3], in which the combustion wave in a model heterogeneous system is realized (thin plates separated by gas gaps).

The calculated unsteady-state temperature profiles are shown in Fig. 3. They corroborate the validity of the accepted assumptions (the quasistationary heat transfer in gas gaps, which leads to linear temperature profiles, and the absence of a temperature spread in thin plates).

Figure 3 corresponds to the quasihomogeneous regime with $(d + \delta)/L_f \ll \gamma$. In this case, the combustion wave is similar to that in a homogeneous medium. The wave consists of a heated zone characterized by the original composition and an exothermic-reaction zone, more narrow than the former, in which the original heated reagents transform into high-temperature products. Their temperature is close to the equilibrium combustion temperature $T_{ad}^{(2)}$ {here, $T_* = T_{ad}^{(2)}$}. Characteristics of the structure and the wave velocity can approximately be derived from effective thermal and macrokinetic parameters. The heat-release function $F(\theta, \eta)$ at a fixed moment of time τ^* is also shown in Fig. 3a (the corresponding temperature distribution is marked by an asterisk). It is interesting to note that approximately three effectively reacting layers in the reaction zone are sufficient for the shock front to have a quasihomogeneous structure. The heat-release source has a bar character, because heat release is concentrated in the reacting plates. The envelope of $F(\theta, \eta)$ corresponds to the heat release in a homogeneous medium. Its translation is caused by coherent variations of $F(\theta, \eta)$ in the reacting layers.

Figure 3b presents an intermediate case (between quasihomogeneous and express-delivery regimes), $(d + \delta)/L_f \sim \gamma$. In this case, the interaction between interlayers becomes heterogeneous, and the reactive layers burn up according to the express-delivery initiation regime. The remaining layers have either burnt or have a low temperature; in the latter case, their transformation can be ignored. The propagation of the combustion wave is characterized by the relaxation oscillations of all the characteristics of the front, among them the velocity of wave propagation. In Fig. 3b, the space–time dependence of $F(\theta, \eta)$ inside two reactive layers (marked by *1* and *2*) is also shown. If the moment of the burnout of the layer preceding layer *1* is chosen as a time reference point [$\tau^n = 0$, $a_x(\eta) > 0.99$], then the profiles marked by *1* to *20* correspond to τ^n = 406.39, 442.39, 451.92, 455.59, 457.46, 458.53, 459.30, 459.93, 460.64, 462.15, 869.62, 905.62, 914.54, 918.82, 920.69, 921.15, 922.27, 922.77, 938. 48, and 925.15, respectively. It is seen that the oscillation period involves a heating stage of relatively long duration. In Fig. 3b, the corresponding space–time distribu-

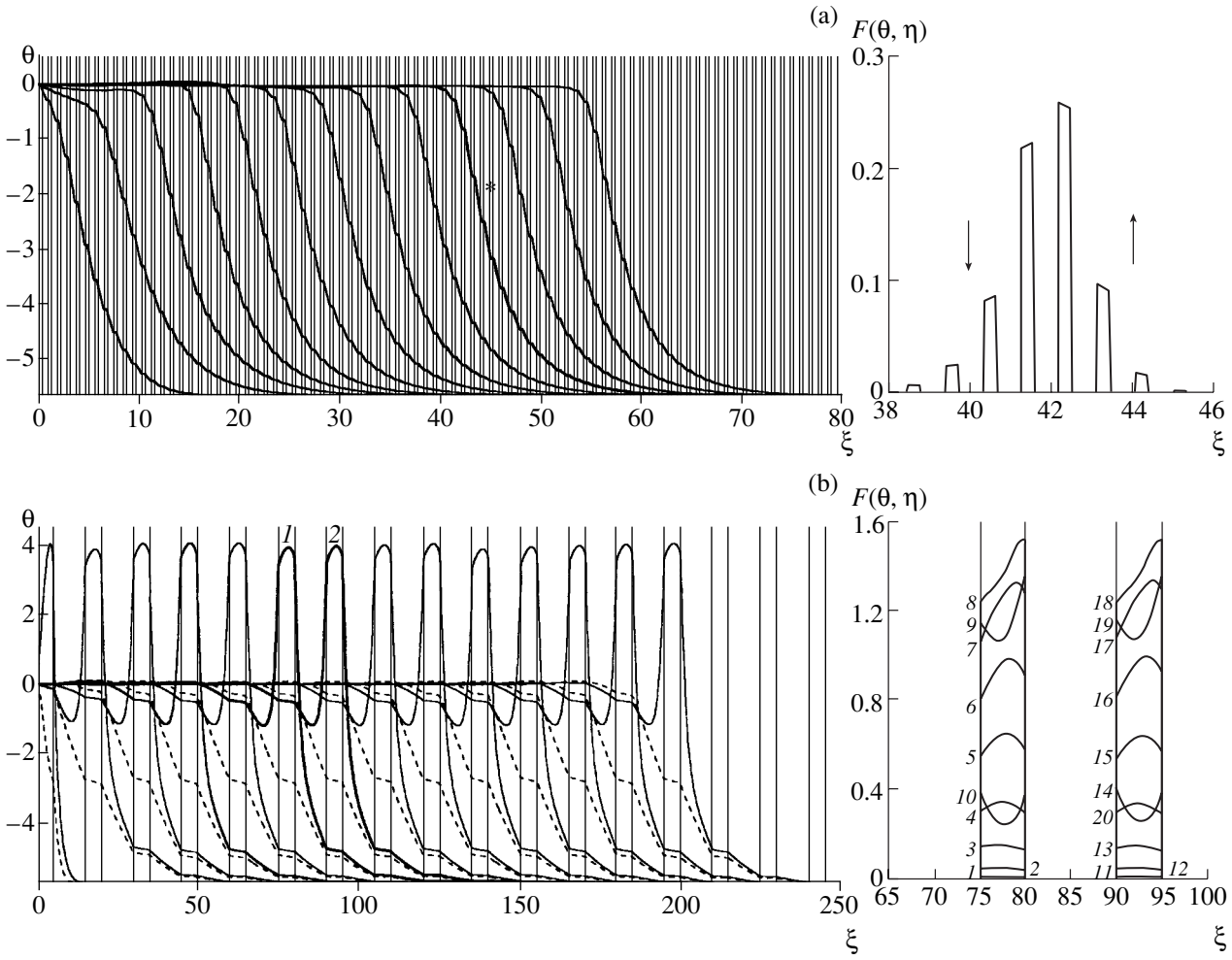

Fig. 3. Space–time distribution of temperature and the heat-release function in the multilayer system under (a) homogeneous (d = 0.3125) and (b) intermediate (d = 5) regimes: $d/\delta = 0.5$, $\sigma_{c\rho} = 0.25$, $\sigma_\lambda = 0.1$, $\gamma = 0.117$, $\beta = 0.153$, $\theta_0 = -5.67$, and $\theta_\infty = \theta_{ini} = 0$.

tion of temperature is shown by the dashed line. In this case, explosive combustion of the consecutive reactive plates occurs, and the characteristic time of heating to ignition is one tenth as long as the thermal relaxation time. The temperature of combustion products is superadiabatic. The released energy causes the original heterogeneous medium to heat up. At the same time, interlayer heat transfer occurs behind the combustion front, which results in the establishment of an equilibrium temperature of the reaction products.

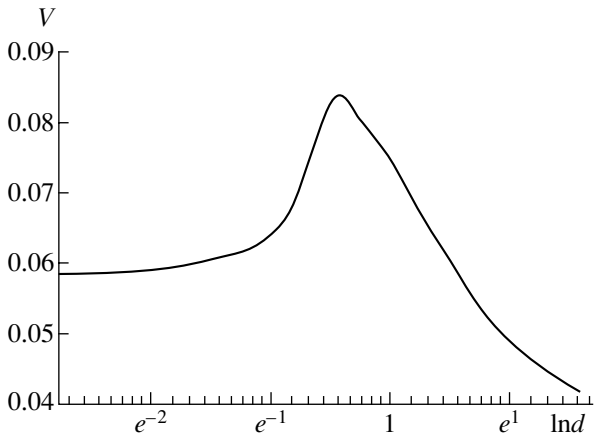

Fig. 4. Burning velocity V as a function of the scale of heterogeneity: $d/\delta = 0.5$, $\sigma_{c\rho} = 1.0$, $\sigma_\lambda = 0.1$, $\gamma = 0.117$, $\beta = 0.153$, $\theta_0 = -5.67$, and $\theta_\infty = \theta_{ini} = 0$.

Superadiabatic heating substantially influences both instantaneous and mean velocities. The burning velocity V as a function of the thickness d of a combustible layer (for $\delta = 0.5d$) is presented in Fig. 4. For thin layers, quasihomogeneous combustion takes place. In this case, the burning velocity depends on macrokinetic and thermal parameters but is nearly independent of the scale of heterogeneity. As the thickness increases, for d/δ = const, the homogeneous regime is replaced by the express-delivery one. In this case, the maximum temperature in a reactive layer sharply increases and considerably exceeds the equilibrium temperature. Despite the increase in the thickness of an inert layer, the mean heat flux into the nearest reactive layer increases. The

burning velocity attains a maximum. For thicker layers, the temperature is nearly constant and the flux decreases; as a result, the burning velocity decreases.

A more detailed analysis of the model proposed can be found in papers devoted to the character and features of heterogeneous combustion. Here, we note only two remarkable features of the discrete heterogeneous model in comparison with a homogenized mixture of reactive and inert layers. The localization of a combustible component in equidistant layers allows us to obtain the following effects:

In the first place, the transformations occur at higher, superadiabatic temperatures.

Secondly, the heat-pulse transport occurs at a higher velocity.

The first effect is of interest in self-propagating high-temperature synthesis (SHS) technology (SHS in weakly exothermic systems and the fusion of high-melting substances). The second one could be used in pyrotechnics (in systems of heat-pulse transport over a distance).

ACKNOWLEDGMENTS

This work was supported by the Russian Foundation for Basic Research, project no. 99-03-32392a.

REFERENCES

1. A. G. Merzhanov, Dokl. Akad. Nauk **353**, 505 (1997).
2. A. G. Merzhanov, A. N. Peregudov, and V. T. Gontkovskaya, Dokl. Akad. Nauk **360**, 217 (1998).
3. A. S. Rogachev and A. G. Merzhanov, Dokl. Akad. Nauk **365**, 788 (1999).
4. S. G. Vadchenko and A. G. Merzhanov, Dokl. Akad. Nauk **352**, 487 (1997).
5. A. G. Merzhanov and A. S. Rogachev, Russ. J. Phys. Chem., Suppl. 1 **74**, 20 (2000).
6. B. V. Novozhilov, Dokl. Akad. Nauk SSSR **141**, 151 (1961).
7. Ya. B. Zel'dovich, O. I. Leĭpunskiĭ, and V. B. Librovich, *Theory of Nonstationary Combustion of Powder* (Nauka, Moscow, 1975).

Translated by V. Chechin

Doklady Physics, Vol. 46, No. 9, 2001, pp. 624–626. Translated from Doklady Akademii Nauk, Vol. 380, No. 3, 2001, pp. 328–331.

PHYSICS

Ecton Mechanism for the Generation of Ion Flows in a Vacuum Arc

Academician G. A. Mesyats and S. A. Barengolts

Received September 3, 2001

In this paper, the parameters of an ion flow generated by cathode spots in a vacuum arc are explained for the first time based on the ecton mechanism.

The key problem of the physics of a vacuum arc is the mechanism governing the effusion of a conducting medium into vacuum, because it is this process that determines the discharge operation. Since the time the vacuum arc was discovered, the nature of the physical processes resulting in the generation of the cathode plasma and ion flows from cathode spots has been actively discussed. A generally accepted model of the processes occurring at the vacuum arc cathode is still lacking because of the difficulties related to the diagnostics of cathode spots, which execute permanent random motion. The characteristic temporal and spatial scales of the processes in cathode spots are 10^{-9} s and 10^{-4} cm, respectively [1, 2]. Nevertheless, in spite of the above difficulties, it is possible to determine the most important characteristics of cathode plasma generation. Such characteristics are the ion erosion rate γ_i (the ratio of the mass of the ions ejected from the cathode to the charge passed through the cathode, $q = i\Delta t$, where i is the arc current) and the average ion charge number Z in the cathode plasma. Obviously, an adequate physical model of a vacuum arc should explain the values of these parameters, which can be determined experimentally.

In recent years, a substantial progress in the investigation of the ion parameters in an arc plasma has been achieved. This is related to the creation of vacuum arc ion sources that make it possible to measure the ion distributions over charge states for practically all of the conductive materials [3]. These investigations have shown that the charge composition of a vacuum arc plasma remains unchanged as the arc current increases from 50 up to 500 A. An important result of these studies is the experimentally established fact that ions with different charges move at the same velocity [4], which undoubtedly evidences in favor of the gasdynamic mechanism for ion acceleration.

Institute of Electrophysics, Ural Division, Russian Academy of Sciences, ul. Amundsena 106, Yekaterinburg, 620016 Russia

The study of explosive electron emission [2] made it possible to reveal the nature of physical processes in the cathode spot of a vacuum arc. It was established that the parameters (such as the expansion velocity and charge composition) of a cathode jet plasma produced due to explosive electron emission in the spark stage of a discharge are almost the same as in the arc plasma. In both cases, the erosion patterns at the cathode are identical. The expansion velocity of the liquid metal fraction, the erosion rate, the cathode voltage drop, and the threshold current also coincide with those in the arc. All this allows us to conclude that, in a vacuum arc, explosive electron emission takes place. In [1], it was shown that the processes in a vacuum arc cathode spot are determined by microexplosions at the cathode accompanied by the formation of ectons (electron bunches) in the course of explosive electron emission.

In the present paper, we apply the ecton model of a vacuum arc cathode spot [1] to analyze the main characteristics of the processes resulting in the generation of a cathode plasma in a vacuum arc (such as the ion erosion rate and the average ion charge). According to this model, the cathode spot of a vacuum arc consists of individual cells emitting ectons. The model is based on the main experimentally observed features of the ion flows ejected from a vacuum arc cathode spot. The increase in the current leads to an increase in the number of cells. The main parameters of the ion flows are determined by the processes occurring in an individual cell in the course of explosive destruction of the cathode surface under the action of Joule heating. The cathode material sequentially passes through the following states: condensed matter, a nonideal plasma, and an ideal plasma. As a result, the ion charge composition of the plasma produced is established and the ions are accelerated by the pressure gradient of the plasma, whose density falls by several orders of magnitude over a distance of ten microns from the cathode surface.

An ecton is formed in the interaction of a liquid metal jet (see Fig. 1) ejected from the cathode spot region with the cathode plasma. By analogy to the electric explosion of a conductor, the current density j in the

1028-3358/01/4609-0624$21.00

jet during the ecton formation can be estimated by the formula

$$j = \left(\frac{\bar{h}}{t_d}\right)^{1/2}, \quad (1)$$

where $\bar{h}$ is the specific action of the current during the electric explosion and t_d is the explosion delay time. For the majority of metals, we have $\bar{h} \sim 10^9$ A^2 s cm^{-4}. Hence, for $t_d \approx 10^{-9}$ s, the current density is on the order of 10^9 A/cm^2. The high current density results in the rapid heating and explosion of the cathode spot region accompanied by explosive electron emission. In the course of explosion, the area of the emission zone increases and the current density decreases, so that both the heat removal due to thermal conduction and the energy withdrawal due to the ejection of the plasma and of the heated liquid metal begin to play an important role. As a result, explosive emission terminates and a short-lived electron bunch (ecton) is formed.

The ecton lifetime can be estimated as [1]

$$t_e = \frac{i_e^2}{\pi^2 a^2 \bar{h} \theta^4}, \quad (2)$$

where a is the thermal diffusivity of the cathode material and i_e is the ecton current. When deriving expression (2), it was assumed that the ecton is produced due to the explosion of a liquid metal point of conical geometry with a small apex angle θ (Fig. 1). The mass carried away from the cathode in time t_e is equal to

$$M = \frac{2}{3\pi^2} \frac{i_e^3 \rho}{(a\bar{h})^{3/2} \theta^4}, \quad (3)$$

where ρ is the mass density of the cathode material. The total charge of the electrons that have passed over the time during which the ecton exists is equal to

$$q_e = \frac{i_e^3}{\pi^2 a^2 \bar{h} \theta^4}. \quad (4)$$

Since the arc discharge is maintained due to the explosions of liquid metal microspots, in formulas (1)–(4), the liquid state values of a, ρ, and $\bar{h}$ should be used.

Because of the finite lifetime of the ecton, the processes in a cathode spot are cyclic in character. The cycle consists of two phases: the main (ecton) phase with a duration t_e equal to the ecton lifetime and the ion phase with a smaller duration t_i, in which a new ecton is initiated by the ion current from the cathode plasma. The cycle period can be estimated from the experimental data on the oscillations of both the discharge voltage at currents close to the threshold arc current and the noise discharge voltage. According to these estimates, the cycle period is on the order of $t_c \sim 30$ ns for copper and tungsten cathodes and the relative duration of the ion phase is $\alpha = \frac{t_i}{t_e + t_i} \approx 0.2$ [5].

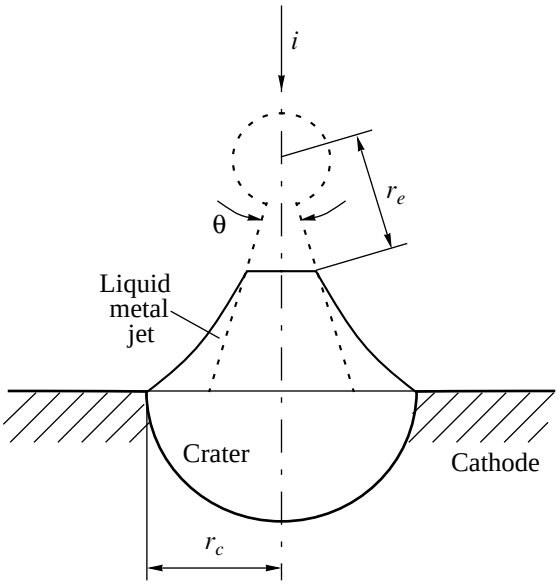

Geometry of a liquid metal jet at which an ecton is formed: r_c is the radius of the fused region at the cathode, and r_e is the radius of the ecton zone.

Another important property of the cathode spot is the presence of an internal structure that manifests itself in the existence of individual cells or the fragments of the cathode spot. According to [6], a current equal to the doubled threshold arc current i_t flows through each cell of the cathode spot. In the ecton model, the spot cell is regarded as an explosive emission center emitting a portion of electrons—an ecton.

The measurements of the ion energy distribution in an arc plasma showed that the ions leave the cathode spot with an average velocity of $\sim 10^6$ cm/s. These ions produce a current opposite to the arc current because they move from the cathode toward the anode. The measurements carried out by Kimblin [7] showed that the ion current collected by a cylindrical screen has a maximum, which is independent of the geometrical parameters, is approximately proportional to the total arc current, and depends slightly on the cathode material. The ratio of the ion current to the total current is approximately equal to 0.1.

The ion current from the cathode results in the loss of the cathode material, emitted as ions. Experimental data on the cathode erosion are rather contradictory because, along with ion erosion, the cathode material is carried away in the form of macroparticles, drops, and neutral vapor. The results obtained by conventional methods for determining the erosion parameters (such as weighing a sample and estimating the erosion rate by the change in the geometrical parameters of the erosion

The ion erosion rate and the average ion charge number in an arc plasma for different cathode materials

Material	ρ, g/cm^3	a, cm^2/s	$\bar{h} \times 10^{-9}$, A^2 s cm^{-4}	γ_i, μg/C	Z	Z [3, 10]
Cu	8.0	0.42	3.1	37.2	1.76	1.7–2.0
Au	17.2	0.40	1.3	120.6	1.69	1.6–2.0
Al	2.3	0.40	1.4	15.5	1.80	1.5–1.7
Ag	9.3	0.56	2.0	62.2	1.77	1.8–2.1
W	17.0	0.14	1.5	65.7	2.90	3.0–3.1

structure) depend substantially on the arc current, discharge duration, and cathode geometry. Daalder [8] carried out a series of experiments with copper electrodes 25 and 10 mm in diameter. The current varied in the range 33–200 A. It was found that, as q decreased to 0.1 C, the measurements of the erosion rate carried out at different currents yielded the same value equal to ~40 μg/C, which was the ion erosion rate. The ion erosion rate can also be determined from the measured average ion charge number by the formula [8]

$$\gamma_i = \frac{i_i}{i}\frac{m}{Ze}, \tag{5}$$

where i_i is the ion current from the cathode, Z is the average ion charge number in an arc plasma, and m is the mass of an ion.

Let us apply the ecton model to analyze the characteristics of the ion flow emitted by the cathode spot. The mass carried away during the time t_e is determined by formula (3). During the time t_i, the ion current, which is directed to the cathode, is approximately equal to 0.1 of the arc current. Therefore, during a cycle, the total loss of mass by the cathode is equal to $M(1–2\alpha)$. Taking into account expression (4), we obtain the following expression for the ion erosion rate:

$$\gamma_i = \frac{2}{3}\rho\left(\frac{a}{\bar{h}}\right)^{1/2}(1-2\alpha). \tag{6}$$

Using formulas (5) and (6), we can determine the average ion charge number in a plasma produced under the action of an ecton:

$$Z = \frac{3i_i}{2i}\frac{m}{e\rho(1-2\alpha)}\left(\frac{\bar{h}}{a}\right)^{1/2}. \tag{7}$$

Since we have $\frac{i_i}{i} \approx 0.1$ for all the materials [7], the values of γ_i and Z are independent of the current and are determined exclusively by the cathode material, which agrees with the experimental results of [3, 8]. The table presents the average ion charge numbers and the ion erosion rates calculated by using formulas (6) and (7) for a number of metals for which the values of $\bar{h}$ are known. The values of the thermophysical coefficients are taken from [9]. For all of the metals (by analogy to tungsten and copper), the value of α was set equal to 0.2. It is seen that the calculated values agree well with the experimental data, which is somewhat surprising, taking into account an uncertainty in the cathode spot temperature and a significant scatter in the experimental data on the thermophysical parameters of the materials under consideration.

Thus, the estimates of the ion parameters in a vacuum arc obtained using the ecton model agree qualitatively and quantitatively with the experimental data. We note that these estimates are obtained for a single cell of the cathode spot (a single ecton). The increase in the arc current is related to the increase in the number of simultaneously existing ectons. That is why, in experiments, the ion parameters depend only slightly on the arc current (up to currents of about 1 kA, at which the magnetic field of the plasma column begins to play an important role).

ACKNOWLEDGMENTS

This study was supported in part by the Russian Foundation for Basic Research (project no. 99-02-18234) and INTAS–RFBR (grant no. 97-0663).

REFERENCES

1. G. A. Mesyats, Pis'ma Zh. Éksp. Teor. Fiz. **60**, 514 (1994) [JETP Lett. **60**, 527 (1994)].
2. G. A. Mesyats and D. I. Proskurovsky, *Pulsed Electrical Discharge in Vacuum* (Nauka, Novosibirsk, 1984; Springer-Verlag, Berlin, 1989).
3. I. G. Brown, Rev. Sci. Instrum. **65**, 3061 (1994).
4. G. Yu. Yushkov, E. M. Oks, A. Anders, and I. G. Brown, J. Appl. Phys. **88**, 5618 (2000).
5. S. A. Barengolts and G. A. Mesyats, Pis'ma Zh. Tekh. Fiz. **27** (6), 82 (2001) [Tech. Phys. Lett. **27**, 256 (2001)].
6. I. G. Kesaev, *Cathode Processes in Electric Arc* (Nauka, Moscow, 1968).
7. C. W. Kimblin, J. Appl. Phys. **44**, 3074 (1973).
8. J. E. Daalder, J. Phys. D **8**, 1647 (1975).
9. V. E. Zinov'ev, *Thermal Properties of Metals under High Temperatures: Handbook* (Metallurgiya, Moscow, 1989).
10. I. G. Brown, B. Feinberg, and J. E. Galvin, J. Appl. Phys. **63**, 4889 (1988).

Translated by A. Sakharov

Doklady Physics, Vol. 46, No. 9, 2001, pp. 627–632. Translated from Doklady Akademii Nauk, Vol. 380, No. 3, 2001, pp. 332–337.

PHYSICS

Low-Temperature Initiation of the Detonation Combustion of Gas Mixtures in a Supersonic Flow under Excitation of the $O_2(a^1\Delta_g)$ State of Molecular Oxygen

A. M. Starik and N. S. Titova

Presented by Academician O.N. Favorskiĭ April 2, 2001

Received April 2, 2001

INTRODUCTION

Vibrational pre-excitation of reacting molecules leads to an increase in the combustion rate for (H_2 + air) mixtures and to a reduction in the length of the induction zone in a supersonic flow behind a shock front [1]. These effects are caused by the intensification of reactions that lead to the formation of O and H atoms and OH radicals, which are responsible for the chain combustion mechanism. Vibrational excitation is known to cause an increase in the inelastic collision cross section $\sigma(E)$ for reacting molecules. In this case, the value of threshold energy E_{th} at which the inelastic interaction between colliding particles become possible decreases. Hence, the reaction rate for molecules excited into a low-lying vibrational state is greater by several orders of magnitude than that for unexcited molecules [2, 3].

The excitation of the electronic state of molecules should lead to an increase in $\sigma(E)$ and E_{th} that is greater than that caused by vibrational excitation. The reaction rate constant k is related to the cross section $\sigma(E)$ by the formula

$$k = \int_{E_{\text{th}}}^{\infty} \sigma(E)\sqrt{E} f(E) dE,$$

where $f(E)$ is the energy distribution function for molecules. Therefore, the increment of k due to the excitation of the electronic state of a reagent should obviously be greater than that caused by vibrational excitation. This conclusion was verified by experimental data [2, 4]. We will show that the excitation of the electronic state of molecular oxygen into the $O_2(a^1\Delta_g)$ state can significantly affect the combustion kinetics for $H_2 + O_2$ mixtures and initiate the detonation combustion of the gas behind a shock front at a low temperature (~650 K). The molecules O_2 can be excited either by laser radiation with a wavelength $\lambda = 1.27$ μm [5] or by an electric discharge [6].

STATEMENT OF THE PROBLEM AND KINETIC MODEL

We will analyze a flow with a stationary shock wave whose front is inclined at an angle $\beta < 30°$ to the velocity vector u_0 of the undisturbed flow and whose gas velocity behind the front remains supersonic [1]. The pressure P_0 and the Mach number M_0 in the undisturbed flow range from 10^2 to 10^4 Pa and from 5 to 6, respectively. We assume that the translational, rotational, and vibrational degrees of freedom of the molecules in the mixture are in thermodynamic equilibrium, which is not disturbed by chemical reactions. As was shown in [7], a sufficiently complete scheme of 29 reactions involving H, O, OH, H_2O, H_2, O_2, HO_2, H_2O_2, and O_3 should be used in order to describe the low-temperature ignition of the $H_2 + O_2$ mixture. The presence of $O_2(a^1\Delta_g)$ molecules necessitates the introduction of the additional reactions listed in Table 1.

The excitation vibrational and electronic states lower the endoergic-reaction barrier in the Arrhenius law

$$k_q = A_q T^{n_q} \exp\left(-\frac{E_{aq}}{T}\right),$$

where E_{aq} is the activation energy for the qth reaction and T is the gas temperature. In this case, $E_{aq} = E_{aq}^0 - \alpha_q E_{eq}$, where E_{aq}^0 is the activation energy for the qth reaction involving unexcited reagents, E_{eq} is the excitation energy of the reacting molecule, and α_q is a utilization factor for the vibrational or electronic energies, whose value is given by the expression (for $E_{eq} < E_{aq}$) [8]

$$\alpha_q = \frac{E_{aq}^+}{E_{aq}^+ + E_{aq}^-}.$$

Baranov Central Institute of Aviation Motors, Aviamotornaya ul. 2, Moscow, 111250 Russia

1028-3358/01/4609-0627$21.00

Table 1. Reactions involving $O_2(a^1\Delta_g)$ that were included in the description of the combustion kinetics for hydrogen–oxygen mixtures

No.	Reaction	No.	Reaction
1	$O + O + M = O_2(a^1\Delta_g) + M$	9	$H + O_2(a^1\Delta_g) = OH + O$
2	$HO_2 + M = O_2(a^1\Delta_g) + H + M$	10	$H_2 + O_2(a^1\Delta_g) = 2OH$
3	$2HO_2 = H_2O_2 + O_2(a^1\Delta_g)$	11	$H_2 + O_2(a^1\Delta_g) = H + HO_2$
4	$O_3 + O = O_2 + O_2(a^1\Delta_g)$	12	$H_2O + O_2(a^1\Delta_g) = OH + HO_2$
5	$H + O_3 = OH + O_2(a^1\Delta_g)$	13	$OH + O_2(a^1\Delta_g) = O + HO_2$
6	$O_3 + OH = HO_2 + O_2(a^1\Delta_g)$	14	$H_2O + O_2(a^1\Delta_g) = H_2O_2 + O$
7	$O_3 + HO_2 = OH + O_2 + O_2(a^1\Delta_g)$	15	$O_3 + O_2(a^1\Delta_g) = O_2 + O_2 + O$
8	$O_3 + M = O + O_2(a^1\Delta_g) + M$	16	$O_2(a^1\Delta_g) + M = O_2 + M$

Here, E_{aq}^+ and E_{aq}^- are the activation energies for the qth reactions of the disintegration and formation of an excited molecule, respectively. The procedure of decreasing E_{aq} was employed to determine the rate constants for the backward reactions 1, 4, and 5, and for the forward reactions 10, 12, and 13. The temperature dependences of the rate constants for the forward and backward exchange reactions 9 and 11 and for reaction 15 were taken from papers [9] and [10], respectively.

For reactions with low or zero activation energies E_{aq}^0, which lead to the formation of $O_2(a^1\Delta_g)$ or $O_2(b^1\Sigma_g^+)$ molecules, we assume that the probability of exciting the corresponding electronic states of O_2 molecules is determined by their degeneracy multiplicities. In this way, we determined the rate constants for the forward reactions 2, 3, 6, 7, and 8, and for the backward reaction 14. In so doing, we assume that the reaction rate for the electronic–translational (E–T) relaxation $O_2(b^1\Sigma_g^+) \longrightarrow O_2(a^1\Delta_g)$ is much higher than the rates of all other processes. For the forward reactions 1, 4, 5, and 14, as well as for the backward reactions 3, 6, 7, 10, 12, 13, and 15, the rate constants were evaluated on the basis of the detailed balance principle. The relaxation rate constants for the $O_2(a^1\Delta_g)$ state (reaction 16) were taken from [11].

LASER BEAM EXCITATION OF O_2

Let a homogeneous $2H_2 + O_2$ gas mixture moving at supersonic velocity ahead of a shock wave front be acted upon by a radiation field on the interval $[x_0 - \delta, x_0]$. We assume that the radiation intensity I is constant and that the frequency ν_I coincides with that of the electronic-vibrational transition for the O_2 molecule, $m(X^3\Sigma_g^-, v', j', K') \longrightarrow n(a^1\Delta_g, v'', j'', K'')$. Here, (v', j', K') and (v'', j'', K'') are the vibrational and rotational quantum numbers for the $X^3\Sigma_g^-$ and $a^1\Delta_g$ states, respectively. It will be recalled that these transitions are allowed in the magnetic-dipole approximation. We now consider the cases when the rates of chemical reactions upstream from the shock wave front are considerably lower than the rates of both induced transitions and the collisional relaxation of the $a^1\Delta_g$ state. In this case, we can use the two-level approximation for excitations of the O_2 molecules. The concentrations N_m and N_n of the O_2 molecules in the $X^3\Sigma_g^-(N_m)$ and $a^1\Delta_g(N_n)$ states, respectively, are determined by the relationships

$$N_m = \frac{B}{A} + \left(N_m^0 - \frac{B}{A}\right)\exp\left(-A\frac{t}{\tau_R}\right),$$

$$N_n = N_n^0 + \left(N_m^0 - \frac{B}{A}\right)\left[1 - \exp\left(-A\frac{t}{\tau_R}\right)\right],$$

$$A = \left(1 + \frac{g_n}{g_m}\right)\frac{\tau_R}{\tau_I} + 1 + \frac{g_n}{g_m}\exp\left(-\frac{\Delta E_{nm}}{KT}\right), \qquad (1)$$

$$B = (N_m^0 + N_n^0)\left(1 + \frac{\tau_R}{\tau_I}\right),$$

$$(\tau_I)^{-1} = \frac{W_{nm}I}{h\nu_I}, \quad W_{nm} = \frac{\lambda_{mn}^2 A_{mn}}{4\pi b_D}\sqrt{\frac{\ln 2}{\pi}}H(x, a).$$

Here, N_m^0 and N_n^0 are the concentrations of the $O_2(X^3\Sigma_g^-)$ and $O_2(a^1\Delta_g)$ molecules in the undisturbed flow ($x \le x_0 - \delta$), respectively; h is Planck's constant; λ_{mn} is the wavelength corresponding to the midpoint of the absorption line; A_{mn} is the Einstein coefficient; b_D is the Doppler width of the spectral line for the transition $m \longrightarrow n$; $\Delta E_{nm} = E_n - E_m$; E_n and E_m are the corresponding energy levels of the O_2 molecule; g_n and g_m are the corresponding degeneracy multiplicities; K is the Boltzmann constant; τ_R is the electronic–translational relax-

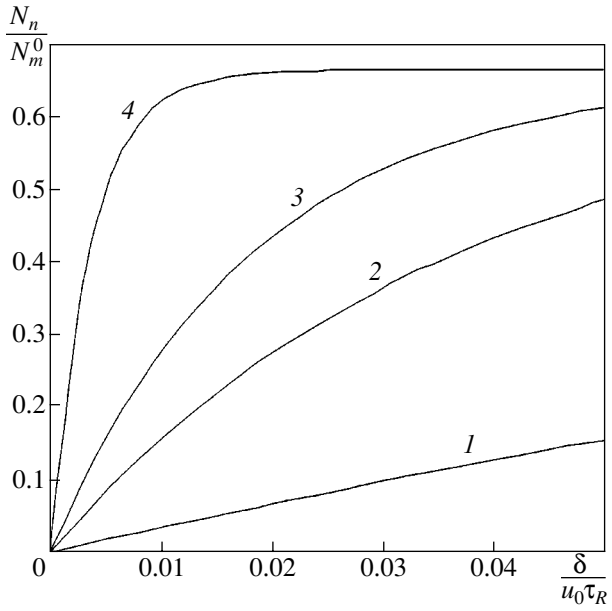

Fig. 1. Evolution of relative concentrations of the excited $O_2(a^1\Delta_g)$ molecules in the laser radiation action zone at $P_0 = 10^3$ Pa for I = (*1*) 1, (*2*) 5, (*3*) 10, and (*4*) 50 kW/cm^2.

ation time for the $O_2(a^1\Delta_g)$ state $\left(\tau_R^{-1} = \sum_M N_M k_{16}^M\right)$; and $H(x, a)$ is the Voigt function. We will analyze a particular case where the radiation frequency coincides with the midpoint of the transition line $^QP(3)$, with $v' = v'' = 0, j' = 4, j'' = 3$, and $K' = K'' = 3$. For this transition, the Einstein coefficient and wavelength are equal to 2.58×10^{-4} s^{-1} and 1.268 μm, respectively.

We now define the characteristic times τ_I, τ_R, and τ_A and the absorption length $L_\nu = k_\nu^{-1}$, which specify the external action and the spatial scale of the problem. For $P_0 = 10^2$–10^4 Pa and $T_0 = 300$ K, the time τ_R ranges from 0.1 to 0.05 s. The time τ_A is related to the length δ of the radiation action zone and to the flow velocity u_0 by the formula $\tau_A = \frac{\delta}{u_0}$. The quantity τ_I specifies the rate of production of the $O_2(a^1\Delta_g)$ molecules. The condition $\tau_I \ll \tau_R$ should be satisfied in order to obtain a high concentration of $O_2(a^1\Delta_g)$ molecules. Given τ_R and τ_A, the relative concentration of excited O_2 molecules increases with radiation intensity I. This is illustrated in Fig. 1, where the quantity $\frac{N_n}{N_m^0}$ is shown as a function of the length of the action zone for various values of I. For high supersonic-flow velocities, it is fairly difficult to attain large values of N_n if δ is small. For example, when $M_0 = 6$ and $P_0 = 10^3$ Pa, the quantity $u_0\tau_R$ is equal to 2100 m. Hence, for $\delta = 1$ m, the value of N_n is not greater than $0.05\,N_m^0$ even for $I = 50$ kW/cm^2. However, such a concentration of $O_2(a^1\Delta_g)$ molecules in the mixture is sufficient for both lengths, L_{in} and L_c of the induction and combustion zones, respectively, to decrease significantly (their values were determined in the same way as in [12]). This effect is seen in Fig. 2,

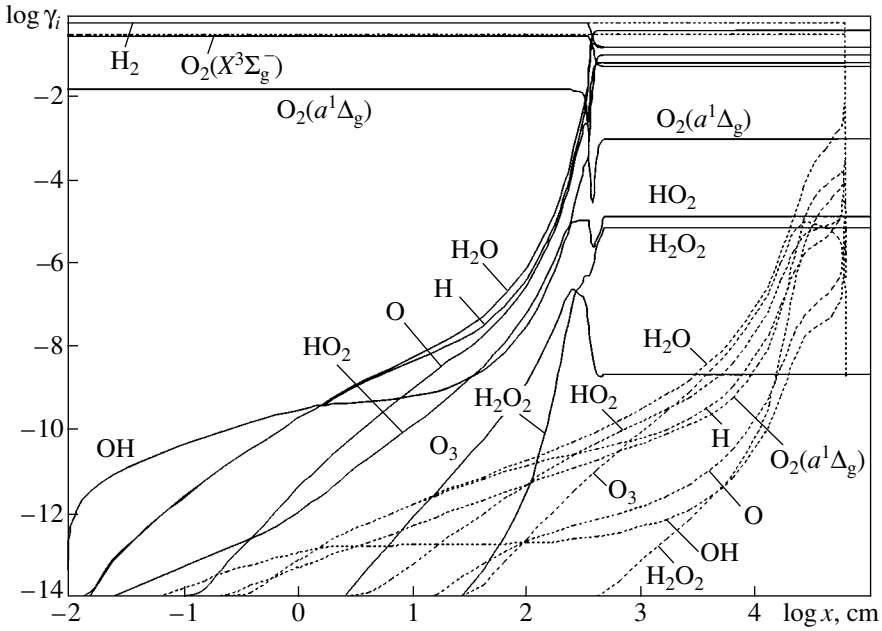

Fig. 2. Evolution of concentrations of the components behind the front of the shock wave with $M_0 = 6$, $\beta = 25°$, and $P_0 = 10^3$ Pa. The flow of the $2H_2 + O_2$ mixture is subjected to laser irradiation with a wavelength $\lambda = 1.268$ μm and an intensity $I = 50$ kW/cm^2 (solid lines). Dashed lines correspond to the absence of irradiation.

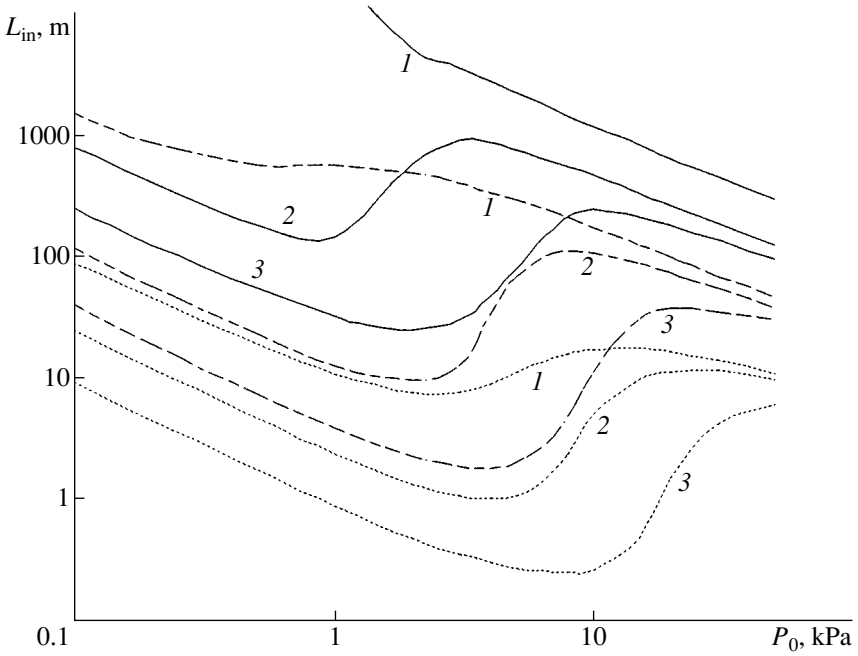

Fig. 3. Length L_{in} as a function of pressure P_0 in the case of combustion of the $2H_2 + O_2$ mixture behind the front of the shock wave, with $M_0 = 6$ and $T_0 = 300$ K. Solid, broken, and dashed lines correspond to $\beta = 20°$, 25°, and 30°, respectively, for the radiation intensities I = (*1*) 0, (*2*) 10, and (*3*) 50 kW/cm^2.

which shows the spatial dependence of the mole concentrations γ_i for various components behind the shock wave front in a mixture subjected (or not subjected) to radiation. Under these conditions, the length L_{in} diminishes by a factor of 200. Since the absorption length L_ν is equal to 257 and 81 m at the pressure $P_0 = 10^3$ and 10^4 Pa, respectively, the corresponding concentration of $O_2(a^1\Delta_g)$ molecules in the action zone can be attained by repetitive scanning across the flow using a narrow laser beam with a radius ranging from 0.1 to 1 cm.

When exciting the $a^1\Delta_g$ state of the O_2 molecules, the reduction of the combustion zone length for the $H_2 + O_2$ mixture is attained by an intensification in the chain combustion reactions. Indeed, the combustion is initiated by the formation of OH, O, and H in the following reactions: $H_2 + O_2 = 2OH$, $OH + H_2 = H_2O + H$, $H + O_2 = OH + O$, and $O + H_2 = OH + H$. The presence of excited $O_2(a^1\Delta_g)$ molecules in the mixture opens up new production channels for OH, O, and H. These are basically reactions 9, 10, and 11 (see Table 1). It is worth noting that, for $T_1 < 700$ K, reaction 15 involving the $O_2(a^1\Delta_g)$ and O_3 molecules becomes essential for the formation of O atoms. All these processes have very high reaction rates. Hence, the presence of even a small amount of $O_2(a^1\Delta_g)$ molecules leads to a significant decrease in L_{in} and L_c. The extent of this decrease depends on the mixture parameters P_1 and T_1 behind the shock wave front, which define the ratio $\frac{\tau_I}{\tau_R}$ and, therefore, the concentration of $O_2(a^1\Delta_g)$ molecules in the induction zone as well as on the quantity I. The values of P_1 and T_1 depend on P_0, T_0, M_0, and β.

The dependence of L_{in} on P_0 for $M_0 = 6$, $T_0 = 300$ K, and $\beta = 20°$, 25°, and 30°, corresponding to $T_1 = 517$, 646, and 791 K, is shown in Fig. 3. There are two ranges of P_0 for each set of the parameters I and β. Indeed, L_{in} can either increase or decrease with increasing P_0. The boundary value P_{0b} separating these ranges increases with I and T_1. The existence of P_{0b} and the increase in L_{in} at $P_0 > P_{0b}$ are due to the formation of chemically inert H_2O_2 molecules and the decrease in the concentration of OH, O, and H [7]. The higher the concentration of $O_2(a^1\Delta_g)$ in a mixture, the greater the pressure P_0 at which these processes begin to dominate. It is seen that the excitation of O_2 molecules into the $a^1\Delta_g$ state allows detonation combustion to be initiated at small distances behind the shock wave front. Indeed, for $\beta = 30°$ and $P_0 = 8000$ Pa, the length L_{in} for I = 50 kW/cm^2 amounts to only 25 cm, while it attains 15 m if there are no excited molecules. Even if the temperature T_1 of the gas behind the front is as small as 646 K ($\beta = 25°$), the length L_{in} for $I = 50$ kW/cm^2 can still be diminished to 1.8 m.

ELECTRIC DISCHARGE EXCITATION OF O_2 MOLECULES

We now consider the case where oxygen activated in an electric discharge is mixed with hydrogen upstream from a shock wave. A bulk electric discharge in oxygen leads to the formation of small amounts of ozone, O, O_2^+, O_3^+, O_4^+, O^-, O_2^-, and O_3^- [6, 13] as well as $O_2(a^1\Delta_g)$ and $O_2(b^1\Sigma_g^+)$ molecules. However, the ions disappear after a short time; as a result, only the long-lived molecules $O_2(X^3\Sigma_g^-)$, $O_2(a^1\Delta_g)$, O, and O_3 remain behind the discharge zone. According to [14], at T_0 = 300 K and P_0 = 1316 Pa, the concentrations of O, $O_2(a^1\Delta_g)$, and O_3 behind this zone are equal to 0.0071, 0.0145, and 0.0165, respectively, and remain invariable over the time $\tau_r = 10^{-3}$ s. Even for supersonic flows with Mach numbers from 5 to 6, the typical mixing length of H_2 and discharge-activated O_2 does not exceed 0.5 m. This corresponds to the characteristic mixing time $\tau_m \sim 3 \times 10^{-4}$ s; therefore, $\tau_m < \tau_r$. For the initial stoichiometric mixture of H_2 and O_2, the concentrations of H_2, $O_2(X^3\Sigma_g^-)$, $O_2(a^1\Delta_g)$, O, and O_3 formed in the mixture are equal to 0.668, 0.32, 4.84×10^{-3}, 2.35×10^{-3}, and 5.49×10^{-3}, respectively.

Compared to the presence of excited O_2 molecules, the presence of O_3 and O along with $O_2(a^1\Delta_g)$ leads to a significant increase in the combustion rate behind the shock wave front. This conclusion is illustrated in Fig. 4, where the concentrations of both the initial components and those formed in the combustion process are presented. Variants 1 and 2 correspond, respectively, to the mixtures H_2–$O_2(X^3\Sigma_g^-)$–$O_2(a^1\Delta_g)$–O–O_3 (electric-discharge excitation) and H_2 : $O_2(X^3\Sigma_g^-$: $O_2(a^1\Delta_g)$ = 0.667 : 0.328 : 0.005 [laser excitation of $O_2(a^1\Delta_g)$]. A more marked intensification of chain reactions in the

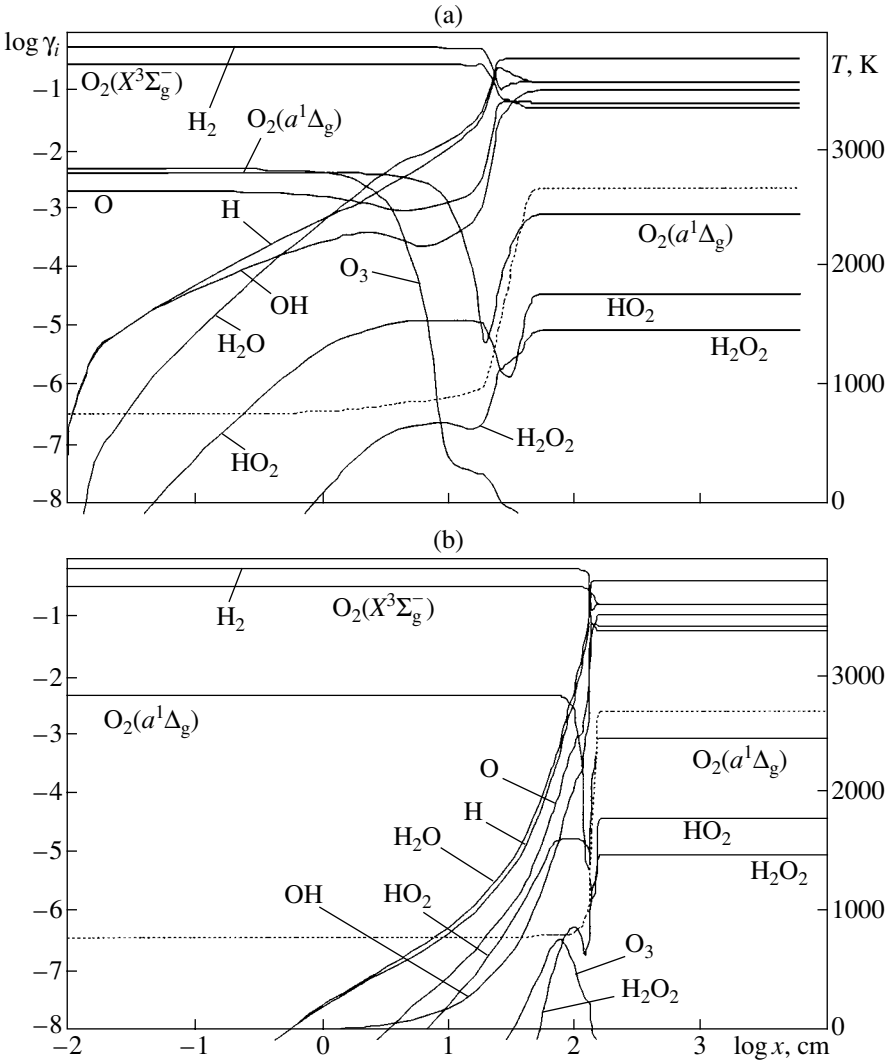

Fig. 4. Evolution of concentrations of the components (solid lines) and temperature of the gas (dashed lines) in the case of combustion of mixtures (a) *1* and (b) *2* behind the front of the shock wave, with $M_0 = 6$, $\beta = 30°$, $T_0 = 300$ K, and $P_0 = 1316$ Pa.

Table 2. Values of L_{in} and L_c for various methods of activating molecular oxygen. The combustion of the $2H_2 + O_2$ mixture occurs behind the front of an inclined shock wave at P_0 = 1316 Pa and T_0 = 300 K. In the two last columns, numbers $A \times 10^m$ are presented as $A(m)$

M_0	β	T_1, K	Activation method O_2	L_{in}, cm	L_c, cm
5	20	439	1	5.82(2)	6.25(2)
			2	3.81(5)	3.81(5)
6	20	517	1	2.53(2)	3.06(2)
			2	7.38(3)	7.43(3)
7	20	605	1	1.28(2)	1.56(2)
			2	1.47(3)	1.53(3)
6	30	791	1	26.5	48.1
			2	1.33(2)	1.55(2)

combustion process under the electric-discharge excitation of O_2 is caused not only by the presence of O atoms in the reaction mixture but also by the appearance of new production channels for O atoms and OH radicals in reaction 15 and in the reaction $O_3 + H = OH + O_2$, respectively. In this case, detonation combustion can be initiated in the gas behind the shock wave front at a temperature as low as $T_1 \le 600$ K. At such a temperature, the detonation combustion of the nonactivated $2H_2 + O_2$ mixture cannot be realized. This method of activating O_2 yields a more pronounced decrease in L_{in} and L_c than the excitation of O_2 molecules into the $a^1\Delta_g$ state. This follows from the data listed in Table 2 for various values of M_0 and β and for the two variants of activating the O_2 molecules. For $M_0 = 6$ and $\beta = 30°$ (T_1 = 791 K), the electric-discharge excitation of O_2 allows one to obtain a combustion zone length L_c as short as ~0.5 m, whereas without activating O_2 the length L_c is equal to 9 m.

Thus, the laser beam excitation of the metastable $O_2(a^1\Delta_g)$ state of molecular oxygen or its excitation by an electric discharge leads to the initiation of the detonation combustion of hydrogen–oxygen mixtures in a supersonic flow behind the front of a fairly weak shock wave when the temperature T_1 of the gas does not exceed 750 K. In this case, the length of the combustion zone can be as short as 1 m.

ACKNOWLEDGMENTS

This work was supported by the Russian Foundation for Basic Research, projects no. 99-01-01165 and no. 99-02-18494.

REFERENCES

1. A. M. Starik and N. G. Dautov, Dokl. Akad. Nauk **350**, 757 (1996) [Phys. Dokl. **41**, 465 (1996)].
2. G. G. Light, J. Chem. Phys. **68**, 2831 (1978).
3. *Combustion Chemistry*, Ed. by W. C. Cardiner (Springer, New York, 1984).
4. L. T. Cupit, G. A. Takacs, and G. P. Glass, Int. J. Chem. Kinet. **14**, 487 (1982).
5. A. M. Starik and O. V. Taranov, Zh. Tekh. Fiz. **68** (8), 15 (1998) [Tech. Phys. **43**, 890 (1998)].
6. K. S. Klopovskiĭ, A. S. Kovalev, D. V. Lopaev, *et al.*, Fiz. Plazmy **18**, 1606 (1992) [Sov. J. Plasma Phys. **18**, 834 (1992)].
7. A. M. Starik and N. S. Titova, Khim. Fiz. **19** (9), 61 (2000).
8. V. D. Rusanov and A. A. Fridman, *Physics of Chemically Active Plasma* (Nauka, Moscow, 1984).
9. V. Ya. Basevich and A. A. Belyaev, Khim. Fiz. **8**, 1124 (1989).
10. D. L. Baulch, R. A. Cox, P. J. Crutzen, *et al.*, J. Phys. Chem. Ref. Data **11**, 327 (1982).
11. Yu. A. Kulagin, L. A. Shelepin, and V. I. Yarygina, Tr. Fiz. Inst. Akad. Nauk **212**, 166 (1994).
12. A. M. Starik and N. S. Titova, in *Gaseous and Heterogeneous Detonations: Science to Applications* (ENAS-Publ., Moscow, 1999), pp. 225–240.
13. O. A. Gordeev, Yu. F. Kolesnichenko, and D. V. Khmara, Khim. Fiz. **19**, 67 (2000).
14. K. S. Klopovskiĭ, A. S. Kovalev, D. V. Lopaev, *et al.*, Zh. Éksp. Teor. Fiz. **107**, 1080 (1995) [JETP **80**, 603 (1995)].

Translated by V. Chechin

Doklady Physics, Vol. 46, No. 9, 2001, pp. 633–635. Translated from Doklady Akademii Nauk, Vol. 380, No. 1, 2001, pp. 34–37.

TECHNICAL PHYSICS

A Paradox of Severe Plastic Deformation in Metals

R. Z. Valiev and I. V. Aleksandrov

Presented by Academician R.I. Nigmatulin February 28, 2001

Received March 16, 2001

It is well known that plastic deformation in metals and many other crystalline materials is associated with their strain hardening [1, 2]. Generally, the larger the deformation magnitude, the higher is the metal strength and the lower the reserve of its plasticity. Strain hardening is applied in the cold rolling of automobile sheets, the drawing of wires, and in many other technological processes. However, their efficiency is reduced due to the plasticity loss by metals. In this study, we show that severe plastic deformation of metals, i.e., their strong deformation under conditions when very high pressures are applied [3–5], leads to a new effect that is characterized by a concurrent increase in both strength and plasticity. The physical nature of this new phenomenon is related to the formation of nanometer-sized structures (nanostructures) and the modification of the micromechanisms of deformation. The observed effect may result in completely new possibilities for the use of metallic materials.

In this study, we used two methods that cause severe plastic deformation and which were actively developed in recent years [4]: torsion under high pressure and equichannel angular pressing (Fig. 1). In both methods, deformation is caused by shear and accumulates by increasing either the number of turns under torsion or the number of runs under equichannel angular pressing. An important advantage of the pressing method is the possibility of obtaining massive blanks, which makes it possible to cut out samples that are suitable for a detailed investigation of their mechanical properties. It is worth noting that the magnitude of the true strain, which corresponds to each pass, is about unity [4], while the pressure applied, as in the case of the torsion method, exceeds 2 GPa.

In performing our investigations, pure Cu (99.996%) was subjected to equichannel angular pressing with rotation through 90° between successive passes. In addition, pure Ti (99.98%) and the intermetallic Ni_3Al compound were also studied, which were subjected to torsion under high pressure. Severe plastic deformation was brought about at room temperature. Both strength and plasticity were determined according to the results of uniaxial-tension tests of plane samples with dimensions of $5 \times 2 \times 1$ mm^3. The deformation rate reached 10^{-3} s^{-1}.

The results of the mechanical-tension tests for each material are shown in Fig. 2, and the stress–deformation curves for a state obtained by severe plastic deformation are presented. For comparison, the corresponding results for the coarse-grained annealed state of the materials and their state upon being subjected to deformation by rolling or extrusion are also presented.

The initial coarse-grained Cu with grain sizes of about 30 μm exhibits a typical behavior (Fig. 2, curve *1*) associated with a low elastic limit, insignificant cold hardening, and significant elongation. Upon cold rolling, the strength of Cu significantly increases but its plasticity drops considerably (Fig. 2, curve *2*); the higher the rolling deformation, the higher the strength, but the lower the plasticity. This tendency apparently continues when Cu is subjected to two passes of equichannel angular pressing where the deformation magnitude is close to 2 (Fig. 2, curve *3*). However, the situation completely changes for Cu subjected to much more severe deformation, e.g., when the number of passes is equal to 16 (Fig. 2, curve *4*). In this case, we not only observed a further increase in strength that reached the extreme values for Cu but also a noticeable increase in plasticity. It should be noted that all the tests were performed at room temperature.

A similar regularity was observed in Ti subjected to severe plastic deformation by torsion (Fig. 2). Here, after deformation by single-turn torsion (when the true logarithmic strain is close to unity), followed by tensile deformation at 250°C, we also observed hardening. However, in this case, the plasticity decreased (Fig. 2, curve *6*) when compared to the initial coarse-crystalline state with average grain sizes of 20 μm (Fig. 2, curve *5*). A further increase in the degree of severe deformation (to 5 turns) allows for the attainment of an extremely high strength of Ti (Fig. 2, curve *7*), with an ultimate strength of about 1000 GPa. This value is comparable with that which is typical for high-strength Ti-based alloys. The plasticity also rises when the ultimate elon-

Institute of Physics of Advanced Materials,
Ufa State Technical University of Aviation,
ul. Karla Marksa 12, Ufa, Bashkortostan, 450000 Russia

1028-3358/01/4609-0633$21.00

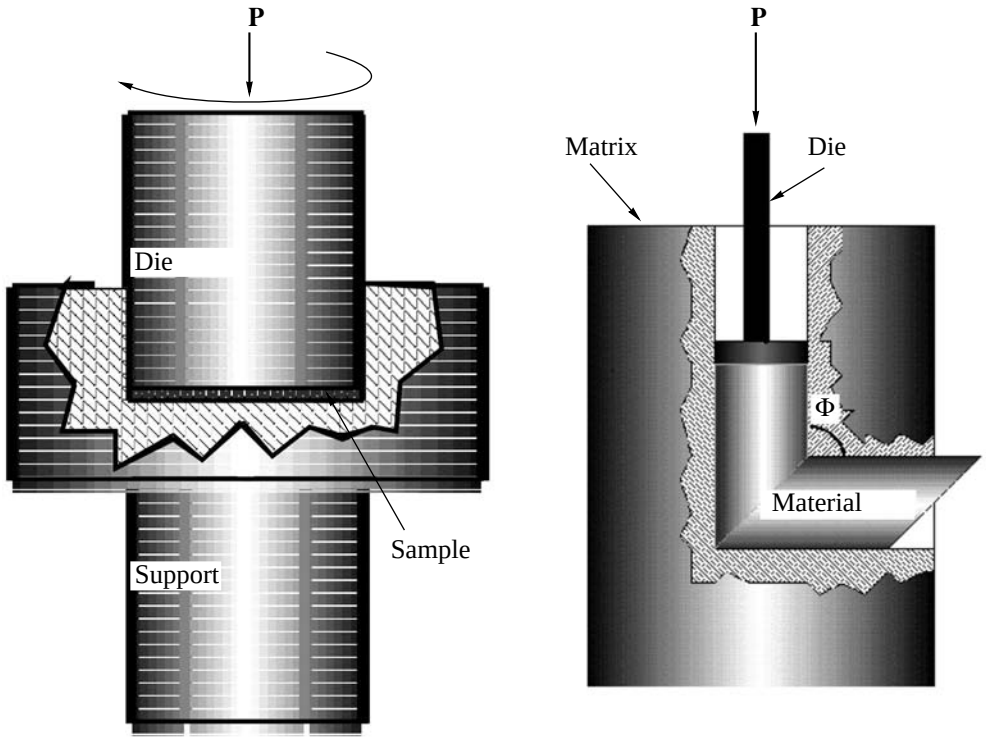

Fig. 1. Methods of severe plastic deformation: torsion under high pressure and equichannel angular pressing.

gation exceeds even the maximum elongation for the initial annealed sample.

The Ni_3Al intermetallic compound in the recrystallized state (with grain sizes of 5 μm) obtained by hot extrusion exhibits (including the extension at 650°C, Fig. 2, curve *8*) a limited plasticity that is typical for this material. The severe deformation by single-turn torsion increases the strength, but the plasticity remains insignificant (Fig. 2, curve *9*). However, further severe deformation (up to 5 turns) qualitatively changes the situation. In this case, the material displays a very high strength and, at the same time, extreme plasticity with an elongation to the point of failure that exceeds 300% (Fig. 2, curve *10*).

Thus, the tests of all three materials show that, under the action of severe plastic deformation by both torsion under high pressure and equichannel angular pressing, their behavior qualitatively changes. They demonstrate not only a very high strength but also a very high plasticity. Such a behavior of the materials qualitatively differs from that of metals and alloys subjected to large plastic deformation, e.g., by rolling or drawing, where an increase in strength usually correlates with a decrease in plasticity [2, 6]. The unusual phenomenon described in this paper defines a paradox of severe plastic deformation that exists when, in contrast to the well-known tendencies of very large deformations characterized by true strains exceeding 6–8, there is a rise not only in the strength but also in the plasticity of metals and alloys.

To understand the nature of the above effect, we consider recent data on the investigations of structures. The data show that under high pressure severe plastic deformation, whose degree exceeds 6–8, results in the formation of nanostructures having extremely small grain sizes on the order of 100 nm [3, 4]. These nanostructures can also be observed in the materials investigated by transmission electron microscopy (Fig. 3). The diffraction patterns confirm the presence of grains misoriented at large angles. Nanostructures formed as a result of severe plastic deformation qualitatively differ from cellular and fragmented microstructures formed after large regular deformations [6, 7]. It is evident that due to the formation of nanostructures deformation mechanisms under conditions of sample extension may be changed. Actually, in this case, processes occurring at the boundaries of nanograins formed under severe plastic deformation, in particular, grain-boundary sliding, begin to play an active part comparable to the role of lattice-dislocation motion [8].

As is well known, the combination of strength and plasticity is a necessary condition for obtaining potentially useful technological materials. In this connection, attaining very high strength and plasticity in metals and alloys subjected to severe plastic deformation opens up ways of creating fundamentally new structural materials with nanometer-size microstructures. Such nanostruc-

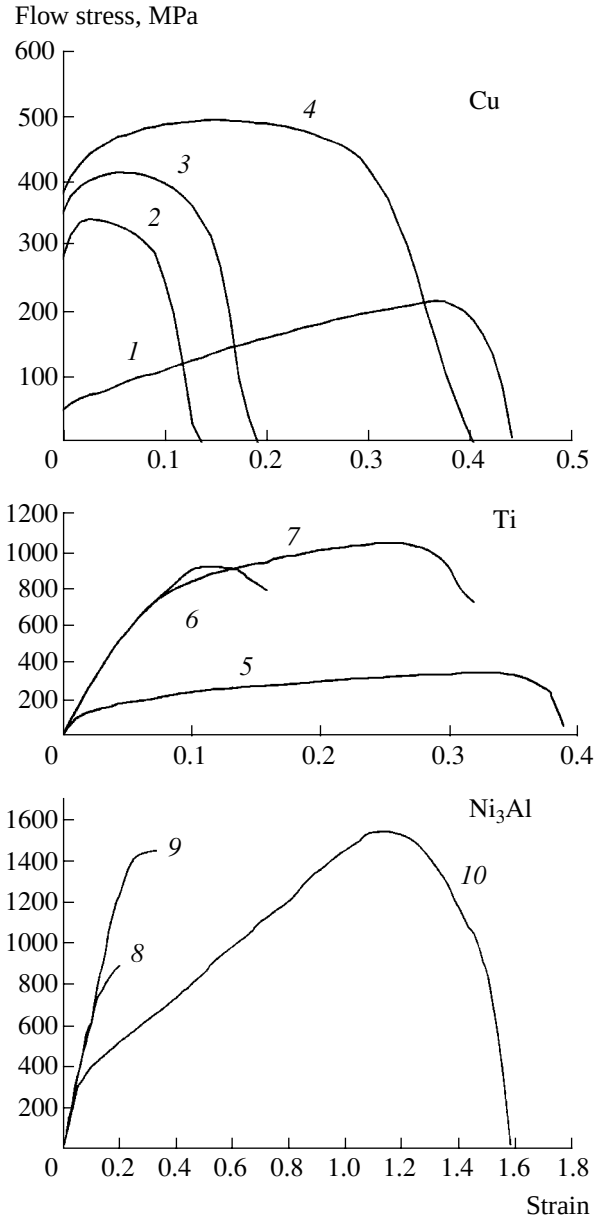

Fig. 2. True-strain curves for three materials under investigation.

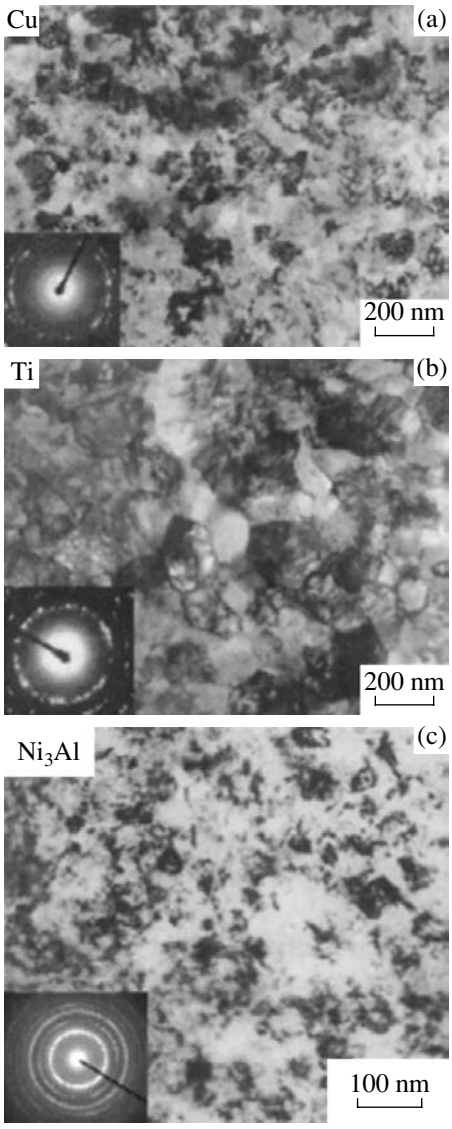

Fig. 3. Electron-microscopy images of nanostructures in the materials under investigation, which were subjected to: (a) equichannel angular pressing (16 passes); (b) torsion under high pressure (5 turns) and holding at 250°C (10 min); (c) torsion under high pressure (5 turns) and heating up to 650°C.

ture materials may possess noticeably higher strength, impact toughness, and fatigue endurance when compared to conventional, widely used commercial materials.

REFERENCES

1. E. Schmid and W. Boas, *Plasticity of Crystals, with Special Reference to Metals* (Chapman and Hall, London, 1968).
2. V. S. Zolotorevskiĭ, *Mechanical Properties of Metals* (Mosk. Inst. Stali i Splavov, Moscow, 1998).
3. R. Z. Valiev, R. K. Islamgaliev, and I. V. Alexandrov, Prog. Mater. Sci. **45** (2), 103 (2000).
4. R. Z. Valiev and I. V. Aleksandrov, *Nanostructural Materials Obtained by Severe Plastic Deformation* (Logos, Moscow, 2000).
5. *Investigations and Applications of Severe Plastic Deformation*, Ed. by T. S. Lowe and R. Z. Valiev (Kluwer, Dordrecht, 2000), NATO ASI Series, Partnership Subseries 3, High Technology **80**, 394 (2000).
6. V. V. Rybin, *Large Plastic Deformations and Fracture of Metals* (Metallurgiya, Moscow, 1986).
7. N. Hansen and J. D. Jensen, Philos. Trans. R. Soc. London, Ser. A **357**, 1447 (1999).
8. R. Z. Valiev, E. V. Kozlov, Yu. F. Ivanov, *et al.*, Acta Metall. Mater. **42**, 2467 (1994).

Translated by Yu. Vishnyakov

Doklady Physics, Vol. 46, No. 9, 2001, pp. 636–641. Translated from Doklady Akademii Nauk, Vol. 380, No. 2, 2001, pp. 183–188.

TECHNICAL PHYSICS

The Problem of Surface-Wave Localization by a Thin Anisotropic Layer

Academician V. A. Babeshko and V. V. Buzhan

Received February 15, 2001

1. We consider the problem of the interaction of elastic waves with an inhomogeneous interface between two solid bodies. These problems are of current interest in geophysics, acoustics, and nondestructive strength tests. In [5, 6], an interface in the form of a thin isotropic layer free of inhomogeneities was used. In this paper, we adopted a model of an interface with defects that was proposed in [1]. The model is based on the study of a thin layer with numerous small cylindrical inclusions aligned in a certain direction. Under such conditions, the material of the layer becomes anisotropic and its behavior is described by the following relation between the displacement–stress vector $\mathbf{U} = (u_x, u_y, u_z, \sigma_{zz}, \sigma_{zy}, \sigma_{zx})^{\mathrm{T}}$ in the upper half-space and a similar vector $\mathbf{U}'$ in the lower half-space:

$$\mathbf{U} = B\mathbf{U}', \quad B = \begin{bmatrix} B_1 & B_2 \\ B_3 & B_4 \end{bmatrix}. \tag{1}$$

Here, u_j are the displacement vector components; i.e., $\mathbf{u} = (u_x, u_j, u_z)$, and σ_{ij} is the stress tensor. The layer material is assumed to be orthotropic in the (x_0, y_0, z) coordinate system, with the (x_0, y_0) plane coinciding with the layer surface and the inhomogeneities aligned in the x_0-direction. The elastic properties of the material are described by the elastic tensor C_{ij}^0 entering in the linear relationships of the generalized Hooke law.

We use the series expansion of the matrix B (see [1]):

$$B = I - i\kappa hA - \frac{1}{2}(\kappa hA)^2 + \frac{i}{6}(\kappa hA)^3 + \ldots, \tag{2}$$

$$A = \begin{bmatrix} 0 & 0 & 1 & 0 & a_{15} & a_{16} \\ 0 & 0 & 0 & 0 & a_{25} & a_{15} \\ a_{31} & a_{32} & 0 & a_{34} & 0 & 0 \\ 0 & 0 & a_{43} & 0 & 0 & 1 \\ a_{51} & a_{52} & 0 & a_{32} & 0 & 0 \\ a_{61} & a_{51} & 0 & a_{31} & 0 & 0 \end{bmatrix}, \tag{3}$$

$$a_{15} = -\frac{\tau_{45}}{i\kappa}, \quad a_{16} = -\frac{\tau_{44}}{i\kappa},$$

$$a_{25} = -\frac{\tau_{55}}{i\kappa}, \quad a_{31} = \frac{C_{13}}{C_{33}}, \quad a_{32} = \frac{C_{36}}{C_{33}},$$

$$a_{34} = -\frac{1}{i\kappa C_{33}}, \quad a_{43} = \frac{\rho_0\omega^2}{i\kappa},$$

$$a_{51} = i\kappa\lambda_{16}, \quad a_{52} = \frac{\rho_0\omega^2}{i\kappa}\left(1 - \frac{\lambda_{66}}{\rho_0 v_{\mathrm{ph}}^2}\right),$$

$$a_{61} = \frac{\rho_0\omega^2}{i\kappa}\left(1 - \frac{\lambda_{11}}{\rho_0 v_f^2}\right),$$

$$\tau_{44} = \frac{C_{44}}{C_{44}C_{55} - C_{45}^2}, \quad \tau_{55} = \frac{C_{55}}{C_{44}C_{55} - C_{45}^2},$$

$$\tau_{45} = -\frac{C_{45}}{C_{44}C_{55} - C_{45}^2}, \quad \lambda_{ij} = C_{ij} - \frac{C_{i3}C_{j3}}{C_{33}}.$$

Here, h is the layer thickness; $v_{\mathrm{ph}} = \dfrac{\omega}{\kappa}$ is the phase velocity; $\omega = 2\pi f$ is the angular frequency; f is the frequency in Hz; $\kappa = \kappa_i \sin\theta_i$ is the component of the wave vector in the plane $z = 0$; κ_i is the wave number; θ_i is the angle of incidence for a wave; ρ_0 is the layer density; $\kappa h = \kappa_i h \sin\theta_i = \dfrac{2\pi h}{\lambda_i}\sin\theta_i$; and C_{ij} is the elastic tensor in the (x, y, z) coordinate system, with the (x, y) plane coinciding with the layer surface. The plane of incidence for elastic waves, (x, z), is inclined at an angle φ to the (x_0, z) plane. The tensor C_{ij} is related to C_{ij}^0 by the formula

$$C = PC^0P^{\mathrm{T}}. \tag{4}$$

The representation of the matrix P was given in [1].

Kuban State University,
ul. Karla Libknekhta 9, Krasnodar, 350640 Russia

1028-3358/01/4609-0636$21.00

Let one of the following conditions be satisfied: the angle of incidence is close to vertical, the wavelength λ_i of the incident wave is much longer than the layer thickness h, or these waves are emitted at a low frequency. In this case, we keep in expansion (2) only terms up to a certain order in powers of κh to provide sufficient accuracy. In addition, we introduce approximate boundary conditions. In what follows, we use, as was done previously in [5, 6], the first approximation.

We assume that the field of monochromatic plane waves incident on the interface is described in the upper half-space by a superposition of the longitudinal waves (hereafter, the factor $\exp[-i\omega t]$ is omitted):

$$\mathbf{u}_{li} = A_l \mathbf{n}_1 \exp(i\kappa_{21}\mathbf{n}_1, \mathbf{r})$$

and transverse waves:

$$\mathbf{u}_{ti} = \mathbf{u}_{SVi} + \mathbf{u}_{SHi}.$$

Here,

$$\mathbf{u}_{SVi} = A_{SV}(\mathbf{n}_2 \times \mathbf{e}_2)\exp(i\kappa_{22}\mathbf{n}_2, \mathbf{r})$$

and

$$\mathbf{u}_{SHi} = A_{SH}\mathbf{e}_2 \exp(i\kappa_{22}\mathbf{n}_2, \mathbf{r})$$

are the fields of the SV waves and SH waves, respectively; A_l, A_{SV}, and A_{SH} are the corresponding amplitudes; $\mathbf{n}_j$ is the normal to the wave front; $\mathbf{r} = (x, y, z)$ is the coordinate vector; κ_{ij} are the wave numbers (the components with $i = 1$ and $i = 2$ correspond to the lower and upper half-spaces, and those with $j = 1$ and $j = 2$ to the longitudinal and transverse waves, respectively); and $\mathbf{e}_2 = (0, 1, 0)$. The unknown displacements are sought as Fourier integral expansions in the lower and upper half-spaces, respectively:

$$u_x'(x, z) = \frac{1}{2\pi}\int_{-\infty}^{\infty}[-i\beta c_{11}e^{\alpha_{11}z} + \alpha_{12}c_{12}e^{\alpha_{12}z}]e^{-i\beta x}d\beta,$$

$$u_y' = \frac{1}{2\pi}\int_{-\infty}^{\infty} d_1(\beta)e^{\alpha_{12}z - i\beta x}d\beta, \qquad (5)$$

$$u_z'(x, z) = \frac{1}{2\pi}\int_{-\infty}^{\infty}[\alpha_{11}c_{11}e^{\alpha_{11}z} + i\beta c_{12}e^{\alpha_{12}z}]e^{-i\beta x}d\beta,$$

$$u_x(x, z) = \frac{1}{2\pi}\int_{-\infty}^{\infty}[-i\beta c_{21}e^{-\alpha_{21}z}$$

$$-\alpha_{22}c_{22}e^{-\alpha_{22}z}]e^{-i\beta x}d\beta + u_{ix},$$

$$u_y = \frac{1}{2\pi}\int_{-\infty}^{\infty} d_2(\beta)e^{-\alpha_{22}z - i\beta x}d\beta + u_{iy}, \qquad (6)$$

$$u_z(x, z) = \frac{1}{2\pi}\int_{-\infty}^{\infty}[-\alpha_{21}c_{21}e^{-\alpha_{21}z}$$

$$+ i\beta c_{22}e^{-\alpha_{22}z}]e^{-i\beta x}d\beta + u_{iz}.$$

Here, u_{ix}, u_{iy}, and u_{iz} are the incident-field components and $\alpha_{ij} = \sqrt{\beta^2 - \kappa_{ij}^2}$.

Let the properties of the layer depend on the sign of x_0 and be described by the matrices B and B' for $x_0 < 0$ and $x_0 > 0$, respectively. The matrix B' contains the same elements as the matrix B, but these are marked by primes. To determine the unknown coefficients in relationships (5) and (6), we employ the approach described in [5], which leads to the system of six functional equations of the sixth order

$$(I + Q_0)\mathbf{X}^- = \mathbf{X}^+ + Q_0\mathbf{L}. \qquad (7)$$

Here, I is the identity matrix;

$$Q_0 = \begin{bmatrix} -N_1Q_1^{-1} & N_1Q_1^{-1}P_2 \\ -N_2Q_1^{-1} & N_2Q_1^{-1}P_2 \end{bmatrix},$$

$$Q_1 = [P_2(B_3'P_1 + B_4') - (B_1'P_1 + B_2')],$$

$$P_k = W_k\Pi_m^{-1}, \qquad (8)$$

$$N_1 = (B_1 - B_1')P_1 + B_2 - B_2',$$

$$N_2 = (B_3 - B_3')P_1 + B_4 - B_4';$$

$$W_1 = \begin{bmatrix} -i\beta & 0 & \alpha_{12} \\ 0 & 1 & 0 \\ \alpha_{11} & 0 & i\beta \end{bmatrix}, \quad W_2 = \begin{bmatrix} -i\beta & 0 & -\alpha_{22} \\ 0 & 1 & 0 \\ -\alpha_{21} & 0 & i\beta \end{bmatrix},$$

$$\Pi_1 = \begin{bmatrix} (\lambda_1 + 2\mu_1)\alpha_{11}^2 - \lambda_1\beta^2 & 0 & 2i\mu_1\beta\alpha_{12} \\ 0 & \mu_1\alpha_{12} & 0 \\ -2i\mu_1\beta\alpha_{11} & 0 & \mu_1(\beta^2 + \alpha_{12}^2) \end{bmatrix}, \qquad (9)$$

$$\Pi_2 = \begin{bmatrix} (\lambda_2 + 2\mu_2)\alpha_{21}^2 - \lambda_2\beta^2 & 0 & -2i\mu_2\beta\alpha_{22} \\ 0 & -\mu_2\alpha_{22} & 0 \\ 2i\mu_2\beta\alpha_{21} & 0 & \mu_2(\beta^2 + \alpha_{22}^2) \end{bmatrix},$$

$$\mathbf{L} = \begin{pmatrix} \mathbf{L}_1 \\ \mathbf{L}_2 \end{pmatrix}, \quad \mathbf{L}_k = \mathbf{L}_k^+ + \mathbf{L}_k^-,$$

$$\mathbf{L}_k^+ = \int_0^\infty (\mathbf{j}_k + \mathbf{i}_k) e^{i(\kappa+\beta)x} dx,$$

$$\mathbf{L}_k^- = \int_{-\infty}^0 (\mathbf{j}_k + \mathbf{i}_k) e^{i(\kappa+\beta)x} dx.$$

The superscripts "+" and "–" signify that the function is analytically extendable along β to the upper and lower half-spaces, respectively. Here,

$$\mathbf{j}_1 = A_l \mathbf{n}_1, \quad \mathbf{i}_1 = A_{SH}\mathbf{e}_2 + A_{SV}(\cos\theta_2 \mathbf{e}_1 + \sin\theta_2 \mathbf{e}_3),$$

$$\mathbf{j}_2 = i\kappa_{21} A_l [\lambda \mathbf{e}_3 - 2\mu \cos\theta_1 \mathbf{n}_1],$$

$$\mathbf{i}_2 = -i\mu\kappa_{22}[A_{SH}\cos\theta_2 \mathbf{e}_2 + A_{SV}\{\cos 2\theta_2 \mathbf{e}_1 + \sin 2\theta_2 \mathbf{e}_3\}],$$

$$\mathbf{e}_1 = (1, 0, 0), \quad \mathbf{e}_3 = (0, 0, 1),$$

and θ_1 and θ_2 are the angles of incidence for the longitudinal and transverse waves, respectively.

The desired vector–functions $\mathbf{C}_k$,

$$\mathbf{C}_1 = \begin{pmatrix} c_{11} \\ d_1 \\ c_{12} \end{pmatrix}, \quad \mathbf{C}_2 = \begin{pmatrix} c_{21} \\ d_2 \\ c_{22} \end{pmatrix}, \tag{10}$$

are expressed in terms of the vector functions $\mathbf{X}^\pm = (\mathbf{X}_1^\pm, \mathbf{X}_2^\pm)^T$:

$$\mathbf{C}_k = \Pi_k^{-1}\mathbf{S}_k, \quad \mathbf{S}_1 = N_1^{-1}(\mathbf{X}_1^- - \mathbf{X}_1^+),$$

$$\mathbf{S}_2 = (B_3' P_1 + B_4')N_2^{-1}(\mathbf{X}_2^- - \mathbf{X}_2^+) + \mathbf{X}_2^- - \mathbf{L}_2.$$

2. The application of the Wiener–Hopf method to the system of equations (7) is reduced to the left-hand-side factorization of the matrix function $Q = I + Q_0$ of the sixth order with respect to the contour that coincides with the real axis almost everywhere and bypasses real singularities in the left and right half-planes from above and from below, respectively [2]:

$$Q = Q_+ Q_-.$$

Poles, branch points, and zeros of the matrix determinant are real singularities. After factorization of the matrix Q, the solution to the problem can easily be written out. However, there are no methods for the exact factorization of general-form matrices. Therefore, approximate methods should be used; namely, elements of an initial matrix should be approximated by rational functions. The matrix obtained in this manner can be factorized exactly [2].

Sometimes, analysis of the matrix being factorized makes it possible to conclude that its elements off the main diagonal are close to zero. In this case, the initial matrix can be approximated by a diagonal matrix whose factorization is easily performed by factorizing its diagonal elements, i.e., its scalar functions. Such a method allows the contribution of surface waves into the total field near the interface to be separated from the general integral solution as a residue in the real root of the corresponding dispersion equation. As an example, we consider an interface layer (similar to that treated in [5]) whose elastic properties vary along the boundary:

$$B_1 = B_1', \quad B_3 = B_3', \quad B_2 \neq B_2', \quad B_4 = B_4'.$$

Properties of the half-spaces are assumed to be identical. In this case, the set of equations (7) is reduced to the system of the third order:

$$(I - N_1 Q_1^{-1})\mathbf{X}_1^- = \mathbf{X}_1^+ + N_1 Q_1^{-1} P_2 \mathbf{L}_1. \tag{11}$$

In contrast to the plane problem considered in [5], the matrix $T = I - N_1 Q_1^{-1}$ of system (11) cannot be reduced to the diagonal form (i.e., the system is not decomposed into three independent equations) by the following simplifications: $B_1 = B_1' = I$, $B_3 = B_3' = 0$, and $B_2' = 0$. In dimensionless variables, the matrix T takes the form

$$T = \begin{bmatrix} -\dfrac{F_1(\alpha)}{s_1\alpha_{22}} & \dfrac{\alpha_{22}}{s_4} & 0 \\ \dfrac{\Delta(\alpha)}{s_4\alpha_{22}} & \dfrac{F_3(\alpha)}{s_3} & 0 \\ 0 & 0 & -\dfrac{F_2(\alpha)}{s_2\alpha_{21}} \end{bmatrix}. \tag{12}$$

Here,

$$s_1 = \frac{2}{\tau_{44}\mu\kappa_t h}, \quad s_2 = \frac{2C_{33}}{\mu\kappa_t h},$$

$$s_3 = \frac{2}{\tau_{55}\mu\kappa_t h}, \quad s_4 = \frac{2}{\tau_{45}\mu\kappa_t h};$$

μ is the shear modulus for the elastic half-space; $\kappa_t = \kappa_{12} = \kappa_{22}$; and

$$F_3(\alpha) = \alpha_{22} + s_3, \quad F_j(\alpha) = \Delta(\alpha) - s_j\alpha_{2,3-j}, \quad j = 1, 2,$$

$$\Delta(\alpha) = 4\left[(\alpha^2 - 0.5)^2 - \alpha^2\sqrt{\alpha^2 - 1}\sqrt{\alpha^2 - \varepsilon^2}\right].$$

If the assumptions concerning the matrix elements that were listed at the beginning of this section are valid, the

problem is reduced to the factorization of the functions $F_k(\alpha)$. In particular, it follows from relationship (4) that

$$C_{44} = C_{44}^0\cos^2\varphi + C_{55}^0\sin^2\varphi,$$
$$C_{55} = C_{44}^0\sin^2\varphi + C_{55}^0\cos^2\varphi,$$
$$C_{45} = 0.5(C_{44}^0 - C_{55}^0)\sin 2\varphi.$$

In this case, it is evident that the form of the matrix is close to a diagonal matrix if $C_{44}^0 \approx C_{55}^0$, i.e., if $\varphi \approx 0°$ or $\varphi \approx 90°$.

The factorization of the functions $F_{1,2}(\alpha)$ was performed in [5]. To factorize $F_3(\alpha)$, we employ the same method and introduce the functions

$$H_3(\alpha) = \frac{F_3(\alpha)}{\phi_3^+(\alpha)\phi_3^-(\alpha)}, \quad (13)$$
$$\phi_3^-(\alpha) = a_3\sqrt{\alpha - 1} + d_3\sqrt{\alpha - ig_3},$$
$$\phi_3^+(\alpha) = \phi_3^-(-\alpha) = -i\{a_3\sqrt{\alpha + 1} + d_3\sqrt{\alpha + ig_3}\}.$$

The parameters a_3, d_3, and g_3 are determined from the condition that the characteristic singularities of the functions $F_3(\alpha)$ and $\phi_3^+(\alpha)\phi_3^-(\alpha)$ should be identical. Hence,

$$a_3 = \frac{\sqrt{1 - s_3} - i\sqrt{g_3}}{1 - \sqrt{ig_3}}, \quad d_3 = \frac{\sqrt{i} - \sqrt{i - s_3}}{1 - \sqrt{ig_3}}.$$

The choice of the free parameter g_3 is dictated by the best approximation of the function $H_3(\alpha)$ to unity throughout the real axis. The function $H_3(\alpha)$ obtained in this manner can be factorized exactly in the integral form [2]:

$$H_3^\pm(\alpha) = \exp\left\{\pm\frac{1}{2\pi i}\int_\Gamma \frac{\ln H_3(\zeta)}{\zeta - \alpha}d\zeta\right\}. \quad (14)$$

The contour Γ was defined above. Hence,

$$F_3^\pm(\alpha) = \phi_3^\pm(\alpha)H_3^\pm(\alpha).$$

3. The incidence of a plane wave on the layer surface results in the origination of surface waves propagating along the *x*-direction near the layer surface. There exist two types of these waves: symmetric and antisymmetric. Symmetric waves excite antiphase oscillations of particles along the *z*-direction and in-phase oscillations along the directions of the *x*- and *y*-axes, and the reverse holds for antisymmetric waves. If the direction of the wave propagation coincides with the symmetry axis (i.e., with the direction of the x_0-axis or y_0-axis), then, as follows from (12), the equations

$$F_1(\alpha) = 0 \quad \text{and} \quad F_3(\alpha) = 0 \quad (15)$$

are the dispersion equations, respectively, for the antisymmetric modes with P–SV and SH polarizations.

The first equation in (15) has a single real root [5, 7]. The second equation has no real roots, because the mode-propagation condition requires that $\alpha > 1$; hence, the radical α_{22} is purely real-valued. The equation

$$F_2(\alpha) = 0 \quad (16)$$

is the dispersion equation for the symmetric mode with P–SV polarization that, under certain conditions, could have a single real root [7]. If the propagation direction for a wave does not coincide with the symmetry axis, then, as follows from (12), the dispersion equation, in general, cannot be reduced to independent equations for modes with P–SV and SH polarizations (see also [1]).

The dispersion equation for the symmetric mode with SH polarization can also be derived from the matrix of the system of equations (7), provided that the inertia properties of the interface layer vary along the boundary [6]:

$$B_1' = B_1, \quad B_2' = B_2, \quad B_3' \neq B_3, \quad B_4 \neq B_4'.$$

This matrix has a similar structure to that considered above, while the dispersion equation takes the form

$$G_3(\alpha) \equiv 1 - q_3\alpha_{22} = 0, \quad q_3 = \frac{2\rho v_t}{\omega M_{pSH}}. \quad (17)$$

Here, v_t is the velocity of the transverse wave in the half-space; $M_{pSH} = M_n\left(1 - \frac{C_{66}^0}{\rho_0 v_{ph}^2}\right)$ is the effective mass of a thin plate, which describes its inertia properties along the direction orthogonal to the plane of incidence; and $M_n = \rho_0 h$ is the plate mass per unit area. In contrast to the antisymmetric mode, Eq. (17) possesses a single real root

$$\alpha_3 = q_3^{-1}\sqrt{1 + q_3^2}.$$

The factorization of $G_3(\alpha)$ is performed in the same manner as that for $F_3(\alpha)$:

$$G_3^\pm(\alpha) = \psi_3^\pm(\alpha)R_3^\pm(\alpha). \quad (18)$$

Here, $R_3^\pm(\alpha)$ is determined by the integral formula (14) with the function $R_3(\alpha)$ substituted for $H_3(\alpha)$:

$$R_3(\alpha) = \frac{G_3(\alpha)}{\psi_3^+(\alpha)\psi_3^-(\alpha)},$$

$$\psi_3^-(\alpha) = b_3\sqrt{\alpha-1} - c_3\sqrt{\alpha - it_3},$$

$$\psi_3^+(\alpha) = \psi_3^-(-\alpha) = i\{b_3\sqrt{\alpha+1} - c_3\sqrt{\alpha + it_3}\},$$

$$b_3 = \frac{q_3(1-\alpha_3) - i}{2[\sqrt{1+iq_3} - \alpha_3\sqrt{iq_3}]},$$

$$c_3 = \frac{q_3(1+\alpha_3) + i(2\sqrt{q_3(i-q_3)} - 1)}{2[\sqrt{1+iq_3} - \alpha_3\sqrt{iq_3}]},$$

$$t_3 = \left[\frac{i - q_3(\alpha_3+1) - 2i\alpha_3\sqrt{q_3(i-q_3)}}{q_3(\alpha_3+1) - i + 2i\sqrt{q_3(i-q_3)}}\right]^2.$$

4. In our numerical evaluations, we use the following parameters borrowed from paper [1]:

1. For the elastic half-space, v_l = 6.2 km/s, v_t = 3.24 km/s, and ρ = 2.7 g/cm^3, where v_l is the longitudinal-wave velocity;

2. For the interface layer having the porosity of 30%, $C_{44}^0 = 11.2 \times 10^9$ N/m^2, $C_{55}^0 = C_{66}^0 = 15.2 \times 10^9$ N/m^2, and ρ_0 = 1.89 g/cm^3;

3. $\theta_1 = 45°$, fh = 0.1 MHz mm.

The exact values of the functions F_3^- (with $g_3 = 40$) and R_3^- evaluated by formula (14) are shown in Figs. 1 and 2, respectively. Based on these factorizations, we evaluated the interface wave amplitudes. The amplitudes of the antisymmetric mode with P–SV polarization propagating along the x_0-direction are plotted in Fig. 3. The numbers of the curves correspond to various values of the parameter $\varepsilon = \frac{v_t}{v_l}$. The maxima arising in the range $0.1 < \kappa_t h < 0.3$ of the dimensionless frequencies can testify, for example, to the existence of a range of optimum frequencies for the ultrasonic monitoring of welded joints. The amplitude of the symmetric mode

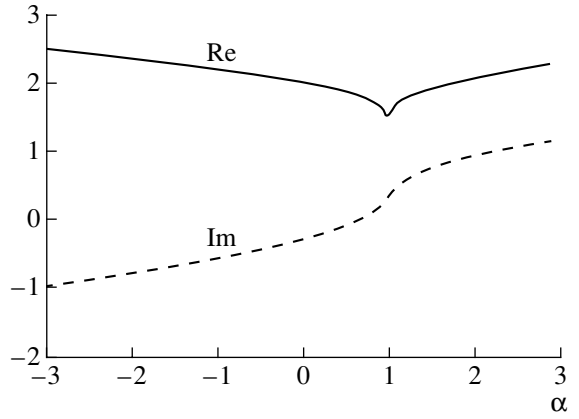

Fig. 1. Real (solid line) and imaginary (dashed line) components of the function $F_3^-(\alpha)$ for $g_3 = 40$.

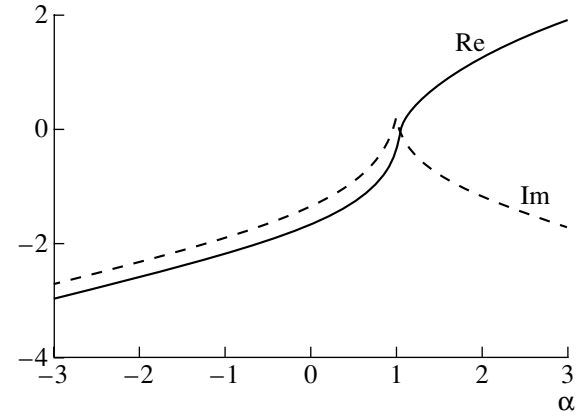

Fig. 2. Real (solid line) and imaginary (dashed line) components of the function $R_3^-(\alpha)$.

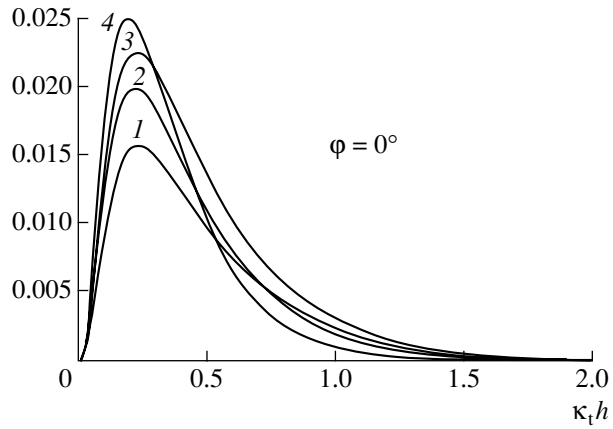

Fig. 3. Amplitude of the antisymmetric mode with P–SV polarization propagating along the x_0-direction and (*1*) ε = 0.2; (*2*) 0.3; (*3*) 0.5; and (*4*) 0.7.

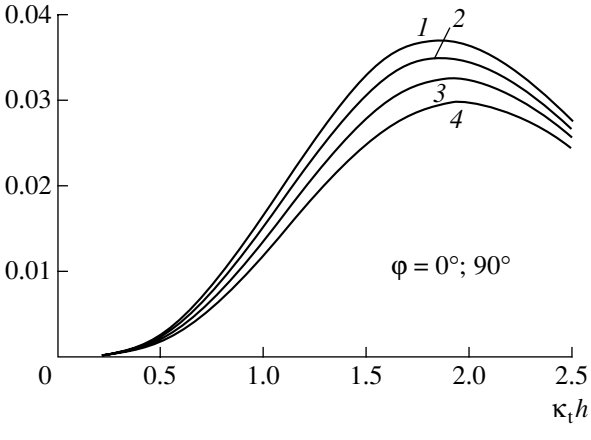

Fig. 4. Amplitude of the symmetric mode with SH polarization and (*1*) ε = 0.2; (*2*) 0.3; (*3*) 0.4; and (*4*) 0.5.

with SH polarization is shown in Fig. 4. As can be seen, the resonance frequencies fall in the range $1.7 < \kappa_t h < 2$.

ACKNOWLEDGMENTS

This work was supported by the Russian Foundation for Basic Research, project nos. 99-01-00787 and 00-01-96019 (r-2000, South), as well as by the CRD Foundation, project REC-004.

REFERENCES

1. W. Huang and S. I. Rokhlin, Geophys. J. Int. **118**, 285 (1994).
2. I. I. Vorovich and V. A. Babeshko, *Dynamical Mixed Problems of the Theory of Elasticity for Nonclassical Fields* (Nauka, Moscow, 1979).
3. B. Noble, *Methods Based on the Wiener–Hopf Technique for the Solution to Partial Differential Equations* (Pergamon, Oxford, 1958; Inostrannaya Literatura, Moscow, 1962).
4. L. M. Brekhovskikh and O. A. Godin, *Acoustics of Layered Media* (Nauka, Moscow, 1989; Springer, New York, 1990).
5. V. A. Babeshko, S. I. Rokhlin, V. Huang, and V. V. Buzhan, Dokl. Akad. Nauk **337**, 732 (1994) [Phys. Dokl. **39**, 566 (1994)].
6. V. A. Babeshko, V. V. Buzhan, E. M. Gorshkova, and S. I. Rokhlin, Dokl. Akad. Nauk **353,** 327 (1997) [Phys. Dokl. **42**, 132 (1997)].
7. V. A. Babeshko, V. V. Buzhan, E. M. Gorshkova, and S. I. Rokhlin, Izv. Vyssh. Uchebn. Zaved. Sev.-Kavk. Reg., Estestv. Nauki, No. 4, 24 (2000).

Translated by V. Chechin

Doklady Physics, Vol. 46, No. 9, 2001, pp. 642–646. Translated from Doklady Akademii Nauk, Vol. 380, No. 2, 2001, pp. 189–193.

TECHNICAL PHYSICS

Algorithms of Robust Image Filtering with the Preservation of Fine Details in the Presence of Noise

V. F. Kravchenko*, V. I. Ponomarev, and Corresponding Member of the RAS V. I. Pustovoĭt*****

Received April 6, 2001

1. Generally, the image quality of objects under remote sensing is poor when the data are interpreted in applications [1]. Nonlinear filters normally provide restoration of the contours of large-scale objects in an image [2–5] without correcting its small-scale details.

In the present paper, new robust nonlinear algorithms of image filtering are presented that ensure the retention of small-scale details and yet suppress pulse and multiplicative noises. These algorithms employ filters of the *RMKNN*-type (rank maximum likelihood filters of *K* nearest neighbors) introduced in [6, 7] with the simplest cutoff function or with the cut-median or Hampel functions [5].

Realization of the proposed *RMKNN* algorithms on the basis of digital signal processing with the use of a DSP TMS320C6701 processor [8] experimentally confirmed the feasibility of the image filtering in real time under various noise conditions.

2. We use the image distortion model previously described in [7, 9]:

$$u(x, y) = N_{\text{pul}}(\varepsilon_{\text{multi}}(x, y)e(x, y)). \quad (1)$$

Here,

$$N_{\text{pul}}(e(x, y)) = \begin{cases} \text{a random pulse, with the appearance probability } P_i \\ e(x, y) \text{ otherwise,} \end{cases}$$

$\varepsilon_{\text{multi}}(x, y)$ is multiplicative noise; $e(x, y)$ is a true image; $u(x, y)$ is the result of the image distortion by the pulse and multiplicative noises; and $N_{\text{pul}}(e(x, y))$ is a functional determining the influence of the pulse noise on the image.

The present task is to elaborate a robust-filtering algorithm capable of eliminating the pulse and multiplicative noises and reconstructing small-scale details of an image. It was shown in [5, 6] that the reduced robust *M*-estimate for the mean value of *X*-sample with the one-step scheme is determined by the combined *RM*-estimate:

$$\theta_{\text{med}M} = \text{med}\{X_i\tilde{\psi}(X_i - \theta^{(0)}), i = 1, \ldots, n\}. \quad (2)$$

Here, $\theta^{(0)}$ is the mean value of the sample; the cutoff function $\tilde{\psi}(X)$ is chosen in such a way that the required level of robustness should be achieved. The function

$$\tilde{\psi}_{\text{cut}}(X) = \begin{cases} X, |X| \le r \\ 0, |X| > r, \end{cases}$$

determined by the robust Huber *M*-estimate for the normal distribution with long tails, was employed in [6, 9].

A function picking out *K* neighboring pixels whose values are nearest to the central element $u(i, j)$ of a filtering window is a simple version of the function $\tilde{\psi}(X)$. In this case, the well-known filtering *KNN* algorithm is easily realized if, at the first iteration step, the central pixel (element) is chosen in the form $\theta^{(0)} = u(i, j)$ [9]:

$$\hat{e}_{KNN}(i, j) = \frac{1}{\sum_{m=-L}^{L}\sum_{n=-L}^{L}\tilde{\psi}(u(i+m, j+n))} \times \sum_{m=-L}^{L}\sum_{n=-L}^{L}\tilde{\psi}(u(i+m, j+n))u(i+m, j+n). \quad (3)$$

Here, $\hat{e}_{KNN}(i, j)$ is the image estimate,

$$\tilde{\psi}(u(i+m, j+n)) = \begin{cases} 1, \text{ if } u(i+m, j+n) \text{ is one of the } K \text{ elements} \\ \text{nearest to } u(i, j) \\ 0, \text{ otherwise.} \end{cases}$$

It was shown in [8, 9] that the robust properties of a standard filtering *KNN*-algorithm (3) may be improved if, instead of the arithmetical mean in the one-step algo-

* *Institute of Radio Engineering and Electronics, Russian Academy of Sciences, ul. Mokhovaya 18, Moscow, 103907 Russia*

** *National Polytechnical Institute of Mexico, Mexico City, e-mail: vponomar@calmecac.esimecu.ipn.mx*

*** *Central Design Bureau of Unique Instrumentation, Russian Academy of Sciences, ul. Butlerova 15, Moscow, 117342 Russia*

1028-3358/01/4609-0642$21.00

rithm of the *RM*-estimate, the central pixel is reused as the first iteration of the following estimate:

$$\hat{e}_{MMKNN}(i, j) = \text{med}\{u_{KNN}(i + m, j + n)\}. \quad (4)$$

Here, $u_{KNN}(i + m, j + n)$ is a set of the K pixels nearest to $u(i, j)$, $m, n = -L, \ldots, L$ inside the filter window.

The median version of the *RMKNN*-filter (4) proved to be the most convenient for the processing of images of a diverse physical nature [7, 9]. Such a filter (*MMKNN* is an acronym for "maximum likelihood median filter of K nearest neighbors") can be written out in the following form:

$$\hat{e}_{MMKNN}(i, j) = \text{med}\{g^{(q)}(i + m, j + n)\}. \quad (5)$$

Here, $g^{(q)}(i + m, j + n)$ is the set of K_c pixels weighted with the $\tilde{\psi}(X)$-function, which are used inside the filtering window and close to the estimate $\hat{e}^{(q-1)}_{MMKNN}(i, j)$ at the previous step. Here, $m, n = -L, L$; $\hat{e}^{(0)}_{MMKNN}(i, j) = u(i, j)$; $u(i, j)$ is the original image; $(2L + 1)^2$ is the filtering-window size; q is the index of the current iteration; $\hat{e}^{(q)}_{MMKNN}$ is the estimate at the qth iteration; and $K_c(i, j)$ is the current number of the nearest pixels. This number accounts for local data activity and the presence of spikes in the filtering window; it is determined as follows:

$$K_c(i, j) = K_{\min} + aS(u(i, j)) \le K_{\max}. \quad (6)$$

Here,

$$S(u(i, j)) = \frac{\text{med}\{|u(i, j) - u(i + m, j + n)|\}}{\text{MADM}\{u(i, j)\}} + 0.5\frac{\text{MADM}\{u(i, j)\}}{\text{med}\{u(i + k, j + l)\}}.$$

The a-parameter controls the sensitivity of the filtering algorithm to local data variations near the contour of an object. The maximum number, $K_{\max}$, of pixels neighboring the central element determines the smoothness of the contour and the preservation of fine details of an image. MADM is an acronym for "the median of absolute deviations from the median".

The filtering algorithm proposed is a generalization of a standard *KNN*-filter (3), being its equivalent in the case of $q = 1$ and $a = 0$.

Only the simplest cutoff function $\tilde{\psi}_{\text{cut}}(X)$ introduced above was employed in the *RM*-type filters described in [9]. A number of other cutoff functions for reduced *M*-estimates are known (see [2–5]): the Andrus sine, the Tuky function, the Bernoulli function, etc.

In this paper, other cutoff functions $\tilde{\psi}(X)$ are employed in the algorithms for the *MMKNN*-filter (5). It was shown in [2, 5] that the most robust version of the reduced *M*-estimate is the cut median:

$$\tilde{\psi}_{\text{med}(r)}(X) = \text{sgn}(X) \times 1_{[-r, r]}(X) = \begin{cases} \text{sgn}(X), & |X| \le r \\ 0, & X > r. \end{cases} \quad (7)$$

Thus, employment of function (7) could result in efficient noise suppression because of the robustness of such an estimate.

We also employ the Hampel function represented in the following form:

$$\Psi_{\alpha, \beta, r}(X) = \begin{cases} X, 0 \le |X| \le \alpha \\ \alpha\text{sgn}(X), \alpha \le |X| \le \beta \\ \alpha\dfrac{r - |X|}{r - \beta}, \quad \beta \le |X| \le r \\ 0, \quad r \le |X|. \end{cases} \quad (8)$$

Here, $0 < \alpha < \beta < r < \infty$.

Cutoff functions (7) and (8) were used in the *MMKNN*-filter (5) in order to sufficiently suppress pulse noise.

To reduce the influence of multiplicative noise [9], another robust filter was proposed, whose algorithm is of the following form:

$$\hat{e}_M(i, j) = \frac{\sum_{m=-L}^{L}\sum_{n=-L}^{L} u(i, j)\tilde{\psi}'\{u(i + m, j + n) - \hat{e}^{(0)}(i, j)\}}{\sum_{k=-L}^{L}\sum_{l=-L}^{L} \tilde{\psi}'\{u(i + m, j + n) - \hat{e}^{(0)}(i, j)\}}. \quad (9)$$

Here,

$$\tilde{\psi}'\{u(i + m, j + n) - \hat{e}^{(0)}(i, j)\} = \begin{cases} 1, & |u(i + m, j + n) - \hat{e}^{(0)}(i, j)| \le b\text{med}\{u(i, j)\} \\ 0, \text{ otherwise}, \end{cases}$$

$\text{med}\{u(i, j)\}$ is the median of a sample of values inside the filtering window; the coefficient b controls the multiplicative noise suppression; $m, n = -L, \ldots, L$, $2(L + 1)$ determine the sizes of the filtration window and $\hat{e}^0(i, j) = \hat{e}_{MMKNN}(i, j)$ is the first iteration. The numerical analysis of algorithm (9) shows that the filtering results weakly depend on b (in what follows, $b = 2$ is taken).

To preserve the small-scale details of an image, an adaptive scheme was proposed that is similar to the one

Table 1. Processing time (in seconds) for various root-mean-square deviation of multiplicative noise and the three filtering functions

Filter	Root-mean-square deviation			
	0.00	0.05	0.10	0.25
The simplest	2.19	2.165	2.16	2.16
Median	2.187	2.21	2.205	2.21
Hampel	2.23	2.26	2.26	2.265

used in the local statistical Lee filter [9]:

$$\hat{e}(i, j) = \hat{e}_{MMKNN}(i, j)Q(i, j) + (1 - Q(i, j))\hat{e}_M(i, j),$$
$$Q(i, j) = 1 - \left(c\frac{\hat{e}_M(i, j)}{\mathrm{med}\{|\hat{e}_M(i, j) - u(i + m, j + n)|\}}\right)^2. \quad (10)$$

Here, the function $Q(i, j)$ is the robust estimate of the local sample activity, and the coefficient c controls restoration of the fine details of an image.

It is worth noting that algorithm (9) is analyzed in the case when cutoff functions (7) and (8) are employed. Consequently, the resulting processing filter (10) is determined by two filters. One of them is the *MMKNN*-filter (5) and (6), which provides the suppression of pulse noise and the preservation of fine details of an image; the other is the *M*-filter (10), which suppresses multiplicative noise.

3. The above-mentioned algorithms were actualized using a Texas Instruments TMS320C6701 floating-point processor, which records and processes signals [8]. The test picture "Automobile" (infrared 256×256 image) [8] was used for finding specific values of the processing time for the filters described above. The data was distorted by a pulse noise, which comprised 15%, and mixed with a multiplicative noise of various root-mean-square deviations. Then, the distorted data were used for filtering. In Table 1, we list experimentally found values of time for both of the filters (*MMKNN* and *M*) with the three functions: simplest, cut-median, and Hampel functions. It is easily seen that the processing time required for the algorithm with the simplest function is shorter than that with either the cut-median or Hampel functions. The processing times for the filters employing the functions under consideration were longer than those for a simple median filter with a 5×5 window size, the latter being 0.3881s. The required processing time is one of the important characteristics of the algorithms under study. Another equally important characteristic of an algorithm is the filtering quality, which will be discussed below.

4. We carried out a series of numerical experiments for studying the properties of new algorithms (5) and (10) and for their comparison with the standard 5×5 median filter. We used the root-mean-square deviation

$$\langle |e(x, y) - \hat{e}(x, y)|^2 \rangle$$

as a criterion of the filtering quality.

For evaluating the noise-suppression quality of the filters proposed, the standard image "Mandrill" [1, 3, 5] was distorted by a mixture of multiplicative Gaussian noise and pulse noise. The parameters a from (6) and c from (10) were varied. The minimum values of the root-mean-square deviation found from the numerical experiments are given in Table 2 for the filter with the simplest cutoff function and for the standard 5×5 median filter. In Table 3, the values are for the filters with the cut-median and Hampel functions. For the filters with the cut-median and Hampel functions, the optimum values of the parameters a and c are constant. The parameters α and r entering in the Hampel function are constants. The parameter β, however, differs little for various images and noise levels. In the case of the simplest cutoff function, the optimum values of a and c are found to be virtually invariant under variations of noise parameters. When the cut-median and Hampel functions are employed, the parameter a is virtually constant. The parameter c is equal to 0.01; however, it is not constant but changes from one image to another.

Table 2. The minimum values of root-mean-square deviation for the "Mandrill" image: (numerator) simplest cutoff function and (denominator) standard 5×5 median filter

Pulse noise probability	Root-mean-square deviation for multiplicative noise			
	0	0.05	0.10	0.25
0	144.2/877.7	819.1/1071.0	1015.1/1234.3	1220.721554.7
1	229.3/878.7	834.2/1076.6	1023.9/1249.8	1265.211568.70
5	312.7/909.9	1034.8/1113.9	1027.6/1270.8	1274.9/1569.3
10	418.9/944.3	1047.8/1115.7	1037.0/1325.0	1310.5/1642.7
15	534.4/984.4	1063.9/1194.2	1038.3/1343.6	1362.4/1661.8
20	667.3/1031.4	1070.6/1220.4	1055.8/1430.4	1412.4/1776.9

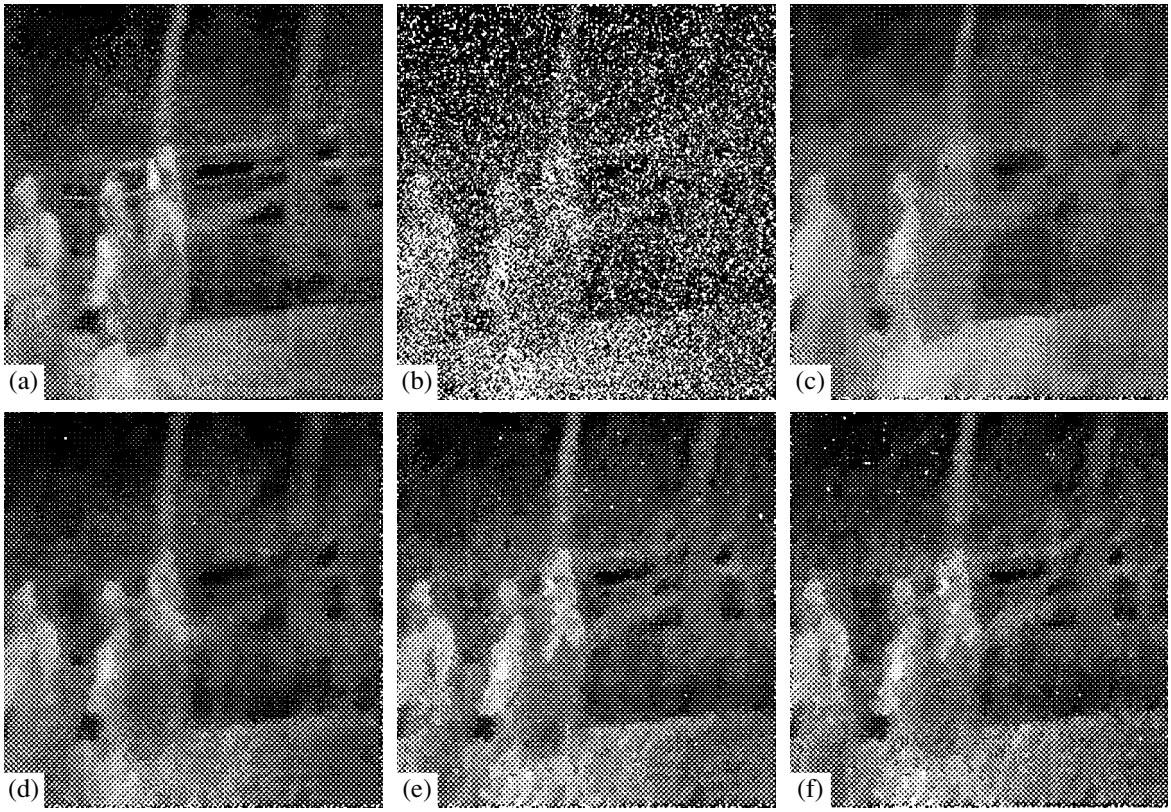

Fig. 1. The results of modeling: (a) test infrared image "People"; (b) noise-polluted image (a) 20% of a pulse noise mixed with a multiplicative Gaussian noise with relative root-mean-square deviation of 0.1; the results of the filtering by (c) standard 5×5 median filter and with (d) simplest cutoff, (e) cut-median, and (f) Hampel functions.

The optimum values for parameters α, β, and r for the Hampel function are $\alpha = 10.00$, $\beta \le 100$, and $r = 300.00$.

The following conclusions can be drawn from the analysis of the numerical experiment: (i) The filtering algorithms proposed provide better noise suppression compared to the 5×5 median filter. The algorithms with the cutoff functions ensure reasonably strong suppression and preserve small-scale image details much better than the median filter. (ii) The filters with the cut-median and Hampel functions provide better noise suppression compared to those with the simplest cutoff function when the level of the root-mean-square deviation for multiplicative noise is greater than 0.01. (iii) The optimum values of parameters a and c for the cut-median and Hampel functions are virtually invariable under variations of noise parameters. (iv) The filters constructed on the basis of the cut-median and Hampel functions show better robust properties compared to the filter with the simplest cutoff function.

Figures 1a–1f show the comparative analysis of the filtering and noise suppression by the developed and standard median filters. Figures 1a and 1b show the

Table 3. The minimum values of root-mean-square deviation for the "Mandrill" image: (numerator) cut-median function and (denominator) Hampel function

Pulse noise probability	Root-mean-square deviation for multiplicative noise			
	0	0.05	0.10	0.25
0	518.9/515.5	738.1/723.9	897.0/886.3	1209.6/1203.8
1	551.8/518.9	745.6/730.6	891.8/878.9	1214.4/1208.8
5	588.6/551.8	768.2/752.9	922.9/910.8	1268.3/1260.4
10	626.0/589.0	806.5/792.8	966.8/955.5	1217.4/1310.8
15	638.9/626.6	843.7/829.6	1004.9/993.3	1378.2/1375.1
20	663.9/644.5	890.1/876.6	1054.1/1043.7	1429.5/1430.4

original and noise-polluted images, respectively. Figures 1c to 1f show the results of image processing with the standard 5×5 median filter and the filters with the simplest cutoff, cut-median, and Hampel functions, respectively.

Thus, new robust nonlinear filters for image processing with various cutoff functions are presented.

The robust filtering algorithms proposed and justified can suppress complicated-structure noise and preserve small-scale details of an image. The algorithms with the filtering functions of the cut-median and Hampel types provide better robustness compared to the filter employing the simplest cutoff function. The optimum algorithm parameters were found for various classes of images and noise characteristics. The experimental study of the digital signal processing for the filters under consideration showed that the filter with the simplest cutoff function is less time-consuming than those with the cut-median and Hampel functions.

The results of this study were partially reported at the International Workshop "Mathematical Modeling of Physical Processes in Inhomogeneous Media" (March 20–22, 2001, Guanajuato, Mexico) [10].

REFERENCES

1. A. A. Goncharenko, V. F. Kravchenko, and V. I. Ponomarev, *Remote Sounding of Inhomogeneous Media* (Mashinostroenie, Moscow, 1991).
2. I. Pitas and A. N. Venetsanopoulos, *Nonlinear Digital Filters: Principles and Applications* (Kluwer, Dordrecht, 1990).
3. J. Astola and P. Kuosmanen, *Fundamentals of Nonlinear Digital Filtering* (CRC Press, Boca Raton, 1997).
4. J. S. Lee, Comput. Vis. Graph. Image Process **24**, 255 (1983).
5. V. I. Ponomarev and O. B. Pogrebnyak, J. Electron. Imaging **8**, 467 (1999).
6. V. F. Kravchenko, V. I. Pustovoit, V. I. Ponomarev, and A. B. Pogrebnyak, Dokl. Akad. Nauk **371**, 611 (2000) [Dokl. Phys. **45**, 149 (2000)].
7. V. F. Kravchenko, V. I. Ponomarev, A. B. Pogrebnyak, *et al.*, Radiotekh. & Elektron. (Moscow) **46** (4) (2001) (in press).
8. F. J. Gallegos-Funes, V. I. Ponomarev, V. F. Kravchenko, and L. Nino-de-Rivera, Telecommun. Radio Eng. (Engl. Transl.) **56** (1), 71 (2001).
9. V. F. Kravchenko, V. I. Ponomarev, V. I. Pustovoit, and L. Nino-de-Rivera, Dokl. Akad. Nauk **376**, 629 (2001) [Dokl. Phys. **46**, 97 (2001)].
10. F. J. Gallegos-Funes, V. I. Ponomarev, A. B. Pogrebnyak, and L. Nino-de-Rivera, in *Proceedings of the International Workshop on Mathematical Modeling of Physical Processes in Inhomogeneous Media, Guanajuato, 2001*, p. 38.

Translated by V. Tsarev

Doklady Physics, Vol. 46, No. 9, 2001, pp. 647–650. Translated from Doklady Akademii Nauk, Vol. 380, No. 3, 2001, pp. 338–341.

TECHNICAL PHYSICS

The Synthesis of Signal-Correcting Systems for Antennas of Ultrashort Pulses

Corresponding Member of the RAS L. D. Bakhrakh* and M. Ya. Izrailovich**

Received March 2, 2001

When ultrashort pulses are emitted by antennas [1, 2], the emitted signal differs substantially from that fed to the antenna input from a generator because of dynamic distortions. The actual emitted signal is essentially different from the desired one both in form and duration. For the distortion level to be reduced, it was proposed in [3] to feed an additional correcting signal into the antenna input in addition to the major (operating) pulse.

Supplying a correcting signal simultaneously while applying a linear correcting transformation to the major operating signal is a more efficient means for reducing the distortion level. A general method of constructing such correcting systems is presented in this paper.

1. STATEMENT AND SOLUTION OF THE PROBLEM

According to the block diagram of the correcting system presented in the figure, a signal $x_0(t)$ produced by an ultrashort-pulse generator is fed into the input of a correcting device, whose dynamics is described by an impulse transient function $v(t-\tau)$. Next, the transformed signal is added to the correcting signal $u(t)$. Thereafter, it is fed into the antenna input, whose dynamics is characterized by an impulse transient function $h(t-\tau)$.

As a result, a time diagram of the emitted unidirectional signal is determined in the form

$$y = \int_0^t h(t-\tau)\int_0^\tau v(\tau-\theta)x_0(\theta)d\theta d\tau + \int_0^t h(t-\tau)u(\tau)d\tau \qquad (1)$$

$$= \int_0^t g(t-\tau)v(\tau)d\tau + \int_0^t h(t-\tau)u(\tau)d\tau,$$

where

$$g(t-\tau) = \int_\tau^t h(t-\theta)x_0(\theta-\tau)d\theta.$$

Let $y_*(t)$ be the desired emitted-signal time diagram, which is assumed to be a finite function

$$y_*(t) \neq 0, \quad t \in (0, T_1), \quad y_*(t) = 0, \quad t \in [T_1, \infty).$$

It is necessary to find functions $v_*(t)$, $u_*(t)$ providing the best fit of $y(t)$ to $y_*(t)$. As a criterion of such closeness, with the physical feasibility requirement taken into account, the following quadratic functional is used:

$$J(v, u) = \int_0^T [(y-y_*)^2 + \gamma_1 u^2 + \gamma_2 v^2]dt. \qquad (2)$$

Here, $T > T_1$ and γ_1, γ_2 are positive weighting coefficients.

Assuming that the functions v, u belong to the space $L^2(0, T)$, we can write out diagram (1) in the form $y = Au + Bv$, where A and B are bounded linear operators;

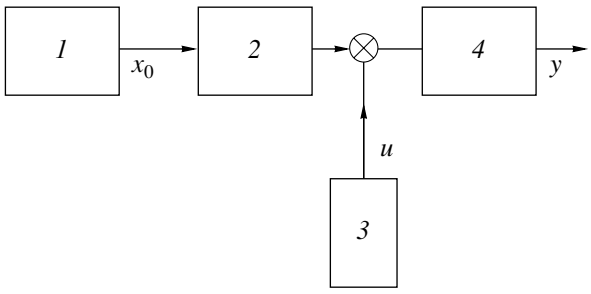

Block diagram of the system: (*1*) operating-pulse generator; (*2*) linear correcting device; (*3*) correcting-pulse generator; (*4*) antenna.

* *Moscow Research Institute of Instrument Building, Kutuzovskiĭ pr. 34, Moscow, 121170 Russia*

** *Institute of Mechanical Engineering, Russian Academy of Sciences, ul. Bardina 4, Moscow, 117334 Russia*

1028-3358/01/4609-0647$21.00 © 2001 MAIK “Nauka/Interperiodica”

functional (2) can be represented in the form

$$J(v, u) = (y - y_*, y - y_*) + \gamma_1(u, u) + \gamma_2(v, v)$$
$$= (Au + Bv - y_*, Au + Bv - y_*) + \gamma_1(u, u) + \gamma_2(v, v). \quad (3)$$

A procedure similar to that outlined in [4] for the case of a desired function is used for minimization of functional (3). The following system of linear operator equations is obtained as a result of employing this procedure:

$$A^*Au + A^*Bv + \gamma_1 u = A^*y_*,$$
$$B^*Au + B^*Bv + \gamma_2 v = B^*y_*. \quad (4)$$

Here, A^*, B^* are operators conjugate to the operators A, B. It follows from (4):

$$u_* = (r_{11}A^* + r_{12}B^*)y_*,$$
$$v_* = (r_{21}A^* + r_{22}B^*)y_*,$$

where r_{sk} ($s = 1, 2$, $k = 1, 2$) are elements of a matrix operator $R_{\gamma_1\gamma_2}$, which is the inverse of the matrix operator of the left-hand side of system (4).

In the nonabstract form, system (4) takes a form of Volterra linear integral equations of the second kind:

$$\int_t^T h(s-t)\int_0^s h(s-\tau)u(\tau)d\tau ds + \int_t^T h(s-t)\int_0^s g(s-\tau)v(\tau)d\tau ds + \gamma_1 u = \int_t^T h(s-t)y_*(s)ds,$$
$$\int_t^T g(s-t)\int_0^s h(s-\tau)u(\tau)d\tau ds + \int_t^T g(s-t)\int_0^s g(s-\tau)v(\tau)d\tau ds + \gamma_2 v = \int_t^T g(s-t)y_*(s)ds. \quad (5)$$

By virtue of this, r_{sk} are elements of the matrix resolvent $R_{\gamma_1\gamma_2}$. It follows from (5): $u(T) = v(T) = 0$. By applying the operators A^{*-1} and B^{*-1} (which are the inverses of the operators A^*, B^*) to the first and second equations of the system, respectively, we obtain

$$\gamma_1 A^{*-1}u(0) = y_*(0) = 0,$$
$$\gamma_2 B^{*-1}v(0) = y_*(0) = 0.$$

2. A PROBLEM WITH FIXED FINAL CONDITIONS

Although the procedure outlined provides a reduction in the emission intensity outside the desired time interval $(0; T_1)$, it does not allow the emission to be completely suppressed at the fixed instant upon the completion of the observational period $t = T$. When this condition is rigorously required, laws $u(t)$ and $v(t)$ must be determined such that the equalities $y^i(T) = 0$, $i = 0, 1, \ldots, n-1$ are provided, where $y^i(T)$ is the derivative of the ith order of the emitted signal $y(t)$ at the instant of time $t = T$. In view of (1), these conditions are written in the form:

$$y^i(T) = A_i(T)u + B_i(T)v = 0. \quad (6)$$

Here,

$$A_i(T)u = \int_0^T h^i(T-t)u(t)dt,$$
$$B_i(T)v = \int_0^T g^i(T-t)v(t)dt;$$

and the superscript implies the derivative of the ith order.

For linear isoperimetric conditions (6) to be met, the following extended functional should be introduced when minimizing functional (3):

$$\tilde{J}(u, v, \lambda) = J(u, v) + \sum_{i=0}^{n-1} \lambda_i [A_i(T)u + B_i(T)v]. \quad (7)$$

Here, λ_i ($i = 0, 1, \ldots, n-1$) are Lagrange factors.

As a result of the minimization of functional (7), the following system of equations is obtained for the functions u, v instead of Eqs. (4):

$$A^*Au + A^*Bv + \gamma_1 u = A^*y_* - \sum_{i=0}^{n-1} \lambda_i h^i(T-t),$$
$$B^*Au + B^*Bv + \gamma_2 v = B^*y_* - \sum_{i=0}^{n-1} \lambda_i g^i(T-t). \quad (8)$$

On account of system (8), the functions u, v must obey the boundary conditions

$$\gamma_1 u(T) = -\sum_{i=0}^{n-1} \lambda_i h^i(0), \quad \gamma_2 v(T) = -\sum_{i=0}^{n-1} \lambda_i g^i(0),$$

$$\gamma_1 A^{*-1} u(0) = -\sum_{i=0}^{n-1} \lambda_i h^i(T),$$

$$\gamma_2 B^{*-1} v(0) = -\sum_{i=0}^{n-1} \lambda_i g^i(T).$$

As a result of the substitution of the solution to system (8), $u(\lambda_i)$, $v(\lambda_i)$ into isoperimetric conditions (6), we obtain a system of n linear algebraic equations in Lagrange factors λ_i. After solving this system, the final expressions for u_*, v_* are determined:

$$u_* = (r_{11}A^* + r_{12}B^*)y_* - \sum_{i=0}^{n-1}\sum_{j=0}^{n-1} \frac{\Delta_{ij}}{\Delta} h^i(T-t)$$
$$\times \{[A_j(T)r_{11} + B_j(T)r_{21}]A^* + [A_j(T)r_{12} + B_j(T)r_{22}]B^*\}y_*, \quad (9)$$

$$v_* = (r_{21}A^* + r_{22}B^*)y_* - \sum_{i=0}^{n-1}\sum_{j=0}^{n-1} \frac{\Delta_{ij}}{\Delta} g^i(T-t)$$
$$\times \{[A_j(T)r_{11} + B_j(T)r_{21}]A^* + [A_j(T)r_{12} + B_j(T)r_{22}]B^*\}, \quad (10)$$

In (9), (10), Δ implies a determinant of the matrix

$$\left\| A_j(T)(r_{11}A^* + r_{12}B^*)h^i(T-t) + B_j(T)(r_{21}A^* + r_{22}B^*)g^i(T-t) \right\|,$$
$$j = 0, 1, \ldots, n-1, \quad i = 0, 1, \ldots, n-1,$$

and Δ_{ij} are its algebraic adjuncts. As before, $A_i(T)f$, $B_i(T)f$ denote linear operators

$$\int_0^T h^i(T-t) f(t) dt, \quad \int_0^T g^i(T-t) f(t) dt.$$

3. SCHEMES OF A SIMPLIFIED SOLUTION

Although the numerical constructing of the functions $v_*(t)$, $u_*(t)$ is in accordance with the procedures described, nevertheless, the procedure is fairly cumbersome. This is also true when numerical methods are combined with approximate analytical methods; in particular, when those used for the construction of the matrix are resolvent $R_{\gamma_1\gamma_2}$ in the series form. At the same time, for preliminary (estimating) calculations simpler algorithms and procedures that are based as much as possible on closed analytic representations for solutions are preferred. Because of this some versions of simplified schemes of the solution are presented below.

1. At first, the problem of finding $v_*(t)$ is solved. In this case,

$$y = Bv, \quad J = (y - y_*, y - y_*) + \gamma_2(v, v). \quad (11)$$

The solution is determined as $v_* = R_{\gamma_2} B^* y_*$, where, in this case, R_{γ_2} is a scalar operator, which is the inverse of the operator $B^*B + \gamma_2$. Then, we assume that $y_0 = Bv_*$. After that, the problem of finding u_* is solved by minimizing the functional

$$J(u) = (Au + y_0 - y_*, Au + y_0 - y_*) + \gamma_1(u, u). \quad (12)$$

As a result, u_* is determined in the form $u_* = R_{\gamma_1}(y_* - y_0)$, where R_{γ_1} is a scalar operator that is the inverse of the operator $A^*A + \gamma_1$.

2. Use of simplified schemes is especially topical for a problem with fixed final conditions, since the realization of $u_*(t)$, $v_*(t)$ in the form (9), (10) is quite cumbersome. In this case, we first determine v_* by minimizing functional $J(v)$ (11) without taking into account conditions (6). For the complete antenna damping, only the additive correcting signal $u_*(t)$ is employed. In so doing, an extended functional corresponding to $J(u)$ (12) is minimized in which Lagrange factors are inserted. As a result, u_* is determined in the form:

$$u_* = R_{\gamma_1}\left\{A^*(y_* - y_0) - \sum_{j=0}^{n-1}\sum_{i=0}^{n-1} \frac{\Delta_{ij}}{\Delta} h^i(T-t) \times A_j(T)[R_{\gamma_1}A^*(y_* - y_0) + v_* x_0]\right\}. \quad (13)$$

Here, Δ is the determinant of the matrix

$$\left\| A_j(T) R_{\gamma_1} h^i(T-t) \right\|,$$
$$i = 0, 1, \ldots, n-1, \quad j = 0, 1, \ldots, n-1,$$

and Δ_{ij} are its algebraic adjuncts;

$$v_* x_0 = \int_0^t v_*(t-\tau) x_0(\tau) d\tau.$$

3. In the case of a problem with a fixed right-hand end, only the correcting device v_* is used for correcting the signal form. The function v_* is determined in the

same way as above. As for the additive signal u_*, it is used only for complete antenna damping. In this case, the integral quadratic value $J(u) = (u, u)$ serves as the minimized functional. The solution is reduced to the standard procedure [5] and is determined as

$$u_* = -\sum_{j=0}^{n-1}\sum_{i=0}^{n-1}\frac{\Delta_{ij}}{\Delta}h^i(T-t)B_j(T)v_*, \qquad (14)$$

where Δ and Δ_{ij} correspond to the previously obtained solution (13) for $R_{\gamma_1} = 1$. It is much easier to construct u_* (14) than u_* (13).

REFERENCES

1. H. F. Harmuth, *Nonsinusoidal Waves for Radar and Radio Communication* (Academic, New York, 1981; Radio i Svyaz', Moscow, 1985).
2. L. D. Bakhrakh and A. A. Bliskovitskiĭ, Usp. Fiz. Nauk **162** (12), 51 (1992).
3. L. D. Bakhrakh and M. Ya. Izrailovich, Antenny, No. 2 (48), 58 (2001).
4. R. E. Bellman, I. Glicksberg, and O. A. Gross, *Some Aspects of the Mathematical Theory of Control Processes* (Rand Corp., Santa Monica, 1958; Inostrannaya Literatura, Moscow, 1962).
5. N. N. Krasovskiĭ, *Theory of Motion Control. Linear Systems* (Nauka, Moscow, 1968).

Translated by V. Tsarev

Doklady Physics, Vol. 46, No. 9, 2001, pp. 651–653. Translated from Doklady Akademii Nauk, Vol. 380, No. 3, 2001, pp. 342–345.

TECHNICAL PHYSICS

Formation of a Two-Phase Zone in the Course of Rapid Solidification of Refractory Oxides

A. Yu. Vorobyev, V. A. Petrov, V. E. Titov, and Academician V. E. Fortov

Received February 20, 2001

Among the refractory semitransparent aluminum, zirconium, magnesium, and yttrium oxides and some other oxides, there are those in which solid–liquid and inverse transitions occur. For many years, a classic model was employed for the description of these transitions both for the materials mentioned above and for opaque materials. This model considered only two layers, solid and liquid, separated by a smooth boundary, for which the Stefan conditions were written. Early in the 1960s, most likely for the first time, mathematicians pointed out the shortcomings of such a model even for applications to opaque materials. As a result, a theory for a generalized solution to the Stefan problem was developed, in which the existence of an extended quasiequilibrium two-phase zone was assumed [1, 2]. Various reasons for the cause of the formation of the two-phase zone were considered, but the role of volumetric radiative heat transfer inside a crystallizing semitransparent material had not yet been analyzed. In paper [3], a model of melting and solidification was first considered that allowed for the possibility of forming an extended two-phase zone caused by the radiative heat transfer. In this case, only three simplified problems for model materials were analyzed. In particular, the absorption coefficients in solid and liquid phases were thought to be independent of both the wavelength and temperature. Thermal properties were also assumed to be constant and similar for both phases. Nonequilibrium effects, such as supercooling, were disregarded, and the nature of the formation of crystallization centers was not considered at all. It is clear that the formation of a two-phase zone is possible if volumetric sources and heat outflow exist so that nuclei of a new phase can appear in bulk. However, the question of the experimental or numerical–theoretical study of the possibility of a two-phase zone formation in the course of fusion or solidification of refractory oxides has not been considered until the present time.

In [4], we suggested a more realistic mathematical formulation of the Stefan problem as applied to semitransparent materials. In addition to the one-dimensional non-steady-state process of combined radiative-conductive heat transfer accompanied by the possible formation of a two-phase zone, the model allowed for possible overheating and supercooling, arbitrary nonlinear boundary conditions at the front and back surfaces of a sample, and the dependence of thermal and thermal–radiative properties of both the phases on temperature and on temperature and wavelength, respectively. This model was used for the numerical calculation of the temperature distribution in a flat aluminum oxide sample while it was being heated by concentrated laser or solar radiation and, subsequently while it was cooling after switching off the radiation. Aluminum oxide is a unique oxide for which data on the optical and thermal properties of the melt are available. Some calculation results for the one-dimensional field in a flat 10-mm-thick sample of Al_2O_3 are presented in Fig. 1; the sample was heated from one of its sides by a CO_2-laser radiation with a flux density of 600 W cm^{-2}. Only the region of 2-mm thick near the heated surface is shown; the heating stage is not shown. The first temperature profile in Fig. 1 relates to the time moment of 100 s after the beginning of the heating, when the laser heating was switched off. At this moment, the temperature profile is close to a quasistationary one, and the thickness of the molten layer is equal to 0.625 mm. In accordance with the calculations, the two-phase zone is not observed either in the process of melting the sample and increasing the molten layer thickness or on attaining the quasistationary state. After switching off the laser heating, the surface temperature rapidly drops and after 130 ms becomes less than the melting temperature, although a liquid state is retained. The minimum surface temperature is about 50 K lower than the melting temperature. The two-phase zone appears near the surface about 0.2 s after the beginning of the cooling. Its thickness increases very rapidly: within the range from 100.3 to 100.5 s, it increases from 180 to 340 μm. At 100.7 s, the two-phase zone occupies almost a whole layer, which became molten before the beginning of the cooling. One should note that at 100.5 s, a thin layer of the solid phase appears near the surface but because of its high transparency it slightly affects the heat transfer in the sample; its temperature is close to the solidification point. The process of complete solidification of the two-phase zone is rather long: it takes about 0.5 s. It is

Institute for High Energy Densities, Associated Institute for High Temperatures, Russian Academy of Sciences, Izhorskaya ul. 13/19, Moscow, 127412 Russia

1028-3358/01/4609-0651$21.00

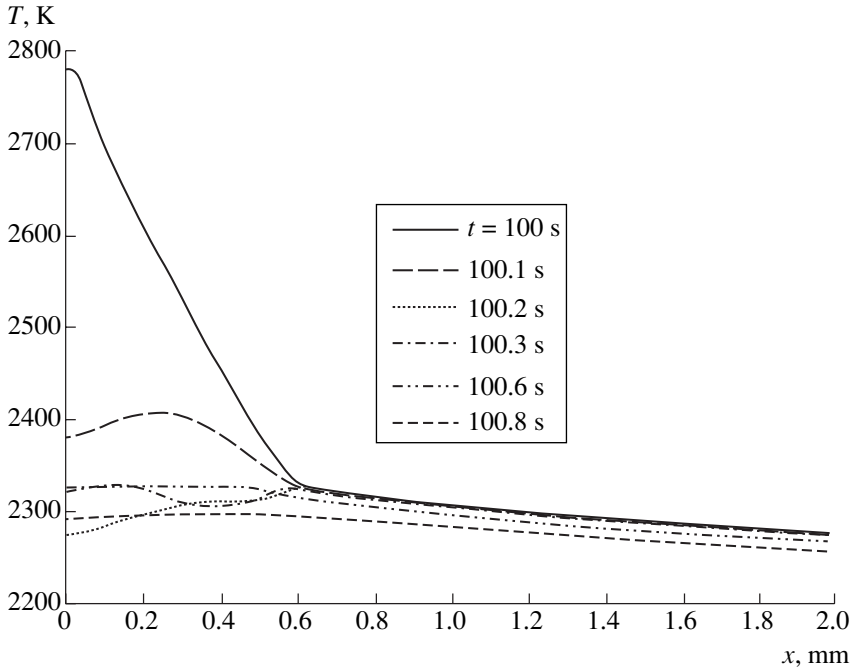

Fig. 1. Temperature distribution observed in the aluminum oxide in the process of cooling.

this process that was observed in experiments of some authors on the solidification of molten oxides in solar and arc image furnaces as a region with a constant brightness temperature and treated as a solidification plateau.

Similar calculations were performed in the case of heating using concentrated solar radiation with the same flux density of 600 W cm^{-2}. The quasistationary temperature distribution slightly differed from that attained under laser heating, but this fact weakly influenced the solidification process.

However, our mathematical model does not allow for scattering, which can exist in a solidified layer because of its porosity and in the two-phase zone because of a difference in the refractive indices of liquid and solid phases. Therefore, special experiments on solidification were carried out under conditions of rapid cooling. One of the experiments involved the study of the solidification process when measuring thermal-radiative characteristics of ceramics made of aluminum oxide with a molten pool at its surface, which was formed by laser heating. The high-speed measurements of reflection of the probing laser radiation with the required wavelength from the specimen were carried out in the processes of sample heating by CW CO_2-laser and subsequent cooling after switching off the laser heating. When heating with a flux density about 1600 W cm^{-2}, the thickness of the molten layer was about 0.4 mm. The solidification plateau in the temperature measurements for the wavelengths of 0.55 and 0.72 μm was not flat: after supercooling, a small segment of the plateau with a slight slope was observed on the thermogram. Its length was about 0.17 s.

In other experiments, a sample of premelted powder of pure aluminum oxide that had been solidified in the surrounding of the same powder was heated by concentrated laser radiation with a flux density of about 1000 W cm^{-2} in an air atmosphere during a longer period of time, about 2–3 minutes. In the steady state, the thickness of the melt was about 2–3 mm. The results of the measurement of brightness temperatures for a series of wavelengths are shown in Fig. 2; they were obtained in the course of the cooling process after switching off the laser heating. Since some differences were observed in the density of the radiation flux in these experiments, the regions of heating are not presented in Fig. 2. The beginning of the cooling is normalized to the same time moment.

As follows from Fig. 2, the horizontal solidification plateau for the brightness temperatures was observed at wavelengths of 0.55, 5.0, and 9.0 μm. Its length was significantly greater than that for a thin melt and amounted to about 2 s. Contrary to the results of numerical calculations, there were no horizontal regions for the brightness temperatures on the cooling thermograms for the wavelengths of 2 and 3 μm (corresponding to the lowest values of the absorption coefficient); these regions were slightly inclined. A steep fall of the brightness temperatures after finishing the solidification, which followed from the results of the numerical modeling, was not found. The microstructure analysis of the cross section of the solidified melts showed that when a total thickness of the solidified layer was about 0.4 mm, the solidified melt contained a combination of lath crystals with a trigonal orientation, with the laths consisting of elementary cubic crystals. There were

voids in the space between the laths. In this case, a homogeneous nucleation was most probable. Because of the small thickness of the sample, the whole molten layer was intensely cooled as a result of volumetric radiation, and the cooling rate was much higher than that in the experiments with a thick molten layer. The supercooling causes volumetric nucleation and the growth of randomly oriented grains. The microstructure of the solidified thick layer of the melt was slightly different. The subsurface layer with a thickness of about 450 μm consisted of two sublayers. The upper sublayer, with a thickness of about 250 μm, had a dendritic structure (the dendrite axes were perpendicular to the surface); the lower one consisted of more isometric particles. Beyond the subsurface layer, there was a zone of large columnar crystals misaligned to a greater or lesser extent with the normal to the sample surface. Voids and fissures were seen in both the sublayers, and they also could have caused scattering. The scattering coefficient in the two-phase zone and in the crystallized layer certainly depended on the wavelength. The formation of voids and fissures was associated with a large increase (approximately by 30%) in the density of Al_2O_3 during solidification. Though the structure of the thicker crystallized layer of the melt differs from that of a thinner one, the two-phase zone formation is also very probable in the process of crystallization. The dendritic nature of the crystal growth in the subsurface layer suggests that dendrites grew from the surface into the supercooled melt and expanded into the melt between individual dendrites. The transition from dendritic growth to the growth of roughly isometric grains is associated with the decrease of the cooling rate in deeper layers of the melt.

To confirm the possibility of forming a two-phase zone in the process of rapid solidification of other refractory oxides, we carried out experiments with cubic zirconium oxide stabilized by 18 mol % of calcium oxide. These experiments were performed in a vacuum and in air. One of the principal differences in the results obtained was that supercooling was observed in the vacuum and not in air. With respect to the experiments in the vacuum, the molten layer and the adjacent ceramic layer became black because of oxygen loss. After the experiments, the reflectivity of the sample at room temperature remained very low within the studied spectral range from 0.63 to 3.39 μm. This implies that the absorption coefficient increased irreversibly during the process of heating in the vacuum and the material became practically opaque. The color of the ceramics and the solidified melt did not change during the experiments in air. In the course of heating, the absorption coefficient certainly increased; however, even at the highest temperature of 3400 K, the oxide melt in air should be considered a semitransparent substance. Actually, the micrographs of the structure showed that the solidification of a 70-μm-thick layer adjacent to the surface involved the formation of individual star-like dendritic crystals with sizes from 10 to 50 μm. They had no predominant orientation and had voids between them.

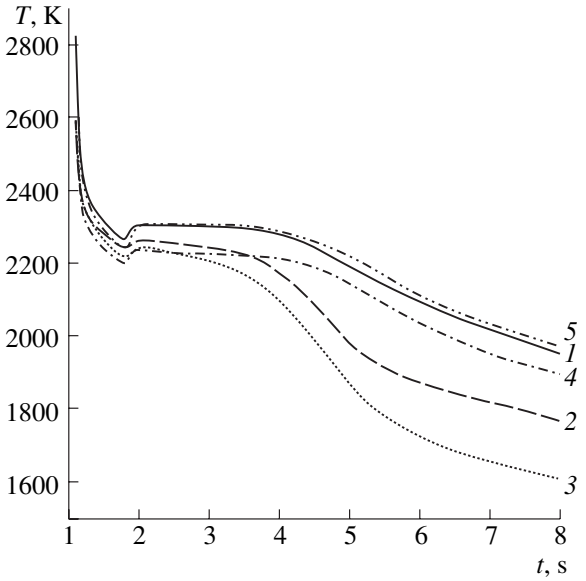

Fig. 2. Brightness temperatures of the deep pool with the melt of aluminum oxide observed in the process of its cooling for various wavelengths: (*1*) 0.55; (*2*) 2; (*3*) 3; (*4*) 5; (*5*) 9 μm.

This suggests that this layer crystallizes by volumetric nucleation and that a two-phase zone exists. Owing to the high values of the absorption coefficient on heating in a vacuum, the solidification began at the surface where the supercooling was greatest. The grains grew inside, the outer layer adjacent to the surface and observed in the process of solidification in air was absent, and the two-phase zone was absent, too.

Thus, the results of our experiments and numerical calculations showed that the temperature plateau observed in the process of solidification is explained by the existence of a two-phase zone. However, such a two-phase zone is not always formed. Its formation depends on the value of the absorption coefficient of the melt, the cooling rate, and the solidification point determining the contribution of the volumetric radiative heat transfer.

ACKNOWLEDGMENTS

This work was supported by the Russian Foundation for Basic Research, project no. 98-02-16115.

REFERENCES

1. N. A. Avdonin, *Mathematical Description of Crystallization Processes* (Zinatne, Riga, 1980).
2. A. M. Meĭrmanov, *Stefan Problem* (Nauka, Novosibirsk, 1986).
3. S. H. Chan, D. H. Cho, and G. Kocamustafaogullary, Int. J. Heat Mass Transf. **26**, 621 (1983).
4. V. A. Petrov, V. E. Titov, and A. Yu. Vorobyev, High Temp.–High Press. **31**, 267 (1999).

Translated by T. Galkina

Doklady Physics, Vol. 46, No. 9, 2001, pp. 654–658. Translated from Doklady Akademii Nauk, Vol. 380, No. 1, 2001, pp. 38–42.

MECHANICS

Schemes of the Krylov–Bogolyubov Averaging Method for the Highest Powers

L. D. Akulenko

Presented by Academician V.V. Kozlov April 9, 2001

Received April 10, 2001

The modified averaging method is presented for investigating nonlinear vibrations described by the N.N. Bogolyubov standard system. The following situation encountered in applied problems is considered: the first-approximation set makes it impossible to judge its substantial evolution and qualitative behavior (an averaged value of the right-hand side of the system is identically equal to zero). The procedure for constructing the averaged system is developed and substantiated to describe the evolution for much longer time intervals, and this system is averaged over the negative powers (quadratic, cubic, etc.) of a small parameter. The efficiency of the proposed schemes of averaging the highest powers is illustrated by solving some examples.

1. We consider a multi-dimensional nonlinear vibratory system in the standard Bogolyubov form [1–4]:

$$\dot{x} = \varepsilon X(t, x), \quad t \geq 0, \quad x(0) = x^0, \quad 0 \leq \varepsilon \leq \varepsilon_0 \ll 1. \tag{1}$$

Here, x is the n-vector, $x \in D \subset R^n$, D is a certain bound set (a closed [1–3] or open [4] region); X is the smooth function of a real variable x, whose properties of smoothness are specified below; and the continuity and 2π-periodicity are assumed with respect to the argument t (t is the time or phase).

To investigate the Cauchy problem (1), we carry out standard constructions of the averaging method [1–4] and write out the averaged first-approximation system:

$$\dot{\xi} = \varepsilon X_0(\xi), \quad \xi(0) = x^0, \quad X_0(\xi) \equiv \langle X(t, \xi) \rangle, \quad 0 \leq t \leq \frac{L}{\varepsilon}. \tag{2}$$

According to the character of the first-approximation solution ξ [given by (2)] and the local properties of system (1) in the vicinity of this solution, we use the results of the Bogolyubov principal theorems on the proximity of solutions (ε-proximity in the case of the periodicity in t) for the asymptotically large time interval $0 \leq t \leq \frac{L}{\varepsilon}$ (the first theorem, the averaging method [1–6]), or the averaging on the infinite interval $|t| < \infty$ (the second theorem, the method of local integral manifolds [1–3]). If $X_0(\xi) \not\equiv 0$, the solution $\xi = \xi_0$ (2), generally speaking, gives a reasonably complete representation of the evolution of osculating variables x and the process in general. Their variations (on the order of unity) can be substantial for $t \sim \frac{1}{\varepsilon}$. Successive approximations give only a small refinement [on the order $O(\varepsilon)$] of the solution at the interval $0 \leq t \leq \frac{L}{\varepsilon}$.

We consider the situation when the higher approximations are fundamentally important. In applied problems, the identity $X_0(\xi) \equiv 0$ often takes place; in this case, $\xi_0 \equiv x^0$, and, at the interval $t \sim \frac{1}{\varepsilon}$, the variable x executes small vibrations with an amplitude on the order $O(\varepsilon)$ relative to $x = x^0$. We propose the approach associated with constructing the schemes of averaging the highest powers of ε with a considerable increase in the interval of variation of the argument t. We use the standard transformation of the variable $x \longrightarrow \xi$ [1–6]:

$$x = \xi + \varepsilon u(t, \xi), \quad u \equiv \int_0^t X(s, \xi) ds, \quad X_0(\xi) \equiv 0. \tag{3}$$

The function u in (3) is 2π-periodic in t at fixed ξ; the quantity ξ is the new unknown variable to be determined from the Cauchy problem:

$$\dot{\xi} = \varepsilon^2 \Xi(t, \xi, \varepsilon), \quad \xi(0) = x^0 \quad \left(\frac{\partial u}{\partial t} \equiv X(t, \xi)\right), \tag{4}$$

$$\Xi \equiv (I + \varepsilon u'_\xi)^{-1} \varepsilon^{-1} [X(t, \xi + \varepsilon u) - X(t, \xi)], \quad \xi \in D.$$

For reasonably small values of $\varepsilon > 0$, the right-hand side of system (4) is smooth with respect to ξ, $\xi \in D$,

Institute of Problems of Mechanics,
Russian Academy of Sciences,
pr. Vernadskogo 101, Moscow, 117526 Russia

1028-3358/01/4609-0654$21.00

and is 2π-periodic in time. For the function Ξ, the approximated representation is valid:

$$\Xi = \Xi_{(0)}(t, \xi) + \varepsilon\Xi_1(t, \xi) + \varepsilon^2 + \ldots \equiv \Xi_{(0)} + \varepsilon\Delta\Xi,$$
$$\Xi_{(0)} = X'_\xi u, \quad \Xi_1 = \frac{1}{2}(X''_{\xi^2}u, u) - u'_\xi X'_\xi u, \ldots . \tag{5}$$

Next, the Cauchy problem (4), (5) is considered at the interval $0 \le t \le \frac{L}{\varepsilon^2}$, where the variable ξ (and x) can substantially change by a value of the order of unity. It is necessary to construct the scheme of the averaging method for higher-order powers of ε and to substantiate the estimate of proximity. The principal purpose of the outlined asymptotic approach, as with the Krylov–Bogolyubov classic method [1], is to evade the secular terms in the approximate construction of the solution at the interval $0 \le t \le \frac{L}{\varepsilon^2}$. The development of such an approach in the calculation aspect is also thought to be topical, because the numerical integration of the Cauchy problems (1), (4), at $t \sim \frac{1}{\varepsilon^2}$ is still more problematic than at $t \sim \frac{1}{\varepsilon}$.

2. We apply to the Cauchy problem (4), (5) the standard scheme of change of variables $\xi \longrightarrow \eta$ of type (3):

$$\xi = \eta + \varepsilon^2 v(t, \eta, \varepsilon) = \eta + \varepsilon^2 v_2 + \varepsilon^3 v_3 + \varepsilon^4 + \ldots,$$
$$v \equiv \int_0^t (\Xi(s, \eta, \varepsilon) - \langle\Xi\rangle)ds, \quad \eta \in D, \tag{6}$$
$$\dot\eta = \varepsilon^2\Xi_0(\eta) + \varepsilon^3\Xi_{10}(\eta) + \varepsilon^4 H(t, \eta, \varepsilon), \quad \eta(0) = x^0,$$
$$\Xi_0 = \langle\Xi_0(t, \eta)\rangle, \quad \Xi_{10} = \langle\Xi_1(t, \eta)\rangle, \ldots, \quad 0 \le t \le \frac{L}{\varepsilon^2}.$$

The function H is known, 2π-periodic in t, smooth, and uniformly restricted in η, $\eta \in D$, for reasonably small values $\varepsilon > 0$; its definition is similar to (4) for Ξ. Let $\Xi_0 \not\equiv 0$; in this case, it is natural to introduce an argument interval $0 \le t \le \frac{L}{\varepsilon^2}$, at which the variable η, together with the variables ξ and x, change by a substantial value on the order of unity. We reject the terms $O(\varepsilon^3)$ and higher order on the right-hand side of system (6) and obtain the first-approximation self-governing system, whose solution is considered as known:

$$\dot\eta_0 = \varepsilon^2\Xi_0(\eta_0), \quad \eta_0(0) = x^0,$$
$$\eta_0 = \eta_0(\varepsilon^2 t, x^0), \quad 0 \le \varepsilon^2 t \le L. \tag{7}$$

The uniform proximity of solutions η and η_0 to problems (6) and (7) is estimated by means of integral inequalities (Gronuolla lemma [1–4]). The standard procedure for constructing the estimates in the averaging method leads to the uniform estimate

$$\max_t|\eta - \eta_0| \le C_\eta\varepsilon, \quad 0 \le t \le \frac{L}{\varepsilon^2};$$
$$C_\eta \text{ and } L \text{ are the constants,} \tag{8}$$
$$C_\eta = ML\exp(\lambda L), \quad M = \max_{t,\eta}|\Xi_{10} + \varepsilon H|,$$
$$\eta \in D, \quad 0 \le \varepsilon \le \varepsilon_0.$$

Here, λ is the Lipschitz constant in η for the function $\Xi_0(\eta)$. It is assumed [1–3] that $\eta_0 \in D$ is with a certain small neighborhood. From (8), it follows, making allowance for (6) and (3), that the solution η_0 to (7) is ε-proximate to the solutions ξ and x, to problems (4) and (1), respectively:

$$\max_t|\xi - \eta_0| \le C_\xi\varepsilon, \quad \max_t|x - \eta_0| \le C_x\varepsilon,$$
$$0 \le t \le \frac{L}{\varepsilon^2}. \tag{9}$$

Thus, for $X_0 \equiv 0$ and $\Xi_0 \not\equiv 0$, the first-approximation solution η_0 (7) determines the evolution of the system (1) at the interval $t \sim \frac{1}{\varepsilon^2}$ with a small error $O(\varepsilon)$. The procedure of refining the solution η of problem (6) with respect to the powers of ε is realized similarly to the averaging method [1–6]. The required degree of accuracy is restricted by the smoothness of the function Ξ, i.e., of the initial right-hand side of X (1). In particular, if the function $\Xi_{(0)}$ satisfies the Lipschitz condition with respect to ξ, $\xi \in D$, with a uniformly bounded constant λ, while the function $\Delta\Xi$ is uniformly bounded in the region $0 \le \varepsilon \le \varepsilon_0$, $\eta \in D$, $t \ge 0$, then the estimates of ε-proximity (8) and (9) take place for the first-approximation solution η_0 (7). The function $\Xi_{(0)}$ is such if the initial function X is continuously differentiable with respect to x, $x \in D$, while the derivatives satisfy the Lipschitz condition. The scheme of higher order powers of ε requires higher smoothness than the standard averaging scheme. Conceptually, this scheme is related to constructing the second approximation (see Section 3).

If the function $\Xi_{(1)} = \Xi_{(0)} + \varepsilon\Xi_1$ (5) satisfies the Lipschitz condition with respect to ξ, i.e., the second derivatives of the function X meet this condition with respect to x, $x \in D$, the following second-approximation scheme can be written out according to (6):

$$\dot\eta_{(1)} = \varepsilon^2\Xi(\eta_{(1)}) + \varepsilon^3\Xi_{10}(\eta_{(1)}), \quad \eta_{(1)}(0) = x^0;$$
$$\eta_{(1)} = \eta_0(\varepsilon^2 t, x^0) + \varepsilon\eta_1(\varepsilon^2 t, x^0) + \varepsilon^2 + \ldots, \ 0 \le \varepsilon^2 t \le L. \tag{10}$$

The function η_1 in (10) can easily be found by numerical or analytical methods using the generating solution η_0 (7) and the system in variations. In this case, it is convenient to introduce the slow argument $\tau = \varepsilon^2 t$, $0 \le \tau \le L$. Without any loss of accuracy with respect to

the powers of ε, we can substitute $\eta_0(\tau, x^0)$ into the function Ξ_{10}. Using the acquired solution $\eta_{(1)}(\tau, x^0, \varepsilon)$ to (10), we obtain the estimates:

$$\max_t|\eta - \eta_{(1)}| \le C_\eta\varepsilon^2, \quad \max_t|\xi - \eta_{(1)}| \le C_\xi\varepsilon^2,$$
$$\max_t|x - [\eta_{(1)} + \varepsilon u(t, \eta_0]| \le C_x\varepsilon^2, \quad 0 \le t \le \frac{L}{\varepsilon^2}. \tag{11}$$

The construction of more exact solutions $\eta_{(k)}(t, x^0, \varepsilon)$, $k \ge 3$, which differ from η by $O(\varepsilon^k)$ for $0 \le t \le \frac{L}{\varepsilon^2}$, requires a higher smoothness of the function X and rather cumbersome expansions, taking into account the expression for $H(t, \eta, \varepsilon)$ in (6), which require invoking computer-algebra methods.

Theorem 1. *When the condition $X_0(x) \equiv 0$ in* (2) *and the formulated conditions of smoothness in x and periodicity in t for the function $X(t, x)$ are met, the solution $x(t, x^0, \varepsilon)$ of system* (1) *is represented by the function $\eta_0(\varepsilon^2 t, x^0)$* (7) *at the interval $0 \le t \le \frac{L}{\varepsilon^2}$ with an error $O(\varepsilon)$ according to* (9) *and by the function $\eta_{(1)} + \varepsilon u(t, \eta_0)$* (10) *with an error $O(\varepsilon^2)$ according to* (11). *For $\Xi_0 \not\equiv 0$, the variable x changes in the general case by the value of δx of the order of unity with respect to a small parameter ε: $|\delta x| = |x - x^0| \sim O(1)$, $t \sim \frac{1}{\varepsilon^2}$.*

The Proof is virtually carried out in the above constructions and has a constructive character. If the function $X(t, x, \varepsilon)$ and the quantity $x^0(\varepsilon)$ depend explicitly on the small parameter ε in a smooth way [1–3], it should be (but not necessarily) expanded into a power series of ε [1–3] (see the examples in section 4). Of course, if the functions X, x^0 depend on ε in an unsmooth manner (for example, continuously), such expansions are impossible, and the dependence is taken into account completely.

3. Along with the first-order identity $X_0(\xi) \equiv 0$, the second-order identity $\Xi_0(\eta) \equiv 0$ can take place. In this case, the variable η does not change to a first approximation at the interval $t \sim \frac{1}{\varepsilon^2}$. According to (7), we obtain $\eta_0 = x^0$. As a result, $|\eta - x_0| = O(\varepsilon)$ [see (8)]. The variables x and η also change by the value of $O(\varepsilon)$ at $t \sim \frac{1}{\varepsilon^2}$, because

$$\dot\eta = \varepsilon^3\Xi_{10}(\eta) + \varepsilon^4 H(t, \eta, \varepsilon), \quad \eta(0) = x^0,$$
$$\Xi_{10}(\eta) = \frac{1}{2}\langle (X''_{x^2}(t, \eta)u(t, \eta), u(t, \eta))\rangle - \langle u'_\xi(t, \eta)X'_x(t, \eta)u(t, \eta)\rangle. \tag{12}$$

Provided that the right-hand side is reasonably smooth in η, it is possible to apply the method of separation of motions to system (12). This procedure leads to the first-approximation system and the estimates:

$$\dot\zeta_0 = \varepsilon^3\Xi_{10}(\zeta_0), \quad \zeta_0(0) = x^0, \quad \zeta_0 = \zeta_0(\varepsilon^3 t, x^0),$$
$$|\eta - \zeta_0| \le C_\eta\varepsilon, \quad |\xi - \zeta_0| \le C_\xi\varepsilon, \quad |x - \zeta_0| \le C_x\varepsilon, \quad 0 \le t \le \frac{L}{\varepsilon^3}. \tag{13}$$

Thus, for $X_0 = \Xi_0 \equiv 0$, a substantial variation of the variable x takes place at the interval $t \sim \frac{1}{\varepsilon^3}$ under the condition $\Xi_{10} \not\equiv 0$. The first approximation [with an error $O(\varepsilon)$] is determined by the function ζ_0 (13). A more exact calculation involves the standard scheme of the averaging method based on the explicit expressions for the functions $\Xi_{10}(\eta)$ and $H(t, \eta, \varepsilon)$. Similarly, we construct the set of evolutionary equations for slow variables of an arbitrary power of ε.

The above schemes are realizable on the basis of the standard procedure of the averaging method [1–6]:

$$x = \xi + \varepsilon U_1 + \varepsilon^2 U_2 + \ldots + \varepsilon^k U_k + \varepsilon^{k+1} + \ldots,$$
$$\dot\xi = \varepsilon\Theta(\xi, \varepsilon) \tag{14}$$
$$= \varepsilon\Theta_1 + \varepsilon^2\Theta_2 + \varepsilon^3\Theta_3 + \ldots + \varepsilon^k\Theta_k + \varepsilon^{k+1} + \ldots.$$

The coefficients U_i and Θ_i in the asymptotic expansions (14) are calculated with the derivatives of the function X at the point $x = \xi$ by quadratures and algebraic operations. The first-approximation system for an arbitrary kth power in ε and its solution ξ_1 have the form:

$$x = \xi + \varepsilon U_1 + \ldots + \varepsilon^k U_k,$$
$$\Theta_1 = \Theta_2 = \ldots = \Theta_{k-1} \equiv 0, \quad \Theta_k \not\equiv 0,$$
$$\dot\xi_1 = \varepsilon^k\Theta_k(\xi_1), \quad \xi_1(0) = x^0, \quad \xi_1 = \xi_1(\varepsilon^k t, x^0), \tag{15}$$
$$|\xi - \xi_1| \le C_\xi\varepsilon, \quad |x - \xi_1| \le C_x\varepsilon, \quad 0 \le t \le \frac{L}{\varepsilon^k},$$

and the following proposition is valid.

Theorem 2. *Let the identities $\Theta_1 = \Theta_2 = \ldots = \Theta_{k-1} \equiv 0$ be fulfilled in the k*th *approximation in ε using scheme* (14), *but $\Theta_k(\xi) \not\equiv 0$, $k \ge 1$. In this case, the qualitative evolution of set* (1) *proceeds at the interval $0 \le t \le \frac{L}{\varepsilon^k}$ and is described by the function $\xi_1(\varepsilon^k t, x^0)$* (15) *with an error $O(\varepsilon)$.*

Proof of the proximity of x and ξ_1 at $0 \le t \le \frac{L}{\varepsilon^k}$ is carried out by using integral inequalities.

Along with the averaging method [1–6], the recurrence accelerated-convergence method of the Newton-type can be used for constructing the averaged system. At the kth step, we have the system [provided that $\langle X_{(k-1)}\rangle = O(\varepsilon^{\theta(k-1)})$ or less]

$$\dot{x}_{(k)} = \varepsilon^{\theta(k)} X_{(k)}(t, x_{(k)}, \varepsilon), \quad \theta(k) = 2^k. \tag{16}$$

The evolution of the variable x is determined on the basis of system (16) if the average value $\langle X_{(k)}\rangle = O(\varepsilon^K)$, where $0 \le K \le \theta(k) - 1$. The evolutionary first-approximation equations are reduced to form (15). A substantial variation of the variable x takes place at the argument interval $0 \le \tau \le \dfrac{L}{\varepsilon^K}$, $\tau = \varepsilon^{\theta(k)}t$.

4. We investigate the nonlinear vibratory systems whose substantial evolution requires the application of the scheme of averaging the second power of ε.

4.1. For the purpose of illustration, we first take the scalar equation (1) with $X = \sin(t + x)$, which allows analytic integration. Using the averaging method, we obtain the desired solution to the Cauchy problem; i.e., the expression for x in the second approximation with respect to ε:

$$\begin{aligned} x &= \xi_{(1)}(\tau, x^0) + \varepsilon(\cos x^0 - \cos(x^0 + t)) + O(\varepsilon^2) \\ &= x^0 + O(\varepsilon), \\ \xi_{(1)} &\equiv x^0 - \frac{1}{2}\tau, \quad \tau = \varepsilon^2 t, \quad 0 \le t \le \frac{L}{\varepsilon}. \end{aligned} \tag{17}$$

We will now apply the second-power averaging scheme. On the basis of Theorem 1, the desired solution is obtained in the first and second approximations:

$$\begin{aligned} x &= \xi_{(1)}(\tau, x^0) + \varepsilon[\cos x^0 - \cos(t + \xi_{(1)})] + O(\varepsilon^2) \\ &= \xi_{(1)}(\tau, x^0) + O(\varepsilon), \quad 0 \le t \le \frac{L}{\varepsilon^2}. \end{aligned} \tag{18}$$

From the comparison of expressions (17) and (18), it follows that the first term $\xi_{(1)}$ of the expansion determines the second-power solution with an error of $O(\varepsilon)$ at the interval $t \sim \dfrac{1}{\varepsilon^2}$. Over the time $0 \le t \le \dfrac{L}{\varepsilon^2}$, a substantial evolution takes place; i.e., $\delta x \sim 1$.

4.2. We consider a quasilinear vibratory system under the action of two-frequency perturbation and linear dissipation in the form:

$$\begin{aligned} \ddot{y} + \omega^2 y &= \varepsilon F(t, y, \dot{y}, \varepsilon), \quad y(0) = a, \quad \dot{y}(0) = v, \\ F &\equiv h\sin 2\omega t + \alpha y^2 \\ &+ \varepsilon(f\sin(\omega t + \varphi) + \beta y^3 - \lambda\dot{y}) + \varepsilon^2\gamma y^4 + \varepsilon^3 + \ldots . \end{aligned} \tag{19}$$

The parameters α, β, and γ in (19) are determined by higher derivatives of the restoring-force function at the equilibrium point. Introducing a dimensionless time ($\omega t \longrightarrow t$), renaming parameters, and adopting the Vander-Pol osculating variables $x = (x_1, x_2)^T$ in (19), we obtain the set of equations of type (1) in Bogolyubov standard form [1–3]. In the first approximation, according to Theorem 1 for the averaged variable η, the equation of type (7) is obtained with the argument $\tau = \varepsilon^2 t$:

$$\begin{aligned} \dot{\eta} &= p + d\eta^2 J\eta + \left(\frac{\alpha h}{6}E - I\frac{\lambda}{2}\right)\eta, \\ p &= \frac{f}{2}(-\cos\varphi, \sin\varphi)^T, \quad E = \operatorname{diag}(1, -1). \end{aligned} \tag{20}$$

The coefficient d is expressed in terms of α and β; J is the symplectic unit. Set (20) has structural properties and can be adequately investigated by analytical and qualitative phase-plane methods. In particular, without the external action ($h = f = 0$), it is integrated in elementary functions [6]. The nonlinear perturbations $O(\varepsilon y^2)$ and $O(\varepsilon^2 y^3)$ lead to the actions $t \sim \dfrac{1}{\varepsilon^2}$, which are identical in structure at the interval $O(\varepsilon^2\eta^2\eta_{1,2})$. They have a conservative character, the former being independent of the sign α, while the latter is determined by a value of β that can lead to their mutual compensation. The harmonic action $\varepsilon h\sin 2t$ (19) for a reasonably high $|\alpha h|$ leads to unstable stationary points of the saddle type (in particular, for $f = 0$). For $h = 0$, we obtain a vibratory system, which is quite substantive in the mechanical aspect. This system is similar to the Duffing oscillator, which has been well studied with respect to other resonance relationships [7–10]. Thus, the approach described shows that interesting evolutionary processes proceed at the interval of $\dfrac{1}{\varepsilon^2}$ in set (19), none of which manifest themselves in the standard investigation $\left(t \sim \dfrac{1}{\varepsilon}\right)$.

4.3. We consider the motion of a plane physical pendulum, whose axis executes one-frequency vibrations with allowance for viscous-force moment [6]. Contrary to the case of fast vibrations [1–3], we assume that a frequency of small vibrations is comparable to the excitation frequency. An amplitude of vibrations of the suspension point and the viscous-friction moment are considered to be relatively small values. We investigate the case of resonant quasilinear vibrations of the system leading to the second-order averaging scheme (in the neighbourhood of the second zone):

$$\begin{aligned} &\ddot{y} + (4 - \varepsilon\cos 2t)y \\ &= \varepsilon^2\left[\kappa\sin(2t + \delta) - 4\gamma y + \frac{2}{3}y^3 - \sigma\dot{y}\right] + O(\varepsilon^3). \end{aligned} \tag{21}$$

The substantial distinction between Eqs. (20) and (19) lies in parametric excitation. Additional constructions are similar to the above constructions. As a result, the averaged system is obtained:

$$\dot{\eta} = \left(\frac{\eta^2}{8} - \gamma\right)J\eta + p + \left(N - \frac{\sigma}{2}I\right)\eta, \quad I = \mathrm{diag}(1, 1), \tag{22}$$
$$p = \frac{\kappa}{4}(-\cos\delta, \sin\delta)^T, \quad N\eta = \frac{1}{192}(\eta_2, 5\eta_1)^T.$$

Here, γ determines the frequency mismatch; κ and δ are the amplitude and phase of horizontal vibrations of the suspension point, and σ is the coefficient of dissipation. The solution $\eta_{1,2}$ ($\varepsilon^2 t$, x_1^0, x_2^0) to the self-governing set (22) determines the variables $x_{1,2}$ and y, $\dot{y}$ with an error of $O(\varepsilon)$ at the interval $t \sim \frac{1}{\varepsilon^2}$. This set can be sufficiently fully investigated by the phase-plane methods. The extension of this investigation scheme to the interval $t \sim \frac{1}{\varepsilon^2}$ makes it possible to reveal some rather interesting features of the evolution of vibrations of a pendulum with a slowly vibrating suspension point in the ε^2-vicinity of the considered resonance mode (22).

ACKNOWLEDGMENTS

This work was supported by the Russian Foundation for Basic Research, project nos. 99-01-00222 and 99-01-00276.

REFERENCES

1. N. N. Bogolyubov and Yu. A. Mitropol'skiĭ, *Asymptotic Methods in the Theory of Nonlinear Oscillations* (Nauka, Moscow, 1974, 4th ed.; Gordon and Breach, New York, 1962).
2. V. M. Volosov, Usp. Mat. Nauk **17** (6), 3 (1962).
3. Yu. A. Mitropol'skiĭ, *Averaging Method in Nonlinear Mechanics* (Naukova Dumka, Kiev, 1971).
4. J. G. Besjes, J. Mech. **8** (3), 357 (1969).
5. V. I. Arnol'd, V. V. Kozlov, and A. I. Neĭshtadt, *Dynamic Systems*, Vol. 3: *Mathematical Aspects of Classical and Celestial Mechanics* (VINITI, Moscow, 1985).
6. L. D. Akulenko, *Asymptotic Methods of Optimal Control* (Nauka, Moscow, 1987).
7. A. Blaquiere, *Nonlinear System Analysis* (Academic, New York, 1967; Mir, Moscow, 1969).
8. H. Kauderer, *Nichtlineare Mechanik* (Springer-Verlag, Berlin, 1958; Inostrannaya Literatura, Moscow, 1961).
9. L. D. Akulenko and S. V. Nesterov, Prikl. Mat. Mekh. **60**, 88 (1996).
10. L. D. Akulenko, G. V. Kostin, and S. V. Nesterov, Izv. Akad. Nauk, Mekh. Tverd. Tela, No. 1, 19 (1997).

Translated by V. Bukhanov

Doklady Physics, Vol. 46, No. 9, 2001, pp. 659–662. Translated from Doklady Akademii Nauk, Vol. 380, No. 1, 2001, pp. 43–46.

MECHANICS

An Analog of the Centered Riemann Wave in Heat-Conducting Inviscid Gas

S. P. Bautin and Yu. Yu. Chernyshov

Presented by Academician Yu.I. Shokin March 14, 2001

Received April 13, 2001

A centered Riemann wave describes certain plane-symmetric gas flows. This wave represents the solution to the system of gasdynamic equations with a specific singularity of the form

$$\mathbf{U} = \mathbf{U}\left(\frac{x_1 - x_*}{t - t_*}\right),$$

where $\mathbf{U}$ is the vector of the desired functions and x_* and t_* are arbitrary constants. The centered Riemann wave is used to solve many meaningful problems of gas dynamics [1]. In the case of cylindrically and spherically symmetric flows, the self-similar solutions $\mathbf{U} = \mathbf{U}\left(\frac{r}{t - t_*}\right)$ derived by L.I. Sedov [2] possess a similar singularity but only in the vicinity of the point $r = 0$. In particular, these solutions describe the focusing of a compression wave onto a certain axis or a center of symmetry [3]. Flows that possess properties of a centered Riemann wave in the vicinity of the point $r = r_* > 0$ or in the many-dimensional case are described by a special convergent infinite series (detailed references are presented in [4]). Such series are used to solve problems on the instantaneous stopping of a piston, on gas outflow into vacuum, and on strong shock-free gas compression. In problems of strong gas compression, an adequate description of the arising flows requires that both the equilibrium radiation and the Compton scattering of photons be taken into account [3, 5].

In this paper, with the help of a special infinite convergent series, we describe a certain flow of a heat-conducting inviscid gas, which is similar to a centered Riemann wave and is characterized by the strong compression of one-dimensional gas layers with allowance for the above-mentioned physical effects.

For this purpose, the spatial variable and one of the desired functions exchange roles. A special condition that automatically ensures the presence of the required flow singularity is imposed on the system of equations to be derived. The solution to the problem under consideration is written as an infinite series, and the coefficients satisfying recursion relations are obtained. It is proven that in the case of the analyticity of the input data the problem to be solved represents the standard form of the characteristic Cauchy problem [4] for which the analog of the Kovalevskaya theorem [4] is valid. Consequently, the constructed series is locally convergent. By thoroughly analyzing the structure of coefficients of the series, we ascertain the unboundedness of the series-convergence region with respect to one of the variables. The explicit form of the first coefficients of the series shows that in the physical space the solution obtained has the same singularity as a centered Riemann wave.

The solution constructed in this paper is used to describe the strong shock-free compression of one-dimensional gas layers with allowance for equilibrium radiation and the Compton scattering of photons. It is proven that due to the unboundedness of the series-convergence region, for any finite density given *a priori*, there exists a nonzero mass of initially quiescent and homogeneous gas of unit density such that the mass can be compressed to this finite density. The approximate variation law for the gas density in a piston providing the required compression is found as well.

We consider a perfect gas with allowance for equilibrium radiation. In other words, we take the following relations (see [5]) as equations of state:

$$p = R\rho T + \frac{\sigma}{3}T^4, \quad e = c_{v0}T + \sigma\frac{T^4}{\rho}, \qquad (1)$$
$$R, \sigma, c_{v0} = \text{const} > 0.$$

Here, p, T, ρ, e, and σ are pressure, temperature, density, internal energy, and the Stefan–Boltzmann constant, respectively.

Since the Compton scattering of photons is taken into account, the thermal-conduction coefficient κ has the form [5]

$$\kappa = \frac{2}{\gamma - 1}\sigma c\alpha\frac{T^3}{\rho}, \quad \gamma - 1 = \frac{R}{c_{v0}} > 0, \qquad (2)$$

Ural State University of Communication,
ul. Kolmogorova 66, Ekaterinburg, 620034 Russia

1028-3358/01/4609-0659$21.00

where c is the speed of light and ρ is a positive constant depending on a chosen system of units.

To describe the flows of such a gas, we can consider ρ and T as independent thermodynamic variables. Therefore, it is possible to use the complete system of Navier–Stokes equations in which the coefficients of dynamic (μ) and volume (μ') viscosity are assumed to be zero [6]. In the case of one-dimensional flows, the substitution of the function $\vartheta = \ln\rho$ as a desired function instead of the density turns this system into the form

$$\vartheta_t + u\vartheta_r + u_r + \nu\frac{u}{r} = 0,$$

$$u_t + uu_r + \frac{T}{\gamma}\vartheta_r + a(\vartheta, T)T_r = 0,$$

$$T_t + uT_r + b(\vartheta, T)\left(u_r + \nu\frac{u}{r}\right)$$

$$= \kappa_0 c(\vartheta, T)\left(T_{rr} + \frac{\nu}{r}T_r - \vartheta_r T_r + \frac{3}{T}T_r^2\right), \qquad (3)$$

$$a(\vartheta, T) = \frac{1}{\gamma}(1 + \kappa_0 k_1 \exp(-\vartheta)T^3),$$

$$b(\vartheta, T) = (\gamma - 1)T\frac{1 + \kappa_0 k_1 \exp(-\vartheta)T^3}{1 + \kappa_0 k_2 \exp(-\vartheta)T^3},$$

$$c(\vartheta, T) = \frac{\exp(-2\vartheta)T^3}{1 + \kappa_0 k_2 \exp(-\vartheta)T^3}.$$

Here, the values of $\nu = 0$, 1, and 2 correspond to the plane, cylindrical, and spherical symmetries, respectively. Dimensionless variables are introduced in the standard manner with the help of the positive constants L, ρ_{00}, and T_{00}. Moreover, the sound velocity in a non-heat-conducting gas $u_{00} = \sqrt{R\gamma T_{00}}$ is taken as a velocity measure so that

$$\kappa_0 = 2\sigma c\alpha\frac{T_{00}^3}{R\rho_{00}^2 u_{00}L} > 0,$$

$$k_1 = \frac{2\rho_{00}u_{00}L}{3c\alpha} > 0, \quad k_2 = 3(\gamma - 1)k_1 > 0.$$

Similar to the case of a non-heat-conducting gas [4], the roles of the variables ϑ and r are mutually exchanged to describe singularities arising in a gas flow at the moment of strong compression. The variable ϑ (together with t) is considered to be independent, while r becomes a desired function of t and ϑ. In other words, we replace the variables $t = t'$ and $r = r(t', \vartheta)$ with the Jacobian transformation $J = -r_\vartheta$. This turns system (3) into

$$r(u - r_t) + ru_\vartheta + \nu u r_\vartheta = 0,$$

$$r_\vartheta u_t + (u - r_t)u_\vartheta + \frac{T}{\gamma} + a(\vartheta, T)T_\vartheta = 0, \qquad (4)$$

$$r_\vartheta^2\left[r_\vartheta T_t + (u - r_t)T_\vartheta + b(\vartheta, T)\left(u_\vartheta + \nu\frac{u}{r}r_\vartheta\right)\right]$$

$$= \kappa_0 c(\vartheta, T)\left(r_\vartheta T_{\vartheta\vartheta} - r_{\vartheta\vartheta}T_\vartheta + \frac{\nu}{r}r_\vartheta^2 T_\vartheta - r_\vartheta T_\vartheta + \frac{3}{T}r_\vartheta T_\vartheta^2\right).$$

(Here, the prime at t is omitted in order to simplify the notation.)

The solution to system (4) is constructed as the series

$$\mathbf{U}(t, \vartheta) = \sum_{k=0}^{\infty}\mathbf{U}_k(\vartheta)\frac{(t - t_*)^k}{k!},$$
$$\mathbf{U}_k(\vartheta) = \left.\frac{\partial^k\mathbf{U}(t, \vartheta)}{\partial t^k}\right|_{t = t_*}, \qquad (5)$$

where $\mathbf{U} = \{r, u, T\}$ is the desired vector function and t_* is the given time instant.

Since we seek the flow with a singularity similar to that of the centered Riemann wave, a plot of the function $\vartheta = \vartheta(t, r)|_{t = \text{const}}$ as $t \longrightarrow t_* - 0$ must turn into a vertical straight line [4]

$$r|_{t = t_*} = r_* = \text{const} > 0. \qquad (6)$$

The solution to the system of equations (4) is constructed in the form of series (5) under condition (6), which defines the coefficient $r_0(\vartheta)$.

To derive equations for the coefficients $r_1(\vartheta)$, $u_0(\vartheta)$, and $T_0(\vartheta)$, we should allow for condition (6), while setting $t = t_*$ in the first two equations of system (4) (then, the third equation turns into the identity) and differentiating once the third equation with respect to t. This procedure leads to the following system of three differential equations, with two of them being nonlinear:

$$r_*(u_0 - r_1) + r_* u_0' = 0,$$

$$(u_0 - r_1)u_0' + \frac{T_0}{\gamma} + a(\vartheta, T_0)T_0' = 0, \qquad (7)$$

$$r_1'T_0'' - r_1''T_0' - r_1'T_0' + \frac{3}{T}r_1'(T_0')^2 = 0.$$

Finding the general solution to this system seems to be a rather difficult task. Therefore, we take as the function $T_0(\vartheta)$ the constant

$$T_0(\vartheta) = T_{01} = \text{const} > 0, \qquad (8)$$

which turns the last equation of system (7) into an identity. There are two reasons for using the partial

solution (8) here. First, the similar property is inherent in the entropy of a non-heat-conducting gas (see [4]), i.e., $S|_{t=t_*}$ = const. Second, in the plane-symmetric case, it is this property of the temperature, the absence of a jump of the function T at the time moment $t = t_*$, that is observed in numerical calculations of the corresponding compression wave in a heat-conducting gas [5]. For the partial solution (8), the other two equations of the system of equations (7) have the following general solution:

$$u_0(\vartheta) = \pm\sqrt{\frac{T_{01}}{\gamma}}\vartheta + u_{01},$$
$$r_1(\vartheta) = \pm\sqrt{\frac{T_{01}}{\gamma}}\vartheta + u_{01} \pm \sqrt{\frac{T_{01}}{\gamma}}. \quad (9)$$

The integration resulted in the unambiguous definition of the function $r_1(\vartheta)$ and the appearance of two arbitrary constants T_{01} and u_{01} in relationships (8) and (9).

To obtain the coefficients r_{k+1}, u_k, and T_k at $k \geq 2$, we should differentiate the first two equations and the third equation of system (4) k and $k+1$ times with respect to t, respectively, and then set $t = t_*$. This procedure yields the equations

$$r_*(u_k - r_{k+1}) + r_* u_k' = F_k,$$
$$kr_1' u_k + (u_0 - r_1)u_k' + u_0'(u_k - r_{k+1}) + \frac{T_k}{\gamma} + a(\vartheta, T_{01})T_k' = G_k,$$
$$\kappa_0 r_* T_{01}(k+1)r_1'(T_k'' - T_k') = H_k,$$

where the functions F_k, G_k, and H_k depend on r_{l+1}, u_l, T_l $(0 \leq l \leq k-1)$, and their derivatives (due to their awkwardness, the specific forms of these functions are not presented here).

Initially, the third (differential) equation is used to determine

$$T_k = T_{k0} + T_{k1}\exp\vartheta - a_k\int H_k d\vartheta + a_k\int H_k\exp(-\vartheta)d\vartheta, \quad (10)$$

where T_{k0} and T_{k1} are arbitrary constants while a_k represents particular numbers. Then, after the preliminary elimination of r_{k+1} with the help of the first equation, we find from the second (differential) equation

$$u_k = u_{k0}\exp(k\vartheta/2) + \frac{\exp(k\vartheta/2)}{2}\int\left[\mp\sqrt{\frac{\gamma}{T_{01}}}G_k - \frac{F_k}{r_*}\right]\exp(-k\vartheta/2)d\vartheta \quad (11)$$

with one arbitrary constant u_{k0}. Finally, the first (algebraic) equation unambiguously determines the function

$$r_{k+1} = u_k' + u_k - \frac{F_k}{r_*}. \quad (12)$$

The arbitrariness that arises in the construction of series (5) is equivalent to the specification of the conditions

$$u(t, \vartheta)|_{\vartheta=\vartheta_*} = u^0(t),$$
$$T(t, \vartheta)|_{\vartheta=\vartheta_*} = T^0(t), \quad T_\vartheta(t, \vartheta)|_{\vartheta=\vartheta_*} = T^1(t), \quad (13)$$

where the arbitrary functions appearing on their right-hand sides satisfy the relations

$$u^0(t_*) = u_{01}, \quad T^0(t_*) = T_{01}, \quad T^1(t_*) = 0.$$

Theorem. *If the functions $u^0(t)$, $T^0(t)$, and $T^1(t)$ entering in conditions* (13) *are analytic in a certain neighborhood of the point $t = t_*$, then series* (5) *is convergent in a certain vicinity of the point $(t = t_*, \vartheta = \vartheta_*)$.*

In proving this theorem by the known procedure described in [4], we reduce problem (4), (6), (13) to a certain standard form that satisfies the analog of the Kovalevskaya theorem on the existence and uniqueness of the solution in the class of analytic functions [4].

The refinement of the convergence region for the series is attained by thoroughly analyzing the functions r_{k+1}, u_k and T_k.

Lemma. *At $k \geq 1$, the coefficients r_{k+1}, u_k, and T_k are polynomials* [*in both ϑ and* $\exp(\vartheta/2)$] *such that the maximum total power of the monomials in them of the form $\vartheta^n\exp(m\vartheta/2)$ does not exceed $2k$; i.e., $n + m/2 \leq 2k$. In addition, each of the functions r_{k+1}, u_k, and T_k necessarily contain a monomial of the form* $\exp(2k\vartheta)$ *with a nonzero coefficient in front of it.*

The **proof** of the lemma is carried out by induction on k with the use of formulas (10)–(13) and repeats, in its principal features, the corresponding proofs for a non-heat-conducting gas [4].

The lemma makes possible the derivation of the following formula for a convergence region of series (5), which solves problems (4), (6), (13):

$$M\exp(2\vartheta)|t - t_*| < 1, \quad M = \text{const} > 0, \quad (14)$$

Thus, this region turns out to be unbounded in the variable ϑ.

With allowance for formulas (8) and (9), series (5) can be written out as

$$\begin{aligned}\vartheta &= \left(\mp\sqrt{\frac{\gamma}{T_{01}}}u_{01} - 1\right)\\ &\pm\sqrt{\frac{\gamma}{T_{01}}}\frac{(r-r_*)}{(t-t_*)} + (t-t_*)f(t,\vartheta),\\ u &= \left(\pm\sqrt{\frac{T_{01}}{\gamma}}\vartheta + u_{01}\right) + (t-t_*)g(t,\vartheta),\\ T &= T_{01} + (t-t_*)h(t,\vartheta),\end{aligned} \tag{15}$$

where the functions $f(t, \vartheta)$, $g(t, \vartheta)$ and $h(t, \vartheta)$ are analytic in region (14). According to the theorem of the existence of an implicit function, the first relation in (15) determines ϑ as a function of the variables $\frac{r-r_*}{t-t_*}$ and t.

The Jacobian for the transition from the variables t, r to the variables t', ϑ can be represented in the form

$$J = -r_\vartheta = \mp\sqrt{\frac{T_{01}}{\gamma}}(t-t_*) + (t-t_*)^2 q(t,\vartheta),$$

where the function $q(t, \vartheta)$ is also analytic in region (14). Therefore, at $t = t_*$, the Jacobian vanishes, and for any finite value $\vartheta_0 > 0$ there exists $t_0 > 0$ such that $J \neq 0$ for $|\vartheta| < \vartheta_0$ and $|t - t_*| < t_0$.

Consequently, the constructed series (5) describes the flow of a heat-conducting gas with a mathematical singularity in the physical space at the point $r = r_*$ and the time instant $t = t_*$. This singularity is similar to that of the velocity and density inherent in a centered Riemann wave. As $t \longrightarrow t_*$, the principal part of the flow is described by the first terms of formulas (15). In particular, this part is independent of the constant ν and, consequently, is identical for all types of symmetry.

The known method (see [4]) allows for the determination of the asymptotic behavior (as $t \longrightarrow t_* - 0$) of gas parameters in a piston that generates a compression wave described by series (5). Let the function $\vartheta = \Theta(t)$ specify the value of ϑ in the impermeable piston. Then, the differential equation occurs (see [4])

$$r_\Theta(t,\Theta)\frac{d\Theta}{dt} + r_t(t,\Theta) = u(t,\Theta). \tag{16}$$

After retaining only the principal terms in Eq. (16), it turns into the equation

$$(t-t_*)\frac{d\Theta(t)}{dt} = -1,$$

having the general solution

$$\Theta(t) = -\ln\left(\frac{t_*-t}{\rho_{01}}\right), \quad \rho_{01} = \text{const} > 0. \tag{17}$$

Formula (17) represents, of course, a certain approximation to the desired dependence $\Theta(t)$. This formula yields the following approximate dependence for the gas density in the compressing piston:

$$\rho \approx \frac{\rho_{01}}{t_* - t}.$$

The unboundedness (in the variable ϑ) of the convergence region for series (5) leads to the following mathematically-based conclusion: for any given density $\rho_* > 1$, there exists a nonzero mass of an inert and homogeneous gas with the density $\rho = 1$, which, under the action of an impermeable piston, admits shock-free compression to the density ρ_*. This conclusion follows from the fact that for any $\rho_* > 1$ we can choose that trajectory of the compressing-piston motion belonging to region (14), i.e., to the convergence region of series (5) at all values $0 \le \Theta \le \vartheta_* = \ln(\rho_*)$. Then, the value $t_1 - t_0$ specifies the initial width of a gas layer with the density $\rho = 1$ further compressed to the final density $\rho = \rho_*$. Here, the time moments t_1 and t_0 are such that $\Theta(t_1) = \vartheta_*$ and $\Theta(t_0) = 0$.

REFERENCES

1. B. L. Rozhdestvenskiĭ and N. N. Yanenko, *Systems of Quasilinear Equations and Their Applications to Gas Dynamics* (Nauka, Moscow, 1968).
2. L. I. Sedov, *Similarity and Dimensional Methods in Mechanics* (Academic, New York, 1959; Nauka, Moscow, 1981).
3. E. I. Zababakhin and I. E. Zababakhin, *Phenomena of Unlimited Cumulation* (Nauka, Moscow, 1988).
4. S. P. Bautin, *Mathematical Theory of Strong Shock-Free Compression for Ideal Gas* (Nauka, Novosibirsk, 1997).
5. M. G. Anuchin, Prikl. Mekh. Tekh. Fiz. **39** (4), 25 (1998).
6. S. P. Bautin, Prikl. Mat. Mekh. **52**, 579 (1988).

Translated by Yu. Verevochkin

Doklady Physics, Vol. 46, No. 9, 2001, pp. 663–666. Translated from Doklady Akademii Nauk, Vol. 380, No. 1, 2001, pp. 47–50.

MECHANICS

Kinematics and Mass Geometry for a Solid Body with a Fixed Point in $\mathbb{R}^n$

D. V. Georgievskiĭ and M. V. Shamolin

Presented by Academician A.Yu. Ishlinskiĭ April 9, 2001

Received April 10, 2001

1. Let a fixed rectangular Cartesian coordinate system (Ox_i) with the unit vectors $\mathbf{e}_i$ be given in the space $\mathbb{R}^n$ $(\mathbf{e}_i \cdot \mathbf{e}_j = \delta_{ij};\ i = 1, 2, \ldots, n)$. The origin O of this coordinate system is assumed to coincide with a fixed point on an n-dimensional body that is perfectly rigid and moving in $\mathbb{R}^n$. The time dependences of the body's volume and surface are represented by V_t and Σ_t, respectively.

We introduce the radius vector $\mathbf{r} = x_i\mathbf{e}_i$ $(|\mathbf{r}| = r = \sqrt{x_i x_i})$, the velocity vector $\dot{\mathbf{r}} = \mathbf{v} = v_i\mathbf{e}_i$, and the acceleration vector $\ddot{\mathbf{r}} = \mathbf{w} = w_i\mathbf{e}_i$. The velocity $\mathbf{v}$ is related to $\mathbf{r}$ by the generalized Euler formula

$$\mathbf{v} = \boldsymbol{\Omega}^{\{n-2\}} \times \mathbf{r}. \tag{1}$$

Here, $\boldsymbol{\Omega}^{\{n-2\}}$ is the tensor of rank $n-2$, which is referred to as an angular-velocity tensor or, simply, as an angular velocity $(\boldsymbol{\Omega}^{\{n-2\}} = \Omega_{i_1\ldots i_{n-2}}\mathbf{e}_{i_1} \otimes \ldots \otimes \mathbf{e}_{i_{n-2}})$ that depends only on time.

One should keep in mind that in the space $\mathbb{R}^n$ the generalized cross product of the vectors $\mathbf{A}^{\{m\}}$ and $\mathbf{B}^{\{q\}}$ of the ranks m and q (with $m + q \le n$), respectively, is, generally, a pseudotensor $\mathbf{C}^{\{n-m-q\}}$ of the rank $n-m-q$ with the components

$$C_{i_{m+q+1}\ldots i_n} = \epsilon_{i_1\ldots i_n}A_{i_1\ldots i_m}B_{i_{m+1}\ldots i_{m+q}}. \tag{2}$$

Hereafter, the summation over twice repetitive Latin indices from 1 to n is assumed, with free indices also ranging from 1 to n. In (2), $\epsilon_{i_1\ldots i_n}$ is the n-dimensional Levi-Civita symbol. Together with it, we also use the generalized Kronecker symbol $\delta^{i_1\ldots i_n}_{j_1\ldots j_n}$ defined as:[1]

$$\delta^{i_1\ldots i_n}_{j_1\ldots j_n} = \epsilon_{i_1\ldots i_n}\epsilon_{j_1\ldots j_n} = \begin{vmatrix} \delta_{i_1j_1} & \ldots & \delta_{i_1j_n} \\ \vdots & \ddots & \vdots \\ \delta_{i_nj_1} & \ldots & \delta_{i_nj_n} \end{vmatrix}, \tag{3}$$

the sum being over its upper and lower indices standing one on top of the other

$$\delta^{i_1\ldots i_{n-1}l}_{j_1\ldots j_{n-1}l} = \begin{vmatrix} \delta_{i_1j_1} & \ldots & \delta_{i_1j_{n-1}} \\ \vdots & \ddots & \vdots \\ \delta_{i_{n-1}j_1} & \ldots & \delta_{i_{n-1}j_{n-1}} \end{vmatrix}. \tag{4}$$

In the orthogonal Cartesian coordinate system used for this paper, the quantity $\mathbf{C}^{\{n-m-q\}}$ is a true tensor [1]. With regard to (2), the Euler formula (1) can be written in the component form $(m = n-2,\ q = n-m-q = 1)$:

$$v_k = \epsilon_{i_1\ldots i_{n-2}lk}\Omega_{i_1\ldots i_{n-2}}x_l. \tag{5}$$

As follows from (5), the angular velocity must be antisymmetric with respect to the permutation of any pair of its indices. Hence, the number of independent components of the tensor $\boldsymbol{\Omega}^{\{n-2\}}$ having n^{n-2} components is equal to $C_n^{n-2} = C_n^2 = \frac{1}{2}n(n-1) = N$. Hence, the tensor $\boldsymbol{\Omega}^{\{n-2\}}$ can be related to the antisymmetric dual tensor $\boldsymbol{\omega}^{\{2\}} = \omega_{ij}\mathbf{e}_i \otimes \mathbf{e}_j$ of the second order, i.e., the dual angular velocity, by the formulas

$$\begin{aligned} \omega_{lk} &= \epsilon_{i_1\ldots i_{n-2}lk}\Omega_{i_1\ldots i_{n-2}}, \\ \boldsymbol{\omega}^{\{2\}} &= \boldsymbol{\Omega}^{\{n-2\}} \times 1 = 1 \times \boldsymbol{\Omega}^{\{n-2\}}. \end{aligned} \tag{6}$$

Then, equalities (1) and (5) can be represented in terms of the dual angular velocity:

$$\mathbf{v} = -\boldsymbol{\omega}^{\{2\}} \cdot \mathbf{r}, \quad v_k = \omega_{lk}x_l. \tag{7}$$

Multiplying both sides of relationship (6) by $\epsilon_{j_1\ldots j_{n-2}lk}$,

$$\begin{aligned} \epsilon_{j_1\ldots j_{n-2}lk}\omega_{lk} &= \delta^{i_1\ldots i_{n-2}lk}_{j_1\ldots j_{n-2}lk}\Omega_{i_1\ldots i_{n-2}} \\ &= 2(n-2)!\Omega_{j_1\ldots j_{n-2}}, \end{aligned} \tag{8}$$

[1] For the generalized Kronecker delta, we use the upper and lower indices for brevity only; they do not stand for covariant or contravariant tensor components.

Moscow State University,
Vorob'evy gory, Moscow, 119899 Russia

1028-3358/01/4609-0663$21.00

we arrive at the inversion of (6):

$$\Omega_{j_1\dots j_{n-2}} = \frac{1}{2(n-2)!}\epsilon_{lkj_1\dots j_{n-2}}\omega_{lk},$$
$$\boldsymbol{\Omega}^{\{n-2\}} = \frac{\boldsymbol{\omega}^{\{2\}}\times 1}{2(n-2)!} = \frac{1\times\boldsymbol{\omega}^{\{2\}}}{2(n-2)!}. \quad (9)$$

Thus, according to (6) and (9), the angular velocity and dual angular velocity are unambiguously expressed in terms of one another and in terms of the following differential operators of the first order with respect to $\mathbf{v}$:

$$(\mathrm{Grad}\mathbf{v})^{\{2\}} = \nabla\otimes\mathbf{v} = \frac{\partial v_k}{\partial x_l}\mathbf{e}_l\otimes\mathbf{e}_k = \omega_{lk}\mathbf{e}_l\otimes\mathbf{e}_k = \boldsymbol{\omega}^{\{2\}}, \quad (10)$$

$$(\mathrm{rot}\mathbf{v})^{\{n-2\}} = \nabla\times\mathbf{v} = \epsilon_{lki_1\dots i_{n-2}}\frac{\partial v_k}{\partial x_l}\mathbf{e}_1\otimes\dots\otimes\mathbf{e}_{i_{n-2}}$$
$$= \epsilon_{lki_1\dots i_{n-2}}\omega_{lk}\mathbf{e}_1\otimes\dots\otimes\mathbf{e}_{i_{n-2}} = 2(n-2)!\boldsymbol{\Omega}^{\{n-2\}}. \quad (11)$$

The angular-velocity vector $\boldsymbol{\Omega}\in\mathbb{R}^N$ can be formally associated with the tensors $\boldsymbol{\Omega}^{\{n-2\}}$ and $\boldsymbol{\omega}^{\{2\}}$. It is worth noting that in the case of $n = 3$ and $N = 3$ the quantity $\boldsymbol{\Omega}^{\{1\}}$ coincides with $\boldsymbol{\Omega}$. For $n = 2$, the angular velocity is a scalar associated with a unidimensional vector field, as opposed to a vector with a single(!) nonzero component.

We now consider the angular-acceleration tensor $\boldsymbol{\varepsilon}^{\{n-2\}} = \varepsilon_{i_1\dots i_{n-2}}\mathbf{e}_1\otimes\dots\otimes\mathbf{e}_{i_{n-2}}$ (angular acceleration) and the tensor $\mathbf{e}^{\{2\}} = e_{ij}\mathbf{e}_i\otimes\mathbf{e}_j$ (dual angular acceleration), which is dual to the first one in the sense of relationships (6) and (9):

$$\varepsilon_{i_1\dots i_{n-2}} = \dot{\Omega}_{i_1\dots i_{n-2}}, \quad e_{ij} = \dot{\omega}_{ij}. \quad (12)$$

As was the case with $\boldsymbol{\Omega}^{\{n-2\}}$ and $\boldsymbol{\omega}^{\{2\}}$, these tensors are antisymmetric with respect to the permutation of any pair of their indices. Differentiating both sides of (5) with respect to time, we arrive at the generalized Rivals formula, which can be written out in one of the following forms:

$$w_k = \epsilon_{i_1\dots i_{n-2}lk}\varepsilon_{i_1\dots i_{n-2}}x_l - \delta^{i_1\dots i_{n-2}kl}_{j_1\dots j_{n-2}ml}\Omega_{i_1\dots i_{n-2}}\Omega_{j_1\dots j_{n-2}}x_m, \quad (13)$$
$$\mathbf{w} = \boldsymbol{\varepsilon}^{\{n-2\}}\times\mathbf{r} + \boldsymbol{\Omega}^{\{n-2\}}\times(\boldsymbol{\Omega}^{\{n-2\}}\times\mathbf{r}),$$

$$w_k = e_{lk}x_l - \omega_{lk}\omega_{mk}x_m,$$
$$\mathbf{w} = -\mathbf{e}^{\{2\}}\cdot\mathbf{r} + \boldsymbol{\omega}^{\{2\}}\cdot\boldsymbol{\omega}^{\{2\}}\cdot\mathbf{r}. \quad (14)$$

2. We presented above the tensor approach for deriving the generalized Euler formula (5) and Rivals formula (13). We now obtain these formulas by the operator method.

To do this, we introduce the coordinate system (Ox_i') related to an n-dimensional solid body ($i = 1, 2, \dots, n$). Let M be an arbitrary point of the body. Then, its coordinates R_M in the Ox_i reference system are related to its coordinates r_M in the Ox_i' system (i.e., before the rotation about the fixed point O) by the equality

$$R_M = \hat{\Gamma}r_M, \quad (15)$$

where $\hat{\Gamma}\in\mathrm{SO}(n)$. By differentiating relationship (15) with respect to time, we obtain

$$v_M = \hat{\Omega}r_M, \quad \hat{\Omega} = \hat{\Gamma}\hat{\omega},$$
$$\hat{\omega} = \hat{\Gamma}^{-1}\dot{\hat{\Gamma}}\in\mathrm{so}(n), \quad (16)$$

where $\hat{\Omega}$ is the angular-velocity operator. The first equality in (16) is the Euler formula in $\mathbb{R}^n$ written in the operator form.

Rivals formula is derived similarly:

$$w_M = \dot{\hat{\Omega}}r_M + \hat{\Omega}\dot{r}_M = \hat{E}r_M + \hat{\Omega}^2 r_M, \quad \hat{E}\in\mathrm{so}(n), \quad (17)$$

where $\hat{E}$ is the angular-acceleration operator (see [2–4]). We now describe the operator $\hat{\Gamma}$ in detail. The rotation from the Ox_i' coordinate system to the Ox_i system is specified by coordinates in the system SO(n), i.e., by N angles of rotations in the corresponding two-dimensional planes perpendicular to the coordinate axes in SO(n).

The general form of the operator $\hat{\Gamma}$ is

$$\hat{\Gamma} = \hat{\Gamma}_N\hat{\Gamma}_{N-1}\dots\hat{\Gamma}_1. \quad (18)$$

In the case of a four-dimensional space ($N = 6$), representation (18) takes the form

$$\hat{\Gamma} = \begin{pmatrix}\cos\varphi_6 & \sin\varphi_6 & 0 & 0\\ -\sin\varphi_6 & \cos\varphi_6 & 0 & 0\\ 0 & 0 & 1 & 0\\ 0 & 0 & 0 & 1\end{pmatrix}\begin{pmatrix}\cos\varphi_5 & 0 & -\sin\varphi_5 & 0\\ 0 & 1 & 0 & 0\\ \sin\varphi_5 & 0 & \cos\varphi_5 & 0\\ 0 & 0 & 0 & 1\end{pmatrix}$$
$$\times\begin{pmatrix}1 & 0 & 0 & 0\\ 0 & \cos\varphi_4 & \sin\varphi_4 & 0\\ 0 & -\sin\varphi_4 & \cos\varphi_4 & 0\\ 0 & 0 & 0 & 1\end{pmatrix}\begin{pmatrix}\cos\varphi_3 & 0 & 0 & \sin\varphi_3\\ 0 & 1 & 0 & 0\\ 0 & 0 & 1 & 0\\ -\sin\varphi_3 & 0 & 0 & \cos\varphi_3\end{pmatrix} \quad (19)$$
$$\times\begin{pmatrix}1 & 0 & 0 & 0\\ 0 & \cos\varphi_2 & 0 & -\sin\varphi_2\\ 0 & 0 & 1 & 0\\ 0 & \sin\varphi_2 & 0 & \cos\varphi_2\end{pmatrix}\begin{pmatrix}1 & 0 & 0 & 0\\ 0 & 1 & 0 & 0\\ 0 & 0 & \cos\varphi_1 & \sin\varphi_1\\ 0 & 0 & -\sin\varphi_1 & \cos\varphi_1\end{pmatrix}.$$

Using the formulas described above and the interpretation given in [4], we found a new integrable case for $n = 4$ [5], which is an extension of the case $n = 3$ [6].

3. We will now consider the hyperplane motion (parallel to, e.g., the hyperplane π_n: $x_n = 0$) of an n-dimensional body with a fixed point for which the velocity components v_n of all the body's points are equal to zero. We prove that such a motion is the rotation in $\mathbb{R}^n$ about the x_n axis and is described by the angular-velocity tensor $\mathbf{\Omega}^{\{n-2\}}$ that has the following components:

$$\Omega_{i_1\ldots i_{n-2}} = \frac{1}{n-2}\sum_{j=1}^{n-2}(-1)^{n-j}\tilde{\Omega}_{i_1\ldots\hat{i}_j\ldots i_{n-2}}\delta_{i_jn}. \qquad (20)$$

Here, $\tilde{\Omega}_{i_1\ldots\hat{i}_j\ldots i_{n-2}} \equiv \tilde{\Omega}_{i_1\ldots i_{j-1}i_{j+1}\ldots i_{n-2}}$ are the components of a certain tensor $\tilde{\mathbf{\Omega}}^{\{n-3\}}$ of the rank $n-3$.

Substituting (20) into (5), we arrive at

$$\begin{aligned} v_k &= \frac{1}{n-2}\sum_{j=1}^{n-2}(-1)^{n-j}\epsilon_{i_1\ldots i_{n-2}lk}\tilde{\Omega}_{i_1\ldots\hat{i}_j\ldots i_{n-2}}\delta_{i_jn}x_l \\ &= \frac{1}{n-2}\sum_{j=1}^{n-2}(-1)^{n-j}\epsilon_{i_1\ldots i_{j-1}ni_{j+1}\ldots i_{n-2}lk}\tilde{\Omega}_{i_1\ldots\hat{i}_j\ldots i_{n-2}}x_l \\ &= \frac{1}{n-2}\sum_{j=1}^{n-2}(-1)^{2(n-j)}\epsilon_{i_1\ldots\hat{i}_j\ldots i_{n-2}lkn}\tilde{\Omega}_{i_1\ldots\hat{i}_j\ldots i_{n-2}}x_l \\ &= \epsilon_{i_1\ldots i_{n-3}lkn}\tilde{\Omega}_{i_1\ldots i_{n-3}}x_l. \end{aligned} \qquad (21)$$

It follows from (21) that $v_n = 0$ for all the body's points. Moreover, the mechanical essence of the tensor $\tilde{\mathbf{\Omega}}^{\{n-3\}}$ now becomes clear. Since the extreme left and right sides of the series of equalities (21) actually form the generalized Euler formula (5) in $\mathbb{R}^{n-1}$, the quantity $\tilde{\mathbf{\Omega}}^{\{n-3\}}$ is the angular-velocity tensor of a solid body describing the rotation in the hyperplane π_n.

The rotation about the axis x_n in $\mathbb{R}^N$ is specified in terms of dual angular velocity $\boldsymbol{\omega}^{\{2\}}$ in a form much more compact than (20):

$$\omega_{nl} = 0, \quad l = 1, 2, \ldots, n. \qquad (22)$$

4. We define in $\mathbb{R}^n$ the momentum vector $\mathbf{Q} = Q_k\mathbf{e}_k$, the angular-momentum tensor $\mathbf{K}^{\{n-2\}} = K_{i_1\ldots i_{n-2}}\mathbf{e}_{i_1} \otimes \ldots \otimes \mathbf{e}_{i_{n-2}}$, the angular-momentum dual tensor $\mathbf{k}^{\{2\}} = k_{ij}\mathbf{e}_i \otimes \mathbf{e}_j$, and the kinetic energy T:

$$\begin{aligned} Q_k &= \int_{V_t}\rho v_k dV = \epsilon_{i_1\ldots i_{n-2}lk}\Omega_{i_1\ldots i_{n-2}}\int_{V_t}\rho x_l dV \\ &= \omega_{lk}\int_{V_t}\rho x_l dV = M\epsilon_{i_1\ldots i_{n-2}lk}\Omega_{i_1\ldots i_{n-2}}x_l^{(c)} = M\omega_{lk}x_l^{(c)}, \end{aligned} \qquad (23)$$

$$\begin{aligned} K_{i_1\ldots i_{n-2}} &= \delta^{j_1\ldots j_{n-2}ml}_{i_1\ldots i_{n-2}kl}\Omega_{j_1\ldots j_{n-2}}\int_{V_t}\rho x_k x_m dV \\ &\equiv I^{j_1\ldots j_{n-2}}_{i_1\ldots i_{n-2}}\Omega_{j_1\ldots j_{n-2}}, \end{aligned} \qquad (24)$$

$$k_{ij} = (n-2)!\int_{V_t}\rho(\omega_{mj}x_i - \omega_{mi}x_j)x_m dV, \qquad (25)$$

$$\begin{aligned} T &= \frac{1}{2}\int_{V_t}\rho|\mathbf{v}|^2 dV = \frac{1}{2}\delta^{j_1\ldots j_{n-2}ml}_{i_1\ldots i_{n-2}kl}\Omega_{j_1\ldots j_{n-2}}\Omega_{i_1\ldots i_{n-2}} \\ &\times\int_{V_t}\rho x_k x_m dV = \frac{1}{2}\omega_{ml}\omega_{kl}\int_{V_t}\rho x_k x_m dV \\ &= -\frac{1}{2}\int_{V_t}\rho\mathbf{r}\cdot\boldsymbol{\omega}^{\{2\}}\cdot\boldsymbol{\omega}^{\{2\}}\cdot\mathbf{r}dV \\ &\equiv \frac{1}{2}I^{j_1\ldots j_{n-2}}_{i_1\ldots i_{n-2}}\Omega_{j_1\ldots j_{n-2}}\Omega_{i_1\ldots i_{n-2}}. \end{aligned} \qquad (26)$$

Here, $\rho(\mathbf{r})$ is the density (its dimension is ML^{-n}) of the n-dimensional body; M is the body's mass; and $\mathbf{I}^{\{2n-4\}} = I^{j_1\ldots j_{n-2}}_{i_1\ldots i_{n-2}}\mathbf{e}_{i_1}\otimes\ldots\otimes\mathbf{e}_{i_{n-2}}\otimes\mathbf{e}_{j_1}\otimes\ldots\otimes\mathbf{e}_{j_{n-2}}$ is the inertia tensor of the rank $2n-4$ with the components

$$I^{j_1\ldots j_{n-2}}_{i_1\ldots i_{n-2}} = \delta^{j_1\ldots j_{n-2}ml}_{i_1\ldots i_{n-2}kl}\int_{V_t}\rho x_k x_m dV. \qquad (27)$$

Hence, the definitions for $\mathbf{K}^{\{n-2\}}$ and T take the form conventional in classical mechanics:

$$\begin{aligned} \mathbf{K}^{\{n-2\}} &= \mathbf{I}^{\{2n-4\}}\odot\mathbf{\Omega}^{\{n-2\}}, \\ T &= \frac{1}{2}\mathbf{\Omega}^{\{n-2\}}\odot\mathbf{I}^{\{2n-4\}}\odot\mathbf{\Omega}^{\{n-2\}}. \end{aligned} \qquad (28)$$

Here, the symbols $\odot$ stand for the convolution with respect to $n-2$ indices.

Using formula (4), we can prove that the convolutions with respect to $n-2$ indices in (24) and with respect to $2n-4$ indices in (26) are

$$\begin{aligned} &K_{i_1\ldots i_{n-2}} \\ &= (n-2)!\int_{V_t}\rho\left(r^2\Omega_{i_1\ldots i_{n-2}} - x_l\sum_{k=1}^{n-2}x_{i_k}\Omega_{i_1\ldots i_{k-1}li_{k+1}\ldots i_{n-2}}\right)dV, \end{aligned} \qquad (29)$$

$$\begin{aligned} T &= \frac{(n-2)!}{2}\int_{V_t}\rho(r^2\Omega_{i_1\ldots i_{n-2}}\Omega_{i_1\ldots i_{n-2}} \\ &- (n-2)x_k x_l\Omega_{i_1\ldots i_{n-3}k}\Omega_{i_1\ldots i_{n-3}l})dV. \end{aligned} \qquad (30)$$

Thus, the mass geometry of an n-dimensional body is specified by the symmetric inertia tensor $\mathbf{J}^{\{2\}} = J_{ij}\mathbf{e}_i\otimes\mathbf{e}_j$

of only the second rank (the natural tensor of the moment of inertia) such that

$$J_{ij} = (n-2)!\int_{V_t}\rho(r^2\delta_{ij}-(n-2)x_ix_j)dV, \qquad (31)$$

$$K_{i_1\ldots i_{n-2}} = \frac{1}{n-2}\sum_{k=1}^{n-2} J_{i_kl}\Omega_{i_1\ldots i_{k-1}li_{k+1}\ldots i_{n-2}}, \quad n\geq 3, \qquad (32)$$

$$T = \frac{1}{2}J_{kl}\Omega_{i_1\ldots i_{n-3}k}\Omega_{i_1\ldots i_{n-3}l}, \quad n\geq 3. \qquad (33)$$

In the case of $n = 2$, the standard relationships in $\mathbb{R}^2$ [instead of (32) and (33)] follow from (29) and (30): $K = J_O\Omega$ and $T = \frac{J_O\Omega^2}{2}$, where $J_O = \int\rho(x_1^2 + x_2^2)dV$. For $n = 3$, the tensors $\mathbf{I}^{\{2\}}$ and $\mathbf{J}^{\{2\}}$ are identical and are reduced to a conventional inertia tensor in $\mathbb{R}^3$.

REFERENCES

1. B. E. Pobedrya, *Lectures on Tensor Analysis* (Mosk. Gos. Univ., Moscow, 1986).
2. O. I. Bogoyavlenskiĭ, Dokl. Akad. Nauk SSSR **287**, 1105 (1986) [Sov. Phys. Dokl. **31**, 309 (1986)].
3. O. I. Bogoyavlenskiĭ, Dokl. Akad. Nauk SSSR **272**, 1364 (1983) [Sov. Phys. Dokl. **28**, 858 (1983)].
4. V. V. Trofimov and A. T. Fomenko, Itogi Nauki Tekh., Ser. Sovrem. Probl. Mat. Noveĭshie Dostizh. **29**, 3 (1986).
5. M. V. Shamolin, Dokl. Akad. Nauk **364**, 627 (1999) [Dokl. Phys. **44**, 110 (1999)].
6. M. V. Shamolin, Dokl. Akad. Nauk **375**, 343 (2000) [Dokl. Phys. **45**, 632 (2000)].

Translated by V. Chechin

Doklady Physics, Vol. 46, No. 9, 2001, pp. 667–671. Translated from Doklady Akademii Nauk, Vol. 380, No. 1, 2001, pp. 51–55.

MECHANICS

Generation of Periodic Internal Waves by an Oscillating Strip of Finite Width

Yu. V. Kistovich and Yu. D. Chashechkin

Presented by Academician A.Yu. Ishlinskiĭ March 26, 2001

Received March 27, 2001

The traditional approach to the calculation of internal-wave generation, which is based on the use of force and mass sources with parameters adopted from the homogeneous-liquid theory, enables one to determine a far field accurate to empirical constants [1–3]. A method for constructing the solutions to a linearized problem that exactly satisfy boundary conditions, was proposed in [4, 5]. As a wave source, part of an infinite plane positioned at an arbitrary angle φ to the horizontal and executing periodic oscillations with a frequency ω was considered. A finite-width strip oscillating along its surface emits unimodular and bimodal beams into a liquid of a constant buoyancy frequency N; the beams travel at the angle $\theta = \arcsin\frac{\omega}{N}$ to the horizontal. In an arbitrary case ($\varphi \neq \theta$), when all beams separate from the emitting surface, the wave pattern and particle-displacement amplitudes are consistent with the measurements [6, 7]. In the critical case ($\varphi = \theta$), when two wave beams propagate along a plane separating the liquid, the calculations result in overstated values of the separated-beam amplitudes and give no way of finding adjacent-beam parameters [5, 7]. The critical-angle case is of particular interest for problems of geophysical hydrodynamics [8] and calls for special consideration.

In the present paper, a solution to the more physically-based problem of internal-wave generation by a finite-width oscillating strip is constructed for the entire range of variation of the strip slope including the critical one.

A system of two-dimensional equations of motion for an exponentially stratified incompressible liquid in the Boussinesq approximation [1] is brought to the following equation for the stream function Ψ in the emitting-surface axes coordinate system (ξ, ζ) (see figure):

$$\left[\omega^2\Delta - N^2\left(\cos\varphi\frac{\partial}{\partial\xi} - \sin\varphi\frac{\partial}{\partial\zeta}\right)^2 - i\omega\nu\Delta^2\right]\Psi(\xi, \zeta) = 0. \quad (1)$$

Here, $\Delta = \frac{\partial^2}{\partial\xi^2} + \frac{\partial^2}{\partial\zeta^2}$ and ν is the kinematic viscosity. The gravity g is opposite to the z-axis; the relation between the coordinate systems (x, z) and (ξ, ζ) is shown in figure.

The adhesion conditions at the emitting surface (which is a strip with a width a inclined at an angle φ and executing oscillations along its surface) and the damping of all perturbations at infinity constitute the boundary conditions for the velocity $u_\xi = \frac{\partial\Psi}{\partial\zeta}$, $u_\zeta = -\frac{\partial\Psi}{\partial\xi}$. The components of the surface velocity (U_ξ, U_ζ) are specified by the relations

$$U_\xi(\xi) = u_0\vartheta\left(\frac{a}{2} - |\xi|\right), \quad U_\zeta(\xi) = 0, \quad (2)$$

where ϑ is the Heaviside unit function. In what follows, the common time-dependent factor $\exp(-i\omega t)$ is omit-

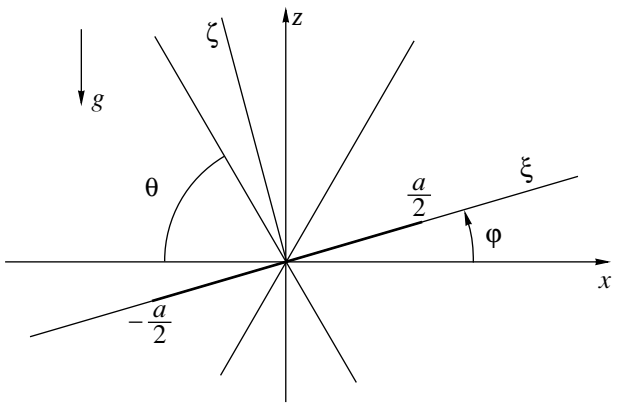

The problem geometry.

Institute of Problems of Mechanics,
Russian Academy of Sciences,
pr. Vernadskogo 101, Moscow, 117526 Russia

1028-3358/01/4609-0667$21.00

ted everywhere. As a result, the boundary conditions for the stream function Ψ on the plate take the form

$$\left.\frac{\partial\Psi}{\partial\zeta}\right|_{\zeta=0} = U_\xi(\xi), \quad \left.\frac{\partial\Psi}{\partial\xi}\right|_{\zeta=0} = -U_\xi(\xi). \qquad (3)$$

They are supplemented with the continuity conditions for Ψ and for all its derivatives with respect to ζ up to and including the third one for $\zeta = 0, |\xi| > \frac{a}{2}$; and with the damping conditions at infinity: $\Psi(\xi, \zeta) \longrightarrow 0$ for ξ, $\zeta \longrightarrow \pm\infty$.

The solution is found by the method of integral transformations. In this way, the stream function of the emitted field is represented in the form [4]

$$\Psi(\xi, \zeta) = \int_{-\infty}^{+\infty}\left(be^{i\kappa_w^+\zeta} + ce^{i\kappa_b^+\zeta}\right)e^{ik\xi}dk, \quad \zeta > 0. \qquad (4)$$

Here, $b(k)$ and $c(k)$ are spectral densities; the wave numbers $\kappa_w^\pm(k)$ and $\kappa_b^\pm(k)$, which correspond to traveling internal waves and internal boundary layers, are roots of the dispersion equation [5]

$$\begin{aligned}\omega^2(\kappa^2 + k^2) - N^2(\kappa\sin\varphi - k\cos\varphi)^2 \\ + i\nu\omega(\kappa^2 + k^2)^2 = 0.\end{aligned} \qquad (5)$$

To meet the damping conditions at infinity, branches are chosen such that

$$\mathrm{Im}\kappa_w^+ > 0, \quad \mathrm{Im}\kappa_b^+ > 0, \quad \mathrm{Im}\kappa_w^- < 0, \quad \mathrm{Im}\kappa_b^- < 0.$$

The solution to Eq. (1) with the foregoing boundary conditions is constructed by the method of successive approximations. At the beginning, following the procedure described in [3, 4], a solution $\Psi_0^{(1)}$ is constructed with boundary conditions (3) and the additional conditions $u_\xi = u_\zeta = 0$ for $\zeta = 0, |\xi| > \frac{a}{2}$, which describe perturbations excited by the motion of a part of the infinite plane. The solution $\Psi_0^{(1)}$ does not satisfy the conditions of continuity for all its derivatives with respect to ζ outside the strip. A correction $\Psi_0^{(2)}$ satisfying Eq. (1) and providing the continuity of the sum $\Psi_0^{(1)} + \Psi_0^{(2)}$ and its derivatives up to the third one for $\zeta = 0, |\xi| > \frac{a}{2}$ is added to $\Psi_1^{(0)}$. The sum obtained ceases to satisfy the boundary conditions (3). To satisfy these conditions on the strip, which is a part of the infinite motionless plane, a function $\Psi_1^{(1)}$ is added to the solution. The addition of a function $\Psi_1^{(2)}$ ensures the continuity of the sum $\Psi_1^{(1)} + \Psi_1^{(2)}$ and its derivatives up to and including the third one outside the plate. Each of the correction functions satisfies Eq. (1). Unrestricted repetition of the iterative procedure allows for the representation of the exact solution to the problem in the form

$$\Psi(\xi, \zeta) = \sum_{n=0}^{\infty}\Psi_n(\xi, \zeta), \quad \Psi_n = \Psi_n^{(1)} + \Psi_n^{(2)}. \qquad (6)$$

Substitution of (6) into the boundary conditions of the problem results in the following relations:

$$\begin{aligned}&\Psi_n^{(2)}\big|_{\zeta=+0} = \Psi_n^{(2)}\big|_{\xi=-0}, \quad \Psi_{n\zeta}^{(2)}\big|_{\zeta=+0} = \Psi_{n\zeta}^{(2)}\big|_{\zeta=-0}, \\ &\Psi_{n\zeta\zeta}^{(2)}\big|_{\zeta=+0} - \Psi_{n\zeta\zeta}^{(2)}\big|_{\zeta=-0} \\ &= \vartheta\left(|\xi| - \frac{a}{2}\right)\left[\Psi_{n\zeta\zeta}^{(1)}\big|_{\zeta=-0} - \Psi_{n\zeta\zeta}^{(1)}\big|_{\zeta=+0}\right], \\ &\Psi_{n\zeta\zeta\zeta}^{(2)}\big|_{\zeta=+0} - \Psi_{n\zeta\zeta\zeta}^{(2)}\big|_{\zeta=-0} \\ &= \vartheta\left(|\xi| - \frac{a}{2}\right)\left[\Psi_{n\zeta\zeta\zeta}^{(1)}\big|_{\zeta=-0} - \Psi_{n\zeta\zeta\zeta}^{(1)}\big|_{\zeta=+0}\right], \\ &\Psi_{n+1}^{(1)}\big|_{\zeta=\pm0} = 0, \\ &\Psi_{n+1,\zeta}^{(1)}\big|_{\zeta=\pm0} = -\vartheta\left(\frac{a}{2} - |\xi|\right)\Psi_{n\zeta}^{(2)}\big|_{\zeta=\pm0}, \\ &\Psi_0^{(1)}\big|_{\zeta=\pm0} = 0, \quad \Psi_{0\zeta}^{(1)}\big|_{\zeta=\pm0} = u_0\vartheta\left(\frac{a}{2} - |\xi|\right).\end{aligned} \qquad (7)$$

Here, each of the indices ζ in $\Psi_n^{(1,2)}$ denotes differentiation with respect to ζ.

Both iterations and the complete solution (4) are sought in the form

$$\begin{aligned}\Psi_n^{(1)} &= \int_{-\infty}^{+\infty}\left[\vartheta(\zeta)A_n^+\left(e^{i\kappa_w^+\zeta} - e^{i\kappa_b^+\zeta}\right)\right. \\ &\left. + \vartheta(-\zeta)A_n^-\left(e^{i\kappa_w^-\zeta} - e^{i\kappa_b^-\zeta}\right)\right]e^{ik\xi}dk, \\ \Psi_n^{(2)} &= \int_{-\infty}^{+\infty}\left[\vartheta(\zeta)\left(B_n^+e^{i\kappa_w^+\zeta} + C_n^+e^{i\kappa_b^+\zeta}\right)\right. \\ &\left. + \vartheta(-\zeta)\left(B_n^-e^{i\kappa_w^-\zeta} + C_n^-e^{i\kappa_b^-\zeta}\right)\right]e^{ik\xi}dk.\end{aligned} \qquad (8)$$

Substitution of (8) into (7) results in the following system of equations:

$$(\kappa_w^+ - \kappa_b^+)A_0^+ = (\kappa_w^- - \kappa_b^-)A_0^- = -\frac{iu_0}{\pi k}\sin\frac{ka}{2} \equiv A_0(k),$$

$$A_{n+1}(k) \equiv (\kappa_w^+ - \kappa_b^+)A_{n+1}^+ = (\kappa_w^- - \kappa_b^-)A_{n+1}^-$$
$$= -\frac{1}{\pi}\int_{-\infty}^{+\infty} \frac{\kappa_w^+(k')B_n^+(k') + \kappa_b^+(k')C_n^+(k')}{k'-k}\sin\frac{(k'-k)a}{2}dk',$$

$$B_n^+ + C_n^+ - B_n^- - C_n^- = 0, \quad (9)$$
$$\kappa_w^+ B_n^+ + \kappa_b^+ C_n^+ - \kappa_w^- B_n^- - \kappa_b^- C_n^- = 0,$$
$$\kappa_w^{+2} B_n^+ + \kappa_b^{+2} C_n^+ - \kappa_w^{-2} B_n^- - \kappa_b^{-2} C_n^- = -D_1 A_n + I_1,$$
$$\kappa_w^{+3} B_n^+ + \kappa_b^{+3} C_n^+ - \kappa_w^{-3} B_n^- - \kappa_b^{-3} C_n^- = -D_2 A_n + I_2.$$

Here,

$$I_j = \frac{1}{\pi}\int_{-\infty}^{+\infty} \frac{D_j(k')A_n(k')}{k'-k}\sin\frac{(k'-k)a}{2}dk',$$

$$D_1 = \kappa_w^+ + \kappa_b^+ - \kappa_w^- - \kappa_b^-, \quad (10)$$

$$D_2 = \kappa_w^{+2} + \kappa_w^+\kappa_b^+ + \kappa_b^{+2} - \kappa_w^{-2} + \kappa_w^-\kappa_b^- + \kappa_b^{-2}.$$

By solving system (9), substituting the result into (8) and (6), and comparing it with (4), we arrive at the spectral densities for the wave component $b(k)$ and the boundary-layer component $c(k)$ of motion:

$$b(k) = \frac{1}{\pi}\int_{-\infty}^{+\infty} R_b(k, k')g(k')dk',$$
$$c(k) = \frac{1}{\pi}\int_{-\infty}^{+\infty} R_c(k, k')g(k')dk'. \quad (11)$$

Here,

$$R_b(k, k') = \frac{D_2(k') + \kappa_w^+ D_1(k')}{(\kappa_w^+ - \kappa_w^-)(\kappa_w^+ - \kappa_b^+)(\kappa_w^+ - \kappa_b^-)},$$
$$R_c(k, k') = \frac{D_2(k') + \kappa_b^+ D_1(k')}{(\kappa_b^+ - \kappa_b^-)(\kappa_b^+ - \kappa_w^+)(\kappa_b^+ - \kappa_w^-)}. \quad (12)$$

All $\kappa_w^\pm$ and $\kappa_b^\pm$ in (12) are functions of k and k'-independent; in (11), the function $g(k)$ is a solution to the integral equation

$$g(k) - \frac{1}{\pi}\int_{-\infty}^{+\infty} R(k, k')g(k')dk' = -\frac{iu_0}{\pi k}\sin\frac{ka}{2} \quad (13)$$

with the kernel

$$R(k, k') = \frac{1}{k'-k}\sin\frac{(k'-k)a}{2} + \frac{1}{\pi}\int_{-\infty}^{+\infty}\sin\frac{(k''-k)a}{2}$$
$$\times \sin\frac{(k''-k')a}{2}\frac{D_3(k'')D_2(k') - D_4(k'')D_1(k')}{(k''-k)(k''-k')D_0(k'')}dk''. \quad (14)$$

Here,

$$D_0 = (\kappa_w^+ - \kappa_w^-)(\kappa_w^+ - \kappa_b^-)(\kappa_b^+ - \kappa_w^-)(\kappa_b^+ - \kappa_b^-),$$
$$D_3 = \kappa_w^+\kappa_b^+ - \kappa_w^-\kappa_b^-, \quad (15)$$
$$D_4 = \kappa_w^+\kappa_b^+(\kappa_w^+ + \kappa_b^+) - \kappa_w^-\kappa_b^-(\kappa_w^- + \kappa_b^-),$$

and D_1 and D_2 are defined in (10). The calculations of the stream function performed for $\zeta < 0$ show that the field possesses central symmetry: $\Psi(-\xi, -\zeta) = \Psi(\xi, \zeta)$.

Since in what follows we employ approximate solutions to dispersion equation (5), cases of a general position of the strip ($\varphi \neq \pm\theta$) and of the critical angle ($\varphi = \theta$) call for separate considerations.

In the general case, approximate expressions for roots of dispersion equation (5) are of the form

$$\kappa_w^\pm(k) = \mp|k|\cot(\theta \mp \lambda\varphi) \pm \frac{i\nu|k|^3}{2N\cos\theta\sin^4(\theta \mp \lambda\varphi)},$$
$$\lambda = \operatorname{sgn} k,$$
$$\kappa_b^\pm(k) = \pm k_b - \frac{k\sin\varphi\cos\varphi}{\sin^2\varphi - \sin^2\theta}, \quad (16)$$
$$k_b = [i + \operatorname{sgn}(\sin^2\varphi - \sin^2\theta)]\sqrt{\frac{N|\sin^2\varphi - \sin^2\theta|}{2\nu\sin\theta}}.$$

Substituting (16) into (12) and (14), we obtain approximate expressions for the kernels R, R_b, and R_c:

$$R(k, k') = \frac{1}{\pi k_b\sin\theta\cos\theta(\sin^2\varphi - \sin^2\theta)}$$
$$\times \int_{-\infty}^{+\infty}\sin\frac{(k''-k)a}{2}\sin\frac{(k''-k')a}{2} \quad (17)$$
$$\times \frac{\operatorname{sgn} k''(k''-k')\sin^2\varphi\cos^2\varphi + (|k''| - |k'|)\sin^2\theta\cos^2\theta}{(k''-k)(k''-k')}dk'',$$

$$R_b(k, k') = -\frac{1}{k_b}\left[\frac{1}{k'-k} - \frac{\sin 2\varphi}{|k|\sin 2\theta}\right]\sin\frac{(k'-k)a}{2}, \quad (18)$$

$$R_c(k, k') = \frac{1}{k_b(k'-k)}\sin\frac{(k'-k)a}{2}. \quad (19)$$

In the low-viscosity approximation for $\nu \longrightarrow 0$, kernel (17) of the integral equation (13) also tends to zero, and in the first approximation solution (13) is of the form

$$g(k) = -\frac{iu_0}{\pi k}\sin\frac{ka}{2}. \quad (20)$$

Substituting (20) and kernels (17), (18) into (11), we obtain the spectral densities of the internal waves and

the boundary layer:

$$b(k) = \frac{iu_0}{\pi k_b}\left[\frac{1}{k} + \frac{1}{2|k|}\frac{\sin 2\varphi}{\sin 2\theta}\right]\sin\frac{ka}{2},$$
$$c(k) = -\frac{iu_0}{\pi k_b k}\sin\frac{ka}{2}. \quad (21)$$

In comparing (21) with the formulas given in paper [5], it follows that only the expression for the wave field changes in the more adequate formulation (in the absence of the infinite motionless plane). The result obtained in [5, 7] for the internal boundary layer remains unchanged. It follows from (21) that the spatial structures of beams emitted by an isolated strip and a moving part of the infinite plane are the same, and the amplitudes differ by the factor $\left(1 \pm \frac{\sin 2\varphi}{2\sin 2\theta}\right)$.

In the critical case, roots of dispersion equation (5) are of the form:

$$\kappa_w^+ = \vartheta(k)\left[\frac{i-\sqrt{3}}{2}\gamma - \frac{k\cot 2\theta}{3}\right] + \vartheta(-k)k\cot 2\theta,$$
$$\kappa_w^- = \vartheta(k)k\cot 2\theta + \vartheta(-k)\left[\frac{\sqrt{3}-i}{2}\gamma - \frac{k\cot 2\theta}{3}\right],$$
$$\kappa_b^+ = \vartheta(k)\left[\frac{\sqrt{3}+i}{2}\gamma - \frac{k\cot 2\theta}{3}\right] + \vartheta(-k)\left[i\gamma - \frac{k\cot 2\theta}{3}\right], \quad (22)$$
$$\kappa_b^- = -\vartheta(k)\left[i\gamma + \frac{k\cot 2\theta}{3}\right] - \vartheta(-k)\left[\frac{\sqrt{3}+i}{2}\gamma + \frac{k\cot 2\theta}{3}\right],$$
$$\gamma = \sqrt[3]{\frac{2|k|N\cos\theta}{\nu}}.$$

Substituting (22) into (14), we obtain

$$g(k) = -\frac{iu_0 a}{2\pi}F\left(\frac{ka}{2}\right), \quad (23)$$

where the universal function $F(x)$ is the solution to the integral equation

$$F(x) - \frac{1}{\pi}\int_{-\infty}^{+\infty}\left[\frac{\sin(x'-x)}{x'-x} - \frac{1}{3\pi}\int_{-\infty}^{+\infty}\frac{\mathrm{sgn}(x'x'')}{(x''-x')(x''-x)}\sqrt[3]{\frac{x'}{x''}}\right.$$
$$\left.\times\left(2 + \sqrt[3]{\frac{x'}{x''}}\right)\sin(x''-x')\sin(x''-x)dx''\right]F(x')dx' = \frac{\sin x}{x}. \quad (24)$$

The kernels R_b and R_c are of the form

$$R_b(k, k') = -\frac{i}{3|k|(k'-k)}\sqrt[3]{\frac{\nu k'|k'|}{2N\cos\theta}}$$
$$\times\left\{3\vartheta(-k) + \vartheta(k)\left[1 - (1+i\sqrt{3})\sqrt[3]{\frac{k}{k'}}\right]\right\}\sin\frac{(k'-k)a}{2},$$
$$R_c(k, k') = -\frac{i}{3|k|(k'-k)}\sqrt[3]{\frac{\nu k'|k'|}{2N\cos\theta}}$$
$$\times\left\{\vartheta(-k)\left[1 - 2\sqrt[3]{\frac{|k|}{k'}}\right]\right.$$
$$\left.+ \vartheta(k)\left[1 - (1-i\sqrt{3})\sqrt[3]{\frac{k}{k'}}\right]\right\}\sin\frac{(k'-k)a}{2}. \quad (25)$$

The equation for $F(x)$ does not contain medium parameters or source characteristics, which appear only after transformations (11) with kernels (25) have been applied to the function $g(k)$. In the critical case, the coordinate system (ξ, ζ) becomes the comoving reference frame for two beams propagating along the oscillation plane. With allowance made for these properties, the expression for the stream function in the region $\xi > \frac{a}{2}$ can be found immediately without solving equation (24):

$$\Psi = -\frac{i\beta u_0}{\pi^2}\sqrt[3]{\frac{\nu^2 a^2}{2N^2\cos^2\theta}}\int_0^\infty \exp\left[-ik\zeta - \frac{\nu k^3\xi}{2N\cos\vartheta}\right]dk. \quad (26)$$

Here, the universal coefficient of the problem

$$\beta = \int_{-\infty}^{+\infty}\frac{\sin x}{\sqrt[3]{x|x|}}F(x)dx. \quad (27)$$

From a comparison of (26) with the results of [1, 3, 7] it follows that the beam propagating along the plate is always unimodular in the critical case. The vertical-displacement amplitude on its axis is determined by the formula

$$h(\xi, 0) = \frac{\beta b\sin\theta}{3\pi^2}\Gamma\left(\frac{2}{3}\right)\sqrt[3]{\frac{2a^2}{\xi^2}}, \quad (28)$$

where $b = \frac{u_0}{\omega}$ is the plate-oscillation amplitude. Thus, employing the correct solutions (22) to the dispersion equation (5) solves the problem of critical angles in the generation problem as well as in the problem of reflection of internal waves from a rigid surface in a viscous, continuously stratified liquid [9].

In a three-dimensional case, the boundary layer has a more complex nature and includes both the periodic

Stokes flow, whose parameters do not depend on the presence of stratification, and an internal boundary layer, which is specific for a given geometry [10]. A separated boundary layer forms a fine structure of a medium at the source horizon [6]. Nonlinear interaction between internal boundary layers and internal waves may serve as an additional mechanism in wave generation [11].

REFERENCES

1. M. J. Lighthill, *Waves in Fluids* (Cambridge Univ. Press, Cambridge, 1978; Mir, Moscow, 1981).
2. V. P. Dokuchaev and I. S. Dolina, Izv. Akad. Nauk SSSR, Fiz. Atmos. Okeana **13**, 655 (1977).
3. S. A. Makarov, V. I. Neklyudov, and Yu. D. Chashechkin, Izv. Akad. Nauk SSSR, Fiz. Atmos. Okeana **26**, 744 (1990).
4. Yu. D. Chashechkin and Yu. V. Kistovich, Dokl. Akad. Nauk **355**, 54 (1997) [Phys. Dokl. **42**, 377 (1997)].
5. Yu. V. Kistovich and Yu. D. Chashechkin, Prikl. Mekh. Tekh. Fiz. **40**, 31 (1999).
6. Yu. S. Il'inykh, Yu. V. Kistovich, and Yu. D. Chashechkin, Izv. Akad. Nauk, Fiz. Atmos. Okeana **35**, 649 (1999).
7. Yu. D. Chashechkin, Yu. V. Kistovich, and S. A. Smirnov, Environmetrics **12**, 57 (2000).
8. C. C. Ericsen, in *Proceedings of the "Aha Huliko" Hawaiian Winter Workshop, University of Hawaii, Manoa, 1984*, p. 183.
9. Yu. V. Kistovich and Yu. D. Chashechkin, Prikl. Mat. Mekh. **59**, 607 (1995).
10. Yu. V. Kistovich and Yu. D. Chashechkin, Prepr. No. 674, IPM RAN (Institute of Problems of Mechanics, Russian Academy of Sciences, Moscow, 2001).
11. Yu. V. Kistovich and Yu. D. Chashechkin, Dokl. Akad. Nauk **367**, 636 (1999) [Dokl. Phys. **44**, 573 (1999)].

Translated by V. Tsarev

Doklady Physics, Vol. 46, No. 9, 2001, pp. 672–674. Translated from Doklady Akademii Nauk, Vol. 380, No. 1, 2001, pp. 56–59.

MECHANICS

A Unique Criterion for the Fatigue Fracture of Metallic Materials

A. N. Romanov

Presented by Academician R.F. Ganiev March 6, 2001

Received March 30, 2001

Over many decades, resistance properties of structural materials with respect to deformation and fracture under cyclic loading have been studied. Investigations aimed at the development of fracture criteria necessary for estimating the strength of machines, equipment, and structures of various application have also been performed. In these studies, force, deformation, and energy approaches were widely used. Each of these approaches now has dozens of proposals related to various criteria [1]. It should be noted that, as a rule, the existing criteria are reduced to equations of a fatigue curve for a given material and given loading conditions and, therefore, cannot be extended to other materials and testing conditions. In addition, these criteria are related to a limited number of materials and loading conditions that, as before, require a large amount of experimental data.

Compared to the other approaches, the energy one is the most general. Numerous studies have demonstrated [2], however, that the energy of cyclic fracture may greatly exceed the energy spent on the single fracture of a sample and, thus, cannot be accepted as a criterion. In the case of cyclic loading, a considerable part of the energy is dissipated in the form of heat and is spent on reversible deformation in the cycles. Only the lesser part of the energy is directly spent on fracturing the material. The experimental determination of this part is extremely difficult [1]. The employment of this quantity for estimating the endurance of structural elements is also hampered.

In [3], a suggestion based on the energy approach is made that in the case of low-cycle loading, the ultimate work p of microscopic stresses (microstresses) in the plastic-deformation path L is the fracture work:

$$\int kp dL = 1. \tag{1}$$

Here, k is a constant determined from the experiment.

Based on the studies of the Bauschinger effect [1] and concepts concerning the role of microdamages in the plastic-deformation path, I succeeded in finding a fracture criterion for the case of cyclic loading within the given loading range in a soft-loading cycle, i.e., in a cycle with a given stress amplitude. In this case, the criterion has the form

$$\int_0^{N_p} \frac{\delta^2}{\varepsilon^2} dN + \int_0^{N_p} \frac{(\delta - \delta')(\varepsilon - \delta)}{\varepsilon^2} dN = 1. \tag{2}$$

Under the condition that, basically, $\delta \ll \varepsilon$, criterion (2) can be written out in the form

$$\int_0^{N_p} \frac{\delta^2}{\varepsilon^2} dN + \int_0^{N_p} \frac{\Delta\varepsilon}{\varepsilon} dN = 1. \tag{3}$$

Here, δ is the plastic deformation (the hysteresis-loop width) in the tension half-cycle; $\delta - \delta' = \Delta\varepsilon$ is the accumulated deformation in the cycle under consideration; δ' is the plastic strain in the compression half-cycle; ε is the material plasticity in the case of the sample single-stage fracture (this quantity provides the material carrying capacity); and N_p is the number of cycles before fracture.

In the case of loading within the given range of elastoplastic deformation in a cycle (rigid loading), the second term in relations (2) and (3) vanishes (the plastic-deformation accumulation does not occur). Then, criterion (3) for the case of rigid loading is written out as

$$\int_0^{N_p} \frac{\delta^2}{\varepsilon^2} dN = 1. \tag{4}$$

The first term in relations (2) and (3) determines the level of damage accumulated as a result of the action of cyclic plastic deformation. The second term corresponds to the damage caused by the accumulated plastic deformation for the number of loading cycles under consideration. The fracture occurs when the damage level attains unity. The relations (3) and (4) make it possible to determine the level of accumulated damage for an arbitrary number (which we are interested in) of loading cycles including programmable loading.

Blagonravov Institute of Engineering Science, Russian Academy of Sciences, Malyĭ Khariton'evskiĭ per. 4, Moscow, 101990 Russia

1028-3358/01/4609-0672$21.00

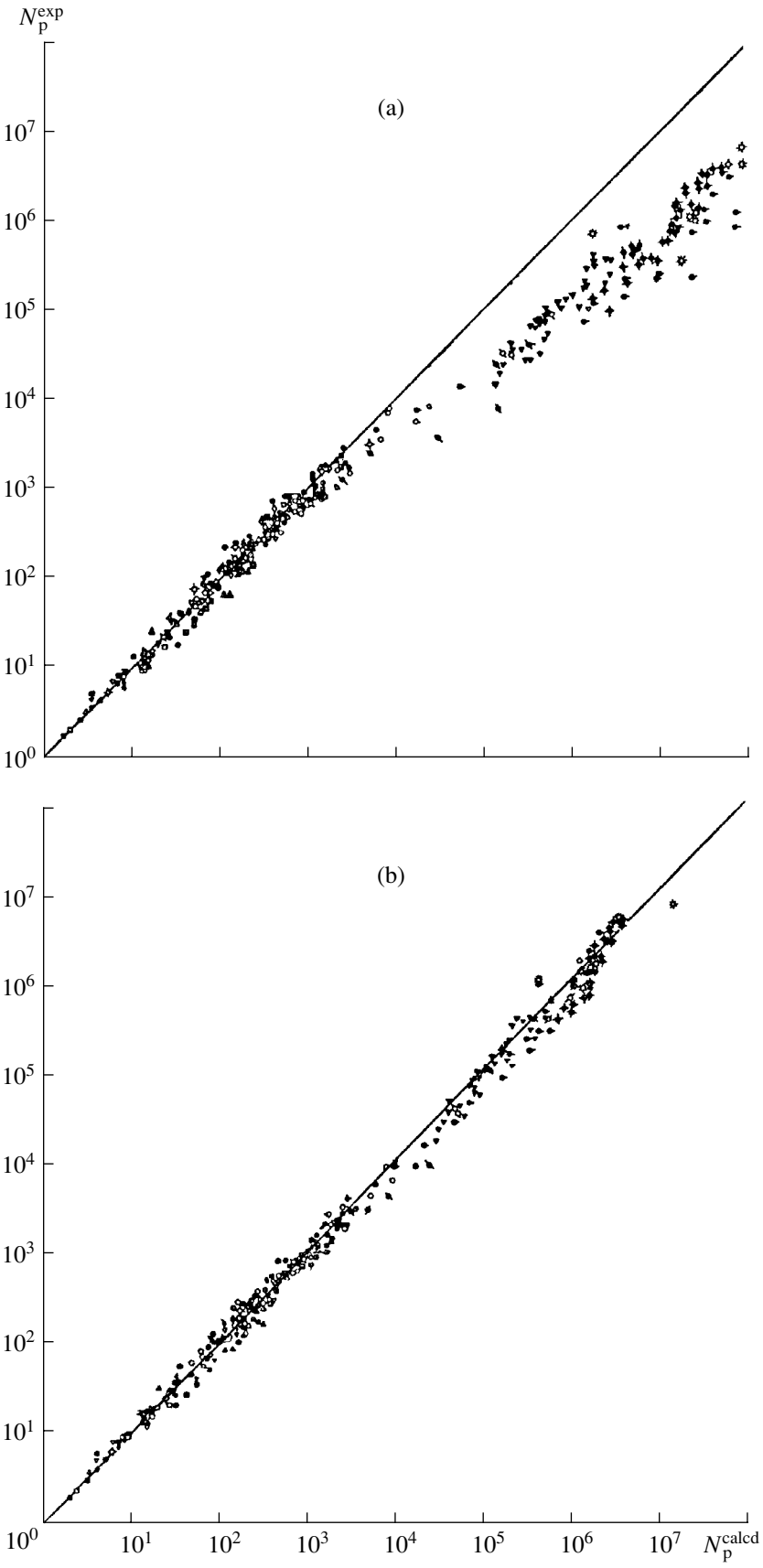
N_p^{exp}
(a)
10^7
10^6
10^5
10^4
10^3
10^2
10^1
10^0
(b)
10^7
10^6
10^5
10^4
10^3
10^2
10^1
10^0
10^1 10^2 10^3 10^4 10^5 10^6 10^7 N_p^{calcd}

Fig. 1.

As experiments show, relations (3) and (4) satisfactorily describe fracture conditions in the region of low-cycle fatigue (Fig. 1a) but do not allow us to describe fracture within the region of a large number of cycles before fracture (more than 10^4 cycles).

The assumption about the damaging role of microstresses also in the path of elastic deformation e_e made it possible to find the fracture criterion in the form

$$\int_0^{N_p} \frac{\delta^2}{\varepsilon^2} dN + \int_0^{N_p} \frac{\Delta\varepsilon}{\varepsilon} dN + \int_0^{N_p} \frac{e_e \delta}{\varepsilon^2} dN = 1. \quad (5)$$

In this relation, the third term determines the level of the accumulated damage caused by the action of elastic deformation $e_e = \frac{\sigma}{E}$.

Criterion (5) can be rewritten as

$$\int_0^{N_p} \frac{\delta e_{ep}}{\varepsilon^2} dN + \int_0^{N_p} \frac{\Delta\varepsilon}{\varepsilon} dN = 1, \quad (6)$$

where $e_{ep} = \delta + e_e$.

In the case of rigid loading, we can assume that δ = const and e_{ep} = const. Then, relation (3) takes the form

$$\frac{de_{ep}}{\varepsilon^2} N_p = 1. \quad (7)$$

The assumptions indicated on the damaging role of microstresses in the path of elastic and plastic deformations made it possible to describe fracture conditions in the entire range of fracturing cyclic loading (i.e., for a different number of fracturing cycles) in both the region of low-cycle and high-cycle fracture (Fig. 1b) by a unique relation (6).

The criterion obtained testifies to the fact that, in the case of cyclic loading, the damage-accumulation process and fracture conditions obey the unique rule (law) independent of loading conditions.

As it was shown previously [1], the ratio $\frac{\delta}{\varepsilon}$ in the low-cycle region before fracture satisfactorily determines the Bauschinger cyclic effect. It may be assumed that the Bauschinger parameter α_e that characterizes fields of residual microstresses can describe the Bauschinger effect in both the low-cycle and high-cycle regions.

Experimental verification of criteria (6) and (7) confirmed the existence of a unique criterion for the fracture of any given metallic material in any given structural state (i.e., independent of the thermal processing form) with arbitrary conditions of cyclic loading (temperature, loading frequency, cycle asymmetry, etc.). In this case, loading conditions affect the characteristics of resistance with respect to deformation, which enter into relationships (6) and (7). However, in accordance with these criteria, the loading conditions do not change the rule (law) of summing damages, including programmable loading (e.g., two-frequency, steplike, overloaded, having time lags in loading half-cycles, etc.).

Criteria (6) and (7) describe the kinetics of damage accumulation, the extreme case of which corresponds to the appearance of a macrocrack.

Numerous criteria of the ultimate failure (survivability criteria) are obtained for describing the stage of the development of such a crack. In contrast to those proposed above, these criteria for describing fracture at the stage preceding the appearance of cracks are not universal.

The extension of the above concept to the stage of crack development make it possible to find criteria for material (structure) survivability in the form

$$\int_0^{N_p} \frac{\nu_{ep}\nu_p}{\nu_c^2} dN + \int_0^{N_p} \frac{\Delta\nu}{\nu_c} dN = 1. \quad (8)$$

Here, ν_p, ν_e, ν_{ep}, and $\Delta\nu$ are the plastic (residual reversible), elastic, and elastoplastic (reversible) displacements of the crack faces in the tension half-cycle and the accumulated crack opening in the cycle, respectively, and ν_c is the ultimate crack opening in the case of a single-stage fracture of a sample with a crack.

When an accumulation of the crack opening does not occur (the case of a rigid loading), the second term in relationship (8) vanishes, and we have

$$\int_0^{N_p} \frac{\nu_{ep}\nu_p}{\nu_c^2} dN = 1. \quad (9)$$

An experimental verification of criteria (8) and (9) has confirmed their validity.

Thus, we can affirm the existence of a unique criterion for fracturing metallic materials in the entire possible time range of loading at the stages of nucleation and the development of cracks (low-cycle and high-cycle fatigue). This criterion is independent of the type, structural state (i.e., thermal processing), form of a loading of a material (single-frequency, double-frequency, asymmetric, having time lags, and programmable), as well as of the loading conditions (temperature and frequency). New approaches that can be applied to both the calculation methods for the cyclic strength and to the rules for the choice of structural materials are proposed.

REFERENCES

1. A. N. Romanov, *Low-cycle Loading Failure* (Nauka, Moscow, 1988).
2. V. S. Ivanova, *Fatigue Fracture of Metals* (Metallurgizdat, Moscow, 1963).
3. V. V. Novozhilov and O. G. Rybakina, in *Proceedings of the III Conference on Mechanical Problems of Fatigue* (IMASh, Moscow, 1966), p. 71.

Translated by G. Merzon

Doklady Physics, Vol. 46, No. 9, 2001, pp. 675–677. Translated from Doklady Akademii Nauk, Vol. 380, No. 2, 2001, pp. 194–196.

MECHANICS

Direct and Inverse Poynting Effects in Elastic Cylinders

L. M. Zubov

Presented by Academician I.I. Vorovich February 22, 2001

Received March 12, 2001

A nonlinear interaction of longitudinal and torsional strains in an elastic cylinder is studied on the basis of the exact theory for the torsion of prismatic bodies subjected to severe strains [1, 2]. Along with the known direct Poynting effect of varying the length of a prismatic body under the action of torque, we treat the inverse Poynting effect, which represents the torsion of a bar under the action of a longitudinal force, provided that the bar has been subjected to a torsional prestrain. For a certain class of isotropic incompressible materials, we draw a qualitative conclusion on the sign of the Poynting effect. A series of identities and inequalities relating the torsional and longitudinal instantaneous rigidities of a bar is found. General statements of the theory developed are illustrated using a circular cylinder made of a non-Hookean material as an example. In this case, using the explicit relationships found for the longitudinal extension and the angle of torsion in terms of the longitudinal force and the torque, we succeed in studying the direct and inverse Poynting effects over a wide range of strains.

1. The torsion and extension–compression of an elastic prismatic (cylindrical) body subjected to finite deformations are described by the relationships [1, 2]

$$X_1 = u_1(x_1, x_2)\cos\psi x_3 - u_2(x_1, x_2)\sin\psi x_3,$$
$$X_2 = u_1(x_1, x_2)\sin\psi x_3 + u_2(x_1, x_2)\cos\psi x_3, \quad (1)$$
$$X_3 = (1 + \delta)x_3 + u_3(x_1, x_2), \quad \psi, \delta = \text{const}.$$

Here, x_k ($k = 1, 2, 3$) are the Cartesian coordinates of the body's points in the undeformed configuration, with the coordinate x_3 measured along the generatrix, i.e., along the axis of the bar. We introduce the notation X_s ($s = 1, 2, 3$) for the Cartesian coordinates of the body's points in the deformed configuration. The constants ψ and δ are the angle of torsion and the longitudinal elongation per unit length of the elastic bar, respectively. The functions u_m ($m = 1, 2, 3$) of the two variables are determined by solving the two-dimensional nonlinear problem formulated in [1, 2].

Rostov State University,
pr. Stachki 194, Rostov-on-Don, 344104 Russia

If the cross section of the cylinder has two axes of symmetry and the bar is made of an isotropic material, then, as was proved in [2], the longitudinal force P and the torque M, both applied to the bar's faces, are given by

$$P(\delta, \psi) = \frac{\partial \Pi}{\partial \delta}, \quad M(\delta, \psi) = \frac{\partial \Pi}{\partial \psi}, \quad (2)$$

$$\Pi(\delta, \psi) = \iint_S W[u_m^0(x_1, x_2, \psi, \delta)]\,dS. \quad (3)$$

Here, W is the specific strain (potential) energy for the elastic material; S is the cross section of the bar in the undeformed configuration; and $\Pi(\delta, \psi)$ is a functional of the specific strain potential energy of the bar (per unit length), which is evaluated for the solution u_m^0 ($m = 1, 2, 3$) to the two-dimensional boundary value problem mentioned above. In what follows, we will assume that the strain potential energy $\Pi(\delta, \psi)$ of the extended and twisted bar is a double differentiable strictly convex function. From the physical standpoint, this assumption implies that the process of extending and twisting the cylinder is stable. As follows from relationships (2), with regard to the strict convexity of the function $\Pi(\delta, \psi)$, the functions $P(\delta, \psi)$ and $M(\delta, \psi)$ are strictly reversible in the range of stable strains. In this case, the relationships

$$\delta(P, M) = \frac{\partial K}{\partial P}, \quad \psi(P, M) = \frac{\partial K}{\partial M}, \quad K(P, M) = P\delta + M\psi - \Pi \quad (4)$$

are satisfied, where $K(P, M)$ is a strictly convex function describing the additional energy of the bar related to the function $\Pi(\delta, \psi)$ by the Legandre transform. It is worth noting that $\Pi(\delta, \psi)$ and $K(P, M)$ are even functions of the variables ψ and M, respectively.

2. Let the longitudinal force P and torque M be applied to the faces of an elastic bar. We now consider small tensile and torsional strains caused by the load increments ΔP and ΔM. Using (4), we obtain

$$\Delta\delta = \frac{\partial \delta}{\partial P}\Delta P + \frac{\partial \delta}{\partial M}\Delta M, \quad \Delta\psi = \frac{\partial \psi}{\partial P}\Delta P + \frac{\partial \psi}{\partial M}\Delta M. \quad (5)$$

1028-3358/01/4609-0675$21.00

According to (5), the derivatives $\frac{\partial\delta}{\partial M}$ and $\frac{\partial\psi}{\partial P}$ define the direct and inverse Poynting effects [3–5] (i.e., the variations of the length or the angular twist of a bar, which are caused, respectively, by increments of the torque or the longitudinal force). The equality $\frac{\partial\delta}{\partial M} = \frac{\partial\psi}{\partial P}$ following from (4) implies that if the length of a bar subjected to a constant force P increases with the torque then the angular twist of such a bar subjected to a constant torque will increase with the extra tensile force.

Since the specific elongation δ is an even function of M, the derivatives $\frac{\partial\delta}{\partial M}$ and $\frac{\partial\psi}{\partial P}$ vanish at $M = 0$. To analyze the direct and inverse Poynting effects for small values of M, we approximate the functions $\delta(P, M)$ and $\psi(P, M)$ by the following partial sums of the Taylor series:

$$\begin{aligned}\delta &= \delta_0(P) + \delta_2(P)M^2 + O(M^4),\\ \psi &= \psi_1(P)M + O(M^3).\end{aligned} \tag{6}$$

It follows from (4) and (6) that

$$2\delta_2(P) = \frac{d\psi_1}{dP}. \tag{7}$$

If the force P has an increment ΔP, then Eq. (6) with a constant torque M yields

$$\Delta\psi = \frac{d\psi_1}{dP}M\Delta P + O(M^3). \tag{8}$$

According to (6), the bar elongates under the action of a torque, provided that $\delta_2(P) > 0$. In this case, by virtue of (7) and (8), we have $M\Delta\psi > 0$ for small M and $\Delta P > 0$. This implies that the extra tensile force applied to the bar subjected to a constant torque causes the bar to be twisted in the same direction as that of the torque. If a bar is contracted when being twisted (i.e., $\delta_2 < 0$), then an extra tensile load leads to its untwisting (i.e., $M\Delta\psi < 0$).

3. The resistance of a preloaded cylinder to torsional and tensile–compression strains can be characterized by the following instantaneous rigidities: $E_\psi = \left(\frac{\Delta P}{\Delta\delta}\right)_\psi$ and $E_M = \left(\frac{\Delta P}{\Delta\delta}\right)_M$ are the instantaneous longitudinal rigidities under a constant angular twist and a constant torque, respectively, and $G_\delta = \left(\frac{\Delta M}{\Delta\psi}\right)_\delta$ and $G_P = \left(\frac{\Delta M}{\Delta\psi}\right)_P$ are the instantaneous torsional rigidities under a constant elongation and a constant force, respectively. By virtue of (2) and the assumption that the function $\Pi(\delta, \psi)$ is strictly convex, the following relationships are valid:

$$\frac{E_M}{E_\psi} = \frac{G_P}{G_\delta}, \quad 0 < E_M \le E_\psi, \quad 0 < G_P \le G_\delta.$$

4. In the case of a circular cylinder made of an incompressible isotropic material, the functions u_k (k = 1, 2, 3) in (1), which express a solution to the problem of torsion–tension in terms of the polar coordinates r and ϕ, take the form [6, 7]

$$\begin{aligned}u_1 &= \alpha^{-1/2}r\cos\phi, \quad u_2 = \alpha^{-1/2}r\sin\phi,\\ u_3 &= 0, \quad \alpha = 1 + \delta > 0.\end{aligned} \tag{9}$$

For an incompressible isotropic body, the specific energy W is a function of the strain invariants I_1 and I_2 [7]:

$$\begin{aligned}I_1 = \mathrm{tr}(\mathbf{C}\cdot\mathbf{C}^{\mathrm{T}}), \quad I_2 &= \frac{1}{2}[\mathrm{tr}^2(\mathbf{C}\cdot\mathbf{C}^{\mathrm{T}}) - \mathrm{tr}(\mathbf{C}\cdot\mathbf{C}^{\mathrm{T}})^2],\\ \mathbf{C} &= \frac{\partial X_k}{\partial x_s}\mathbf{i}_s\otimes\mathbf{i}_k,\end{aligned} \tag{10}$$

where $\mathbf{C}$ is the deformation gradient and $\mathbf{i}_s$ are the position unit vectors. In the case of a circular incompressible cylinder with radius a, we obtain, on account of (1), (3), (9), and (10),

$$\begin{aligned}\Pi(\delta, \psi) &= 2\pi\int_0^a W[I_1(r, \delta, \psi), I_2(r, \delta, \psi)]r\,dr,\\ I_1(r, \delta, \psi) &= \alpha^2 + \alpha^{-1}(2 + \psi^2r^2),\\ I_2(r, \delta, \psi) &= 2\alpha + \alpha^{-2}(1 + \psi^2r^2).\end{aligned} \tag{11}$$

Along with using the invariants I_1 and I_2, a widespread method of defining elastic properties for incompressible materials involves representation of the specific energy W in the form of a function of the invariants J_1 and J_2 for the tension tensor $(\mathbf{C}\cdot\mathbf{C}^{\mathrm{T}})^{1/2}$, with

$$J_1 = \mathrm{tr}(\mathbf{C}\cdot\mathbf{C}^{\mathrm{T}})^{1/2}$$

and

$$J_2 = \frac{1}{2}[\mathrm{tr}^2(\mathbf{C}\cdot\mathbf{C}^{\mathrm{T}})^{1/2} - \mathrm{tr}(\mathbf{C}\cdot\mathbf{C}^{\mathrm{T}})].$$

Using (1), (9), and the formulas obtained in [8], we arrive at

$$\begin{aligned}J_1 &= \alpha^{-1/2} + \sqrt{(\alpha^{-1/2} + \alpha)^2 + \alpha^{-1}\psi^2r^2},\\ J_2 &= \alpha^{1/2} + \sqrt{(\alpha^{1/2} + \alpha^{-1})^2 + \alpha^{-2}\psi^2r^2}.\end{aligned} \tag{12}$$

As follows from (2), (11), and (12), the longitudinal force P that must be applied to a twisted continuous cir-

cular cylinder in order for its length to remain constant is given by the following equivalent expressions:

$$P(0, \psi) = -2\pi\psi^2 \int_0^a \left(\frac{\partial W}{\partial I_1} + 2\frac{\partial W}{\partial I_2}\right) r^3 dr, \tag{13}$$

$$P(0, \psi) = -\pi \int_0^a \left[\left(1 - \frac{2 - \psi^2 r^2}{\sqrt{4 + \psi^2 r^2}}\right)\frac{\partial W}{\partial J_1} + \left(\frac{2 + 2\psi^2 r^2}{\sqrt{4 + \psi^2 r^2}} - 1\right)\frac{\partial W}{\partial J_2}\right] r dr. \tag{14}$$

As is known [5, 7], the strong-ellipticity condition for the equilibrium equations for a nonlinear elastic medium represents a constrain imposed on the specific energy taking the form (in the case of an incompressible material)

$$\frac{d^2}{d\eta^2} W(\mathbf{C} + \eta \mathbf{C} \cdot \mathbf{a} \otimes \mathbf{b})\Big|_{\eta = 0} > 0, \tag{15}$$

where **a** and **b** are arbitrary nonzero mutually orthogonal vectors. Using (13), (14), and the results of paper [9], which contain the satisfiability criteria for the strong-ellipticity condition, we come to the following theorem.

Theorem. *If the specific strain energy W of an isotropic incompressible material satisfies the strong-ellipticity condition* (15) *and is a function of only one of the invariants I_1 and I_2 or one of the invariants J_1 and J_2, then the longitudinal force P that must be applied to a twisted continuous circular cylinder in order for its length to remain constant is negative for all values of $\psi \neq 0$.*

The appearance of a compressive longitudinal force under the torsion of a cylinder, provided that axial displacements of its faces are precluded, evidently implies that the length of the same cylinder will increase under free torsion when $P = 0$. It is worth noting that, for the materials mentioned in the hypothesis of the theorem, this general conclusion on the sign of the Poynting effect is concerned with only circular cylinders. Particular examples [2] indicate that the length of a bar subjected to free torsion could decrease if its cross section appreciably differs from a circle.

5. According to (3) and (9), in the case of a non-Hookean material [7] described by the strain energy $W = \frac{1}{2}\mu(I_1 - 3)$ (where μ is the shear modulus), the specific potential energy of a circular cylinder is given by

$$\Pi(\delta, \psi) = \frac{\pi\mu a^2}{4}\left[2\left(\alpha^2 + \frac{2}{\alpha} - 3\right) + \frac{\psi_*^2}{\alpha}\right], \quad \psi_* \equiv \psi a. \tag{16}$$

The strict-convexity condition for function (16) is satisfied for the parameters α and ψ obeying the inequality $\alpha > 0$, which is valid for arbitrary torsion–tensile deformation of the cylinder. From (2) and (16), we have

$$P_* = \frac{\alpha^3 - 1}{\alpha^2} - \left(\frac{\psi_*}{2\alpha}\right)^2, \quad M_* = \frac{\psi_*}{2\alpha}, \quad P_* \equiv \frac{P}{\pi\mu a^2}, \quad M_* \equiv \frac{M}{\pi\mu a^3}. \tag{17}$$

Resolving relationship (17) with respect to α and ψ_*, and assuming that $P_* + M_*^2 > -3/\sqrt[3]{4}$, we obtain the explicit expressions for both the longitudinal elongation and the angular twist in terms of the longitudinal force and torque:

$$\delta = t + \left(\frac{1}{2} + t^3 + \sqrt{\frac{1}{4} + t^3}\right)^{1/3} + t^2\left(\frac{1}{2} + t^3 + \sqrt{\frac{1}{4} + t^3}\right)^{-1/3} - 1,$$
$$\psi_* = 2(1 + \delta)M_*, \quad t \equiv \frac{1}{3}(P_* + M_*^2). \tag{18}$$

It is easy to verify that $\delta(t)$ is a monotonically increasing function. It is immediately seen from formulas (18) that the extension δ and the angular twist ψ monotonically increase with the torque and the longitudinal force, respectively, provided that either the longitudinal force or the torque remains constant (the direct and inverse Poynting effects).

ACKNOWLEDGMENTS

This work was supported by the Russian Foundation for Basic Research, project no. 99-01-01017.

REFERENCES

1. L. M. Zubov, Dokl. Akad. Nauk SSSR **270**, 827 (1983) [Sov. Phys. Dokl. **28**, 512 (1983)].
2. L. M. Zubov and L. U. Bogachkova, Trans. ASME, J. Appl. Mech. **62** (2), 373 (1995).
3. J. H. Poynting, Proc. R. Soc. London, Ser. A **82**, 546 (1909).
4. J. F. Bell, *Experimental Foundations of Solid Mechanics* (Springer, Berlin, 1973; Nauka, Moscow, 1984), Part 2.
5. C. Truesdell, *First Course in Rational Continuum Mechanics* (John Hopkins Univ., Baltimore, 1972; Mir, Moscow, 1975).
6. R. S. Rivlin, Philos. Trans. R. Soc. London, Ser. A **242**, 173 (1949).
7. A. I. Lur'e, *Nonlinear Theory of Elasticity* (Nauka, Moscow, 1980).
8. L. M. Zubov and A. N. Rudev, Dokl. Akad. Nauk **351**, 188 (1996) [Phys. Dokl. **41**, 544 (1996)].
9. L. M. Zubov and A. N. Rudev, Izv. Akad. Nauk, Mekh. Tverd. Tela, No. 6, 21 (1994).

Translated by V. Chechin

Doklady Physics, Vol. 46, No. 9, 2001, pp. 678–680. Translated from Doklady Akademii Nauk, Vol. 380, No. 3, 2001, pp. 346–348.

MECHANICS

Nonexponential Atmosphere and Noncanonical Probability Distributions

Academician V. V. Kozlov

Received April 6, 2001

1. THE ATMOSPHERE IN THERMAL EQUILIBRIUM

It is well known that the density of a column of perfect gas in thermal equilibrium in a field of gravity force decreases with altitude according to the exponential law

$$\rho(z) = \rho_0 \exp\left(-\frac{mgz}{k\tau}\right). \quad (1)$$

Here, m is the mass of gas particles, g is gravitational acceleration, k is the Boltzmann constant, and τ is absolute temperature. In the case of thermal equilibrium, the temperature is assumed to be independent of the atmosphere altitude. As was noticed by Sommerfeld [1], "meteorologists sometimes protested against this statement."

Formula (1) is easily derived from the equilibrium condition for an ideal liquid

$$\operatorname{grad} p = \rho F \quad (2)$$

(where p is pressure and F is the density of external forces) with the equation of state for a perfect gas taken into account:

$$p = \frac{k}{m}\rho\tau. \quad (3)$$

On the other hand, relation (1) can be obtained by averaging, with respect to momenta, the Maxwell–Boltzmann–Gibbs formula for the density of the canonical probability distribution $c\exp\left(-\frac{H}{\kappa\tau}\right)$, where c is the normalizing factor, and H is the Hamiltonian of a particle placed into the gravitational field. After averaging, we obtain the altitude distribution density for gas particles, which turns out to be proportional to the exponential function in formula (1). This derivation of formula (1), which was obtained for the first time by Maxwell, is considered to be one of the first achievements of equilibrium statistical mechanics.

We recall that even Loschmidt (see monograph [2]) has published critical remarks with respect to statements of Maxwell (including those based on the kinetic theory). In addition, in well-known steady-state models, e.g., in the International Standard Model, the Earth's atmosphere decreases with the altitude according to a nonexponential law, and the temperature depends considerably on the altitude of the observation point.

Even more significant problems arise, however, under the natural assumption that the Earth has a spherical shape with a spherically symmetric mass distribution. It turns out that the Earth cannot have an atmosphere with a finite mass and a constant temperature. Indeed, let M be the mass of the Earth, R its radius, γ the gravitational constant, and r the distances between gas particles and the Earth's center. Solving the system of equations (2), (3) for the case of the gravitational attraction, we obtain the formula

$$\rho(r) = c\exp\frac{mG}{k\tau r}, \quad c = \text{const} > 0, \quad G = \gamma M. \quad (4)$$

Since $\rho(r) \longrightarrow c > 0$ as $r \longrightarrow \infty$, the mass of the atmosphere

$$4\pi\int_R^\infty r^2\rho(r)dr \quad (5)$$

is also infinite. We can complicate the problem by taking into account the mutual attraction of atmospheric particles. In this case, the density at a constant temperature is found as the solution to the integro-differential equation

$$\frac{k\tau}{m}\rho' r^2 = -\gamma\left(M + 4\pi\int_R^\infty x^2\rho(x)dx\right)\rho.$$

This equation is simply reduced to the nonautonomous differential equation of the second order. The solution, which we are interested in, has the following asymptotic behavior:

$$\rho(r) = \frac{\alpha}{r^2} + o\left(\frac{1}{r^2}\right), \quad \alpha = \frac{k\tau}{2\pi m\gamma}.$$

However, in this case, the integral (5) also diverges.

Moscow State University,
Vorob'evy gory, Moscow, 119899 Russia

1028-3358/01/4609-0678$21.00

It is worth noting that relationship (4) can be formally derived from the canonical distribution for the Newtonian attraction using the procedure of averaging with respect to momenta. By virtue of the divergence, however, no probabilistic measure can be associated with this density in phase space.

Assuming τ to be the known function of z, we should change formula (1) according to Eqs. (2), (3) by the relationship

$$\rho(z) = \frac{c}{\tau(z)}\exp\left[-\frac{mg}{k}\int_0^z \frac{dx}{\tau(x)}\right], \quad c = \rho(0)\tau(0). \quad (6)$$

In particular, if the temperature linearly decreases with the altitude z, then the atmosphere is in a steady state (of course, provided that the temperature of the Earth's surface is constant). Indeed, the function $\tau(z)$ is harmonic. Therefore, (in accordance with the Fourier law) the temperature field does not vary with time.

If $\tau = \tau_0(1 - \varepsilon z)$, $0 \le z \le \frac{1}{\varepsilon}$, $\tau_0 = \tau(0)$ then formula (6) acquires the form

$$\rho(z) = \rho_0(1 - \varepsilon z)^{\frac{mg}{k\tau_0\varepsilon} - 1}. \quad (7)$$

In the problem on the equilibrium of the atmosphere in the Newtonian gravitational field, the harmonic functions have the form $\frac{a}{r} + b$. Assuming, e.g., $\tau = \frac{a}{r}$, where $a = k\tau(R)$, we have

$$\rho(r) = cr\left(\frac{r}{R}\right)^{-\frac{mG}{ka}}, \quad c = \text{const} > 0. \quad (8)$$

The integral (5) converges in the case when the condition $\frac{mG}{ka} > 4$ holds. This is certainly true, provided that the temperature of the Earth's surface is not high.

The goal of the present paper is the application of methods of statistical mechanics for deriving formulas similar to (6)–(8) for density. In this case, however, we should change the canonical probability distribution in phase space for other distributions whose densities depend only on the total energy.

2. NONCANONICAL DISTRIBUTIONS

Let $M = \{x\}$ be a configuration space of a mechanical system with n degrees of freedom, $P = T^*M$ its phase space, and

$$H = \frac{1}{2}\sum a_{ij}p_ip_j + V(x)$$

the Hamiltonian function. Here, $p_1, \ldots, p_n$ are canonical momenta conjugate to coordinates $x_1, \ldots, x_n$, and V is the force-field potential.

Let $g: M \to \mathbb{R}$ be the nonnegative function determining the probabilistic measure on M:

$$\int_M g(x)d^nx = 1.$$

Following Gibbs, we write out the probability density distribution on P in the form $f(\beta H)$, where $f(\cdot)$ is the nonnegative function of a single variable and β is a parameter whose dimension is inverse with respect to energy.

Averaging the density f over momenta, we arrive at the integral equation

$$\int_{\mathbb{R}^n} f(\beta H)d^np = g(x). \quad (9)$$

The function g is considered to be given, while f should be determined.

At each point $x \in M$, the kinetic energy can be reduced to the quadratic sum by means of the linear change $p = Cy$:

$$(Ap, p) = (y, y), \quad A = \|a_{ij}\|.$$

Passing to the spherical coordinates in $\mathbb{R}^n = \{y\}$, we transform equation (9) to the form

$$\int_0^\infty r^{n-1}\left[\beta\left(\frac{r^2}{2} + V\right)\right]dr = c\sqrt{|A|}g, \quad (10)$$

where $c = \frac{\Gamma(n/2)}{2\pi^{(n/2)}}$. It follows, then, that $\sqrt{|A|}\,g$ is a function of the potential V. We take, for the sake of brevity, that

$$\rho(\beta V) = c\beta\left(\frac{\beta}{2}\right)^{\frac{n-2}{2}}\sqrt{|A|}g.$$

Then, from Eq. (10), we obtain for the function f the integral Volterra equation of the first order

$$\int_\xi^\infty (\zeta - \xi)^{\frac{n-2}{2}} f(\zeta)d\zeta = \rho(\xi). \quad (11)$$

The insignificant difference from the classical case consists in the fact that the integral in Eq. (11) is improper.

The form of the solution to Eq. (11) depends on the evenness of the dimension n. Let n be even and equal to $2s + 2$ ($s \ge 0$). Then,

$$f(\xi) = \frac{(-1)^{s+1}}{(s+1)!}\frac{d^{s+1}}{d\xi^{s+1}}\rho(\xi). \quad (12)$$

In this case, of course, the $(s + 1)$th derivative of the function $\rho(\xi)$ must decrease sufficiently rapidly as $\xi \longrightarrow \infty$ in order to provide the convergence of the improper integral in the left-hand side of Eq. (11).

For an odd n, after several operations of differentiation with respect to ξ, Eq. (11) is reduced to an Abelian-type integral equation so that we can use the classical Abelian formula [3]. For example, in the case of $n = 1$,

$$f(\xi) = \frac{1}{\pi}\frac{d}{d\xi}\int_{\xi}^{\infty}\frac{\rho(u)du}{\sqrt{u-\xi}}.$$

For this formula to be correct, it is necessary to have the convergence of the improper integral and its continuous differentiability with respect to the parameter ξ.

3. APPLICATION OF THE RESULTS TO THE FINITE ATMOSPHERE

The solution to Eq. (11) acquires an especially simple form for $n = 2$ and, hence, $f = -\rho'$ [see formula (12) for $s = 0$]. Using relationship (7) for the density of the atmospheric column, we arrive at the formula

$$f(\beta H) = c\left(1 - \frac{\varepsilon H}{mg}\right)^{\frac{mg}{k\tau_0\varepsilon} - 2}. \qquad (13)$$

Here, τ_0 corresponds to the temperature near the Earth's surface, c is the normalizing factor, and $H = \frac{y_1^2 + y_2^2}{2m} + mgz$ is the Hamiltonian. It is clear that $0 \le H \le \frac{mg}{\varepsilon}$. The multiplier $\frac{\varepsilon}{mg}$ plays the role of the parameter β.

Since $\tau = \tau_0(1 - \varepsilon z)$, the temperature is independent of the altitude as $\varepsilon \longrightarrow 0$. Therefore, formula (13) transforms into the classical Maxwell–Boltzmann–Gibbs distribution

$$f = c\exp\left(-\frac{H}{k\tau}\right).$$

Thus, formula (12) presents an example of a probability distribution that differs little from the canonical distribution at small values of the parameter ε. The theory of these distributions for Hamiltonian systems with a finite number of degrees of freedom is discussed in [4].

We now analyze the form of equations of state and the dependence of the energy on thermodynamic parameters for a rarified gas obeying distribution (13). To do this, we consider a small closed plane vessel disposed in the vertical plane $\mathbb{R}^2 = \{x, z\}$ with small dimensions that are compared to the altitude z. Let v be the vessel volume (to be more precise, its area). The normalizing factor c in formula (13) can be found from the equality

$$\iint f(\beta H)d^2y d\sigma = 1,$$

where $d\sigma$ is an area element in the vertical plane. From this formula, we obtain

$$c = \frac{2\pi v m^2 g(1-\varepsilon z)^{\alpha-1}}{\varepsilon(\alpha-1)} \text{ and } \alpha = \frac{mg}{k\tau_0\varepsilon}. \qquad (14)$$

Furthermore, the energy of the gas placed in the vessel is determined as the average value of the Hamiltonian

$$N\iint Hf d^2y d\sigma,$$

where N is the number of particles in the vessel.

From relationships (13) and (14), we obtain the formula

$$E = Nk\tau_0(1-\varepsilon z) + Mgz. \qquad (15)$$

Here, $M = Nm$ is the mass of the gas occupying the vessel. The first term in formula (15) has the form $Nk\tau$, where τ is the temperature of the gas in the vessel. This is the internal energy of the perfect gas being determined by the motion of its molecules.

In order to derive the equation of state, we should employ the well-known relationship

$$\Lambda = -M\iint\frac{\partial H}{\partial\lambda}f d^2y d\sigma.$$

Here, λ is the thermodynamic parameter and Λ is the corresponding generalized force. In our case, λ is the gas volume v, while Λ is pressure p. Since the dependence of the Hamiltonian on the volume is not given explicitly, in order to calculate pressure it is necessary to transform the right-hand side of relationship (16). In doing so, we reduce it by calculating the derivative (with respect to v) of a certain multiple integral. Employing these relationships (14), we arrive at the equation of state

$$pv = Nk\tau_0(1-\varepsilon z).$$

With regard to the accepted altitude dependence of temperature, this equation, apparently, is equivalent to the equation of state (3) for perfect gas.

ACKNOWLEDGMENTS

This work was supported by the Russian Foundation for Basic Research, project no. 99-01-0196, and by the INTAS grant no. 00-15-96146 for Leading Scientific Schools.

REFERENCES

1. A. Sommerfeld, *Thermodynamik und Statistik* (Wisbaden, 1952; Inostrannaya Literatura, Moscow, 1955).
2. L. Boltzmann, *Selected Papers* (Nauka, Moscow, 1984).
3. F. G. Tricomi, *Integral Equations* (Interscience, New York, 1957; Inostrannaya Literatura, Moscow, 1960).
4. V. V. Kozlov, Regul. Chaotic Dyn. **4** (2), 44 (1999).

Translated by G. Merzon

Doklady Physics, Vol. 46, No. 9, 2001, pp. 681–686. Translated from Doklady Akademii Nauk, Vol. 380, No. 3, 2001, pp. 349–354.

MECHANICS

An Explicit Solution to the Mixed Problem of Stationary Incoherent Thermoelasticity for a Truncated Circular Hollow Cone

G. Ya. Popov

Presented by Academician A.Yu. Ishlinskiĭ March 14, 2001

Received March 22, 2001

1. Allowing for the action of a temperature field $T(r, \theta, \varphi)$, we study the stressed state of an elastic body filling the region described in the spherical system of coordinates by the relationships:

$$a_0 \le r \le a_1, \quad \omega_0 \le \theta \le \omega_1, \quad -\pi \le \varphi < \pi.$$

It is assumed that the sliding-attachment condition is satisfied on the conical surfaces $\theta = \omega_i$, $i = 0, 1$; i.e.,

$$u_\theta(r, \omega_i, \varphi) = 0, \quad \tau_{\theta r}(r, \omega_i, \varphi) = \tau_{\theta\varphi}(r, \omega_i, \varphi) = 0, \quad i = 0, 1, \tag{1}$$

and that they are thermally insulated; i.e.,

$$\left.\frac{\partial T(r, \theta, \varphi)}{\partial \theta}\right|_{\theta = \omega_i} = 0, \quad i = 0, 1. \tag{2}$$

On the spherical surfaces $r = a_i$, $i = 0, 1$, the boundary conditions can be arbitrary, but for the sake of certainty, we will restrict our consideration by the following conditions:

$$\tau_{\theta r}(a_i, \theta, \varphi) = \tau_{r\varphi}(a_i, \theta, \varphi) = 0, \quad i = 0, 1,$$
$$\sigma_r(a_0, \theta, \varphi) = T(a_0, \theta, \varphi) = 0, \tag{3}$$
$$\sigma_r(a_1, \theta, \varphi) = -p(\theta, \varphi), \quad T(a_1, \theta, \varphi) = q(\theta, \varphi).$$

Taking into account the formula [1]

$$2\tau_{\theta r} = 2\tau_{r\theta} = \frac{2G}{r}\left[r^2\frac{\partial}{\partial r}\left(\frac{u_\theta}{r}\right) + \frac{\partial u_r}{\partial \theta}\right], \tag{4}$$

we can see that the second condition of (1) is satisfied if

$$\left.\frac{\partial u_r}{\partial \theta}\right|_{\theta = \omega_i} = 0, \quad i = 0, 1. \tag{5}$$

2. For solving the formulated problem, the thermoelasticity equations are preliminarily transformed. We introduce the designations for the displacements:

$$2Gu_r(r, \theta, \varphi) = u(r, \theta, \varphi),$$
$$2Gu_\theta(r, \theta, \varphi) = V(r, \theta, \varphi), \tag{6}$$
$$2Gu_\varphi(r, \theta, \varphi) = W(r, \theta, \varphi).$$

Instead of the desired functions, their Fourier transforms with respect to the polar angle are introduced:

$$\begin{Vmatrix} u_n & V_n \\ W_n & T_n \end{Vmatrix} = \frac{1}{2\pi}\int_{-\pi}^{\pi}\begin{Vmatrix} u(r, \theta, \varphi) & V(r, \theta, \varphi) \\ W(r, \theta, \varphi) & T(r, \theta, \varphi) \end{Vmatrix} e^{-in\varphi}d\varphi. \tag{7}$$

In this case, the thermoelasticity equations in the spherical system of coordinates can be represented in the form [1, 2]

$$\Delta_n u_n - 2u_n - 2\operatorname{cosec}\theta(V_n\sin\theta)^{\cdot} - 2in\operatorname{cosec}\theta W_n + \frac{1}{1-2\mu}\left\{r^2\left[\frac{1}{r^2}(r^2u_n)'\right] + r^2\left[\frac{(V_n\sin\theta)^{\cdot}}{r\sin\theta}\right]' + \frac{r^2in}{\sin\theta}\left(\frac{W_n}{r}\right)'\right\} = \alpha_\mu r^2 T_n', \tag{8}$$

$$\Delta_n V_n + 2u_n^{\cdot} - \operatorname{cosec}^2\theta V_n - 2in\operatorname{cosec}\theta\cot\theta W_n + \frac{1}{1-2\mu}\left[\frac{(r^2u_n)'}{r} + \frac{(V_n\sin\theta)^{\cdot}}{\sin\theta} + inW_n\right]^{\cdot} = \alpha_\mu r T_n^{\cdot},$$

$$\Delta_n W_n + 2in\operatorname{cosec}\theta u_n - \operatorname{cosec}^2\theta W_n + 2in\operatorname{cosec}\theta\cot\theta V_n + \frac{in}{1-2\mu}\left[\frac{(r^2u_n)'}{r} + \frac{(V_n\sin\theta)^{\cdot}}{\sin\theta} + \frac{in}{\sin\theta}W_n\right] = \frac{\alpha_\mu inr}{\sin\theta}T_n, \tag{9}$$

Mechnikov University,
ul. Petra Velikogo 2, Odessa, 270100 Ukraine

1028-3358/01/4609-0681$21.00

$$\Delta_n T_n(r, \theta) = 0.$$

Here, the signs prime and dot signify the derivatives with respect to r and θ, respectively;

$$\Delta_n f(r, \theta) = (r^2 f')' - \nabla_n f,$$
$$\nabla_n f(r, \theta) = \frac{n^2}{\sin^2\theta} f - \frac{(\sin\theta f^{\cdot})^{\cdot}}{\sin\theta}; \quad (10)$$

$\alpha_\mu = (1 - 2\mu)^{-1} G(1 + 4\mu)\alpha_T$; and μ, G, and α_T are Poisson's ratio, shear modulus, and expansion coefficient, respectively.

As in [3], we introduce the auxiliary functions to simplify Eqs. (8):

$$\begin{Vmatrix} Z_n(r, \theta) \\ Z_n^*(r, \theta) \end{Vmatrix} = \frac{1}{\sin\theta}\left\{ \begin{Vmatrix} \sin\theta V_n(r, \theta) \\ \sin\theta W_n(r, \theta) \end{Vmatrix}^{\cdot} \pm in \begin{Vmatrix} W_n(r, \theta) \\ V_n(r, \theta) \end{Vmatrix} \right\}. \quad (11)$$

This enabled us to transform equation (8) to the form

$$(r^2 u_n')' - \nabla_n u_n - 2u_n - 2Z_n + \frac{1}{1 - 2\mu}\left\{ r^2 \left[\frac{(r^2 u_n)'}{r^2} \right]' + r^2 \left(\frac{Z_n}{r} \right)' \right\} = \alpha_\mu r^2 T_n', \quad (12)$$

$$(r^2 Z_n') - \mu_* \nabla_n Z_n - 2\nabla_n u_n - \frac{1}{1 - 2\mu} \frac{(r^2 \nabla_n u_n)'}{r} = -\alpha_\mu r \nabla_n T_n, \quad (13)$$

$$(r^2 Z_n^{*\prime})' - \nabla_n Z_n^* = 0, \quad (r^2 T_n')' - \nabla_n T_n = 0,$$

where $\mu_* = 2(1 - \mu)(1 - 2\mu)^{-1}$.

If the boundary conditions following from (2) and (5),

$$u_n^{\cdot}(r, \omega_i) = T_n^{\cdot}(r, \omega_i) = Z_n^{\cdot}(r, \omega_i) = 0, \quad (14)$$

are imposed on the solutions to Eqs. (12) and (13), then the integral transformation constructed in [4] should be used to reduce Eqs. (12) and (13) to one-dimensional equations. The kernel of this transformation is the function ($m = |n|$)

$$\varphi_c^m(\theta, \nu) = P_\nu^m(\cos\theta) \frac{dQ_\nu^m(\cos\omega_1)}{d\omega_1} - Q_\nu^m(\cos\theta) \frac{dP_\nu^m(\cos\omega_0)}{d\omega_0}, \quad \nu = \nu_k^c, \quad (15)$$

satisfying the Legendre differential equation

$$-\nabla\varphi(\theta, \nu) + \nu(\nu + 1)\varphi(\theta, \nu) = 0 \quad (16)$$

and the boundary condition

$$[\varphi(\theta, \nu_k^c)]^{\cdot} = 0, \quad \theta = \omega_i, \quad i = 0, 1. \quad (17)$$

Here, the real-valued numbers ν_k^c, $k = 0, 1, 2, \ldots$, are found from the transcendental equation $\Omega_c^m(\nu_k^c) = 0$, $k = 0, 1, 2, \ldots$, where

$$\Omega_c^m(\nu) = \Omega_\nu^{m+1, m+1} + m[\cot\omega_0 \Omega_\nu^{m+1, m} + \cot\omega_1 \Omega_\nu^{m, m+1}] + m^2 \cot\omega_0 \cot\omega_1 \Omega_\nu^{m, m}. \quad (18)$$

The transforms of the desired functions in this integral transformation are determined by the formulas

$$\begin{Vmatrix} u_{nk}(r) \\ Z_{nk}(r) \\ T_{nk}(r) \end{Vmatrix} = \int_{\omega_0}^{\omega_1} \sin\theta \begin{Vmatrix} u_n(r, \theta) \\ Z_n(r, \theta) \\ T_n(r, \theta) \end{Vmatrix} \varphi_c^m(\theta, \nu_k^c) d\theta. \quad (19)$$

According to [4], the inversion of these transforms is given by the formula

$$\begin{Vmatrix} u_n(r, \theta) \\ Z_n(r, \theta) \\ T_n(r, \theta) \end{Vmatrix} = -\sum_{k=0}^{\infty} \begin{Vmatrix} u_{nk}(r) \\ Z_{nk}(r) \\ T_{nk}(r) \end{Vmatrix} \frac{\varphi_c^m(\theta, \nu_k^c)}{\sigma_{m,k}^c(\omega_0, \omega_1)}, \quad \omega_0 \le \theta \le \omega_1, \quad (20)$$

where (with allowance for corrections made in [4])

$$\frac{1}{\sigma_{m,k}^c(\omega_0, \omega_1)} = \frac{2\nu + 1}{\Gamma_m(\nu)} \frac{dQ_\nu^m(\cos\omega_0)}{d\omega_0} \times \left[\frac{dQ_\nu^m(\cos\omega_1)}{d\omega_1} \frac{d}{d\nu} \Omega_c^m(\nu) \right]^{-1},$$

$$\Gamma_m(\nu) = \frac{2^{2m} \Gamma\left(1 + \frac{1}{2}m + \frac{1}{2}\nu\right) \Gamma\left(\frac{1}{2} + \frac{1}{2}m + \frac{1}{2}\nu\right)}{\Gamma\left(1 - \frac{1}{2}m + \frac{1}{2}\nu\right) \Gamma\left(\frac{1}{2} - \frac{1}{2}m + \frac{1}{2}\nu\right)},$$

$$\nu = \nu_k^c.$$

On account of (14), (16), and (17), the transition to transforms (19) reduces Eqs. (12) and (13) to the following one-dimensional equations:

$$[r^2 u_{nk}'(r)]' - [2 + N_\nu \mu_*^{-1}] u_{nk} - \mu_1 \mu_*^{-1} Z_{nk} + \mu_0 \mu_*^{-1} r Z_{nk}' = \alpha_\mu \mu_*^{-1} r^2 T_{nk}'(r),$$
$$[r^2 Z_{nk}'(r)]' - N_\nu \mu_* Z_{nk} - \mu_0 N_\nu u_{nk}' - 2\mu_* N_\nu u_{nk} = -\alpha_\mu r N_\nu T_{nk}'(r), \quad (21)$$

$$[r^2 Z^{*'}_{nk}(r)]' - N_\nu Z^*_{nk}(r) = 0,$$
$$(r^2 T'_{nk})' - N_\nu T_{nk}(r) = 0, \quad \nu = \nu^c_k, \tag{22}$$

where

$$N_\nu = \nu(\nu+1), \quad \mu_0 = (1-2\mu)^{-1},$$
$$\mu_1 = (3-4\mu)(1-2\mu)^{-1}.$$

3. In order to solve Eqs. (21), we introduce the following functions:

$$y_0(r) = u_{nk}(r), \quad y_1(r) = ru'_{nk}(r),$$
$$y_2(r) = Z_{nk}(r), \quad y_3(r) = rZ'_{nk}(r), \tag{23}$$
$$f_1(r) = \alpha_\mu \mu_*^{-1} r^2 T'_{nk}(r), \quad f_3(r) = -\alpha_\mu N_\nu r T_{nk}(r).$$

In this case, with regard to the equalities

$$ry'_0(r) = y_1(r), \quad ry'_2(r) = y_3(r),$$
$$(r^2 u'_{nk})' = r(ru'_{nk})' + ru'_{nk}, \tag{24}$$

equations (21) can be written in the vector form:

$$r\mathbf{y}(r) = P_k \mathbf{y}(r) = \mathbf{f}(r), \quad a_0 < r < a_1, \tag{25}$$

where

$$P_k = \begin{pmatrix} 0 & 1 & 0 & 0 \\ 2+\mu_*^{-1}N_\nu & -1 & \mu_*^{-1}\mu_1 & \mu_*^{-1}\mu_0 \\ 0 & 0 & 0 & 1 \\ \mu_* N_\nu & \mu_0 N_\nu & \mu_* N_\nu & -1 \end{pmatrix},$$
$$\mathbf{y}(r) = \begin{pmatrix} y_0 \\ y_1 \\ y_2 \\ y_3 \end{pmatrix}, \quad \mathbf{f}(r) = \begin{pmatrix} 0 \\ f_1 \\ 0 \\ f_3 \end{pmatrix}, \quad \nu = \nu^c_k. \tag{26}$$

Assuming the right-hand side in (25) to be zero at the interval $(0, \infty)$, we apply the Mellin integral transformation to (25):

$$\begin{Vmatrix} \mathbf{y}_s \\ \mathbf{f}_s \end{Vmatrix} = \int_0^\infty r^{s-1} \begin{Vmatrix} \mathbf{y}(r) \\ \mathbf{f}(r) \end{Vmatrix} dr.$$

As a result, the solution to Eq. (25) is obtained in the form

$$\mathbf{y}(r) = \int_{a_0}^{a_1} \Phi\left(\frac{r}{\rho}\right)\mathbf{f}(\rho)\frac{d\rho}{\rho},$$

where $\Phi\left(\frac{r}{\rho}\right)$ is the fundamental matrix function [6, 7] of Eq. (25), which is determined by the formula

$$\Phi\left(\frac{r}{\rho}\right) = \frac{1}{2\pi i}\int_{\gamma-i\infty}^{\gamma+i\infty} (-sI - P_k)^{-1}\left(\frac{r}{\rho}\right)^{-s} ds$$
$$= \frac{1}{2\pi i}\int_{-\gamma-i\infty}^{-\gamma+i\infty} (\xi I - P_k)^{-1}\left(\frac{r}{\rho}\right)^{\xi} d\xi. \tag{27}$$

For calculating the last integral, we take into account that [5, 6]

$$(\xi I - P_k)^{-1} = Q_4^{-1}(\xi)\Delta^*_k, \quad IQ_4(\xi) = (\xi I - P_k)\Delta^*_k,$$
$$Q_4(\xi) = \det(\xi I - P_k) = \prod_{j=1}^{4}(\xi - \xi_i)$$
$$= \xi^4 + 2\xi^3 - (2N_\nu + 1)\xi^2 - 2(N_\nu + 1)\xi + N_\nu(N_\nu - 2), \tag{28}$$
$$\nu = \nu^c_k.$$

We then find the roots of the characteristic polynomial,

$$\xi_1 = -2 - \nu^c_k, \quad \xi_2 = -1 + \nu^c_k,$$
$$\xi_3 = -\nu^c_k, \quad \xi_4 = 1 + \nu^c_k \tag{29}$$

and represent the characteristic matrix in the form [5, 6]

$$\Delta^*_k(\xi) = \sum_{j=0}^{3} \xi^j \Delta^{(k)}_{3-j}. \tag{30}$$

In doing so, we find the numerical matrices $\Delta^{(k)}_i$, $i = 0, 1, 2, 3$, by substituting (28) into the second equality of (27) and then compare the coefficients by multiplying the powers of ξ. As a result, we have

$$\Delta^{(k)}_0 = I, \quad \Delta^{(k)}_1 = 2I + P_k,$$
$$\Delta^{(k)}_2 = 2P_k + P_k^2 - (2N_\nu + 1)I,$$
$$\Delta^{(k)}_3 = 2P_k^2 + P_k^3 - (2N_\nu + 1)P_k - 2(N_\nu + 1)I,$$
$$\nu = \nu^c_k.$$

Moreover, the quantity $\Delta^{(k)}_3$ can also be determined by the formula

$$\Delta^{(k)}_3 = -N_\nu(N_\nu - 2)P_k^{-1}, \quad \nu = \nu^c_k.$$

This formula can serve as the control of calculations.

Using (28) and (30), we obtain

$$(\xi I - P_k)^{-1} = \sum_{j=0}^{3} \Delta^{(k)}_{3-j}\frac{\xi^j}{Q_4(\xi)}. \tag{31}$$

Substituting (31) into (27), we find

$$\Phi\left(\frac{r}{\rho}\right) = \sum_{j=0}^{3} \Delta_{3-j}^{(k)} V_j\left(\frac{r}{\rho}\right),$$

$$V_j\left(\frac{r}{\rho}\right) = \left(r\frac{d}{dr}\right)^j u\left(\frac{r}{\rho}\right), \quad (32)$$

$$u\left(\frac{r}{\rho}\right) = \frac{1}{2\pi i} \times \int_{-\gamma-i\infty}^{-\gamma+i\infty} \frac{1}{(\xi-\xi_1)(\xi-\xi_2)(\xi-\xi_3)(\xi-\xi_4)}\left(\frac{r}{\rho}\right)^\xi d\xi.$$

Assuming that $-\gamma > -\nu_k^c$ and $\nu_k^c \geq 1$, and using the theorem on residues and the second equality of (32), we obtain

$$V_j\left(\frac{r}{\rho}\right) = V_j(x) = \frac{1}{2(2\nu+1)}\left[\frac{1}{2\nu-1}\begin{cases}(-\nu)^j x^{-\nu}, & x>1\\ (\nu-1)^j x^{\nu-1}, & x<1\end{cases} - \frac{1}{2\nu+3}\begin{cases}(-2-\nu)^j x^{-2-\nu}, & x>1\\ (\nu+1)^j x^{\nu+1}, & x<1\end{cases}\right],$$

$$\nu = \nu_k^c, \quad j = 0, 1, 2, 3.$$

4. Thus, the solutions to both inhomogeneous equation (25) and set (21) are obtained. However, to find the solution to the formulated problem, it is necessary to satisfy boundary conditions (3). We write these conditions as applied to the functions satisfying Eqs. (12) and (13). Conditions (3) in terms of the Fourier transforms with respect to the polar angle can be written in the form

$$\begin{aligned}\tau_{r\theta n}(a_i, \theta) = \tau_{r\varphi n}(a_i, \theta) = 0, \quad i = 0, 1;\\ \sigma_{rn}(a_0, \theta) = T_n(a_0, \theta) = 0;\\ \sigma_{rn}(a_1, \theta) = -p_n(\theta); \quad T_n(a_1, \theta) = q_n(\theta).\end{aligned} \quad (33)$$

By analogy with (11), we introduce combinations of tangential stresses (in terms of their Fourier transforms)

$$\begin{Vmatrix}\tau_n(r, \theta)\\ \tau_n^*(r, \theta)\end{Vmatrix} = \frac{1}{\sin\theta}\left\{\begin{Vmatrix}\sin\theta\tau_{r\theta n}(r, \theta)\\ \sin\theta\tau_{r\varphi n}(r, \theta)\end{Vmatrix}^{\cdot} \pm in\begin{Vmatrix}\tau_{r\varphi n}(r, \theta)\\ \tau_{r\theta n}(r, \theta)\end{Vmatrix}\right\}. \quad (34)$$

Using the Hook law in the spherical system of coordinates [1], we can show that the following formulas are valid:

$$2r\tau_n = rZ_n' - Z_n - \nabla_n u_n, \quad 2r\tau_n^* = rZ_n^{*\prime} - Z_n^*.$$

After applying integral transformation (19), they take the form

$$\begin{aligned}2r\tau_{nk} = rZ_{nk}' - Z_{nk} - N_\nu u_{nk},\\ 2r\tau_{nk}^* = rZ_{nk}^{*\prime} - Z_{nk}^*.\end{aligned} \quad (35)$$

By virtue of (34), fulfilling the conditions (33) leads to the equalities

$$\tau_n(a_i, \theta) = \tau_n^*(a_i, \theta) = 0, \quad i = 0, 1,$$

or, after applying transformation (20),

$$\tau_{nk}(a_i) = \tau_{nk}^*(a_i) = 0, \quad i = 0, 1.$$

By virtue of (35) and designations (23), the last relationships are reduced to the equalities

$$\begin{aligned}N_\nu y_0(a_i) + y_2(a_i) - y_3(a_i) = 0,\\ a_i Z_{nk}^{*\prime}(a_i) - Z_{nk}^*(a_i) = 0, \quad i = 0, 1.\end{aligned} \quad (36)$$

On the basis of the relationship between stresses and displacements in the spherical system of coordinates [1], and with allowance for (6) and (11), we establish that

$$(1-2\mu)r\sigma_{rnk} = 2\mu u_{nk} + (1-\mu)ru_{nk}' + \mu Z_{nk} - (1-2\mu)d_\mu T_{nk}.$$

Therefore, after applying transformation (19) and taking (23) into account, conditions (34) can be written in the form

$$\begin{aligned}2\mu y_0(a_0) + (1-\mu)y_1(a_0) + \mu y_2(a_0) = 0,\\ 2\mu y_0(a_1) + (1-\mu)y_1(a_1) + \mu y_2(a_1) = -(1-2\mu)g_{nk},\end{aligned} \quad (37)$$

$$g_{nk} = a_1 p_{nk} - \alpha_\mu q_{nk},$$

$$T_{nk}(a_0) = 0, \quad T_{nk}(a_1) = q_{nk}. \quad (38)$$

Here, we introduce the matrices A and B and the vector $\boldsymbol{\gamma}$, which are determined by the formulas

$$A = \begin{pmatrix} N_\nu & 0 & 1 & -1\\ 0 & 0 & 0 & 0\\ 2\mu & (1-\mu) & \mu & 0\\ 0 & 0 & 0 & 0\end{pmatrix},$$

$$\boldsymbol{\gamma} = -\begin{pmatrix}0\\ 0\\ 0\\ (1-2\mu)g_{nk}\end{pmatrix}, \quad \nu = \nu_k^c, \quad (39)$$

(The matrix B is obtained from the matrix A by permutation of the lines: the first and the third lines are replaced by the second and the fourth ones, respectively.) Thus, instead of formulas (36) and (37), we may write out

$$U[\mathbf{y}(r)] = A\mathbf{y}(a_0) + B\mathbf{y}(a_1) = \boldsymbol{\gamma}. \quad (40)$$

5. For solving the boundary-value problem (23) and (40), we preliminarily construct a solution to the matrix differential equation

$$rZ'(r) - P_k Z(r) = 0. \quad (41)$$

Using the Cauchy theorem, it is possible to show that the function

$$Z(r) = \frac{1}{2\pi i}\oint_\Gamma (I\xi - P_k)^{-1} r^\xi d\xi = \frac{1}{2\pi i}\oint_\Gamma \frac{\Delta_k^*(\xi)}{Q_4(\xi)} r^\xi d\xi$$

is a solution to Eq. (41) [6, 7], where Γ is a closed contour enveloping all the zeros of $Q_4(\xi)$. Substituting (30) into this formula and taking (29) into account, as was the case when calculating integral (27), we come to the formula

$$\begin{aligned} Z(r) &= \sum_{j=0}^{3} \Delta_{3-j}^{(k)} w_j(r), \quad 2(2\nu+1)w_j(r) \\ &= \frac{(\nu+1)^j r^{\nu+1} - (-1)^j(\nu+2)^j r^{-\nu-2}}{2\nu+3} \\ &+ \frac{(-\nu)^j r^{-\nu} - (\nu-1)^j r^{\nu-1}}{2\nu-1}, \quad \nu = \nu_k^c. \end{aligned} \quad (42)$$

Using the constructed solution to Eq. (41), we find the basis matrix $\Psi(r)$ for the boundary-value problem (25) and (40) [6, 7]. It must be a solution to the matrix boundary-value problem

$$r\Psi'(r) - P_k\Psi(r) = 0, \quad a_0 < r < a_1, \quad U[\Psi(r)] = I.$$

It is easy to verify that its solution is the matrix

$$\Psi(r) = Z(r)(U[Z(r)])^{-1}. \quad (43)$$

It is possible to show [6, 7] that the matrix

$$G(r, \rho) = \Phi\left(\frac{r}{\rho}\right)\rho^{-1} - \Psi(r)U\left[\Phi\left(\frac{r}{\rho}\right)\right] \quad (44)$$

is a Green matrix for the boundary-value problem (25), (40). Therefore, the solution to the boundary-value problem (25) and (40) has the form

$$\mathbf{y}(r) = \int_{a_0}^{a_1} G(r, \rho)\mathbf{f}(\rho)d\rho + \Psi(r)\boldsymbol{\gamma}, \quad a_0 \le r \le a_1. \quad (45)$$

All that remains is to construct the solution to the boundary-value problems (22), (36), and (38). Since the boundary-value problem for $Z_{nk}^*(r)$ is homogeneous, its solution is zero; i.e.,

$$Z_{nk}^*(r) \equiv 0, \quad Z_{nk}^*(r, \theta) \equiv 0. \quad (46)$$

For solving the boundary-value problem for the function $T_{nk}(r)$, it is sufficient to construct the basis set of solutions $\psi_j(r)$, $j = 0, 1$, to this problem [6, 7]:

$$\Delta(a)\psi_0(r) = \left(\frac{a_0}{a_1}\right)^{2\nu+1}\left(\frac{a_0}{r}\right)^{\nu+1} - \left(\frac{a_0}{a_1}\right)^{2\nu+1}\left(\frac{r}{a_0}\right)^{\nu},$$

$$\Delta(a) = 1 - \left(\frac{a_0}{a_1}\right)^{2\nu+1},$$

$$\Delta(a)\psi_1(r) = \left(\frac{r}{a_1}\right)^{\nu} - \left(\frac{a_0}{a_1}\right)^{2\nu+1}\left(\frac{a_1}{r}\right)^{\nu+1}, \quad \nu = \nu_k^c.$$

In this case, the solution to boundary-value problem (21) and (38) takes the form

$$T_{nk}(r) = \psi_1(r)q_{nk}.$$

Thus, all the desired functions of the solvable system of Eqs. (21) and (22) are determined.

6. It remains to determine the functions $V_n(r, \theta)$ and $W_n(r, \theta)$ by using the obtained auxiliary functions $Z_n(r, \theta)$ and $Z_n^*(r, \theta)$. The desired functions must satisfy boundary conditions (1) with allowance for designations (6) and the passage to the Fourier transforms. These can be written in the following form:

$$\begin{aligned} &V_n(r, \omega_i) = 0, \quad r^2[r^{-1}V_n(r, \omega_i)]^{\cdot} + u_n(r, \omega_i) = 0, \\ &W_n^{\cdot}(r, \omega_i) - \cot\omega_i W_n(r, \omega_i) + inV_n(r, \omega_i) = 0, \\ &i = 0, 1. \end{aligned} \quad (47)$$

All these conditions will be satisfied, provided that

$$\begin{aligned} &u_n^{\cdot}(r, \omega_i) = 0, \quad V_n(r, \omega_i) = 0, \\ &W_n^{\cdot}(r, \omega_i) - \cot\omega_i W_n(r, \omega_i) = 0, \quad i = 0, 1. \end{aligned} \quad (48)$$

The first of these conditions has already been satisfied through applying integral transformation (19) to Eq. (21). To satisfy the two remaining conditions of (48), it is necessary to carry out operations allowing the functions $V_n(r, \theta)$ and $W_n(r, \theta)$ to be determined from the known functions $Z_n(r, \theta)$ and $Z_n^*(r, \theta)$. For this purpose, as was shown in [8], it is necessary to solve the equations

$$-\nabla_n \begin{Vmatrix} V_n^*(r, \theta) \\ W_n^*(r, \theta) \end{Vmatrix} = \begin{Vmatrix} \operatorname{cosec}\theta[Z_n(r, \theta)\sin^2\theta]^{\cdot} \\ inZ_n(r, \theta) \end{Vmatrix}. \quad (49)$$

Here, we take into account that (46) is valid, a misprint in [8] is corrected, and the following designations are introduced:

$$\begin{aligned} V_n^*(r, \theta) &= \sin\theta V_n(r, \theta), \\ W_n^*(r, \theta) &= \sin\theta W_n(r, \theta). \end{aligned} \quad (50)$$

To satisfy conditions (48), it is necessary to impose the following boundary conditions on equations (49):

$$V_n^*(r, \omega_i) = 0,$$
$$W_n^{*\cdot}(r, \omega_i) - 2\cot\omega_i W_n^*(r, \omega_i) = 0, \quad i = 0, 1. \tag{51}$$

These conditions dictate the use of the integral transformations [4]

$$\begin{Vmatrix} V_{nk}^*(r) \\ W_{nk}^*(r) \end{Vmatrix} = \int_{\omega_0}^{\omega_1} \sin\theta \begin{Vmatrix} V_n^*(r, \theta)\varphi_a^m(\theta, \nu_k^a) \\ W_n^*(r, \theta)\varphi_b^m(\theta, \nu_k^b) \end{Vmatrix} d\theta \tag{52}$$

for solving differential equations (49). Here, according to [4],

$$\varphi_a^m(\theta, \nu) = P_\nu^m(\cos\theta)Q_\nu^m(\cos\omega_1) - P_\nu^m(\cos\omega_1)Q_\nu^m(\cos\theta), \quad \nu = \nu_k^a,$$
$$\varphi_b^m(\theta, \nu) = P_\nu^m(\cos\theta)l_1^h Q_\nu^m(\cos\theta) - Q_\nu^m(\cos\theta)l_1^h P_\nu^m(\cos\theta), \quad \nu = \nu_k^b, \tag{53}$$

$$l_i^h y(\theta) = y^{\cdot}(\omega_i) + h_i y(\omega_i), \quad i = 0, 1,$$
$$h_i = -2\cot\omega_i. \tag{54}$$

Eigenfunctions (53) will satisfy equation (16) and boundary conditions (51) if the eigenvalues ν_k^a and ν_k^b are found from the transcendental equations

$$\Omega_a^m(\nu_k^a) = 0, \quad \Omega_b^m(\nu_k^b) = 0, \quad k = 0, 1, 2, \ldots,$$

where $\Omega_a^m(\nu) = \Omega_\nu^{m, m}$, and $\Omega_b^m(\nu)$ is obtained from (18) by replacing the factor m (not the superscript) for $m - 1$.

Applying the integral transformations (52) to the equations (49), we obtain

$$V_{nk}^*(r) = \frac{1}{N_\nu}\int_{\omega_0}^{\omega_1} Z_n(r, \theta)\sin^2\theta\varphi_a^m(\theta, \nu)d\theta, \quad \nu = \nu_k^a,$$
$$W_{nk}^*(r) = -\frac{in}{N_\nu}\int_{\omega_0}^{\omega_1} Z_n(r, \theta)\sin\theta\varphi_b^m(\theta, \nu)d\theta, \quad \nu = \nu_k^b.$$

Using the inversion formulas for integral transformations (52) obtained in [4] and taking (50) into account, we find the Fourier transforms for the displacements:

$$\|V_n(r, \theta), W_n(r, \theta)\| = -\frac{1}{\sin\theta}\sum_{k=0}^{\infty}\left\| \frac{V_{nk}^*(r)\varphi_a^m(\theta, \nu_k^a)}{\sigma_{m,k}^a(\omega_0, \omega_1)}, \frac{W_{nk}^*(r)\varphi_b^m(\theta, \nu_k^b)}{\sigma_{m,k}^b(\omega_0, \omega_1)} \right\|, \tag{55}$$

where, according to [4] (with allowance for correcting the misprints in [4]),

$$\frac{1}{\sigma_{m,k}^a(\omega_0, \omega_1)} = \frac{2\nu + 1}{\Gamma_\nu(\nu)}\frac{Q_\nu^m(\cos\omega_0)}{Q_\nu^m(\cos\omega_1)}\frac{d\Omega_a^m(\nu)}{d\nu}, \quad \nu = \nu_k^a,$$
$$\frac{1}{\sigma_{m,k}^b(\omega_0, \omega_1)} = \frac{2\nu + 1}{\Gamma_\nu(\nu)}\frac{l_0^h Q_\nu^m(\cos\theta)}{l_1^h Q_\nu^m(\cos\theta)}\frac{d\Omega_b^m(\nu)}{d\nu}, \quad \nu = \nu_k^b.$$

Formulas (55), together with (20), determine the transforms of the desired displacements and temperature. To determine the originals, it is sufficient to use the inversion formulas for the Fourier transforms. For example,

$$u(r, \theta, \varphi) = 2Gu_\varphi(r, \theta, \varphi) = \sum_{n=-\infty}^{\infty} u_n(r, \theta)e^{in\varphi}.$$

Thus, we obtained an explicit solution to the formulated problem. The method proposed is essentially based on sliding-attachment conditions on the conical surfaces (1). The boundary conditions for temperature can be arbitrary for all boundary surfaces. They can also be arbitrary for elastic displacements and stresses on the spherical surfaces $r = a_i$, $i = 0, 1$.

REFERENCES

1. W. Nowatskiĭ, *Theory of Elasticity* (PWN, Warszawa, 1970; Mir, Moscow, 1975), translated from Polish.
2. A. D. Kovalenko, *Introduction to Thermoelasticity* (Naukova Dumka, Kiev, 1965).
3. G. Ya. Popov, Prikl. Mat. Mekh. **62**, 840 (1998).
4. G. Ya. Popov, Prikl. Mat. Mekh. **64**, 431 (2000).
5. F. R. Gantmacher, *The Theory of Matrices* (Gostekhteorizdat, Moscow, 1954; Chelsea, New York, 1959).
6. G. Ya. Popov, S. A. Abdymanapov, and V. V. Efimov, *Green Functions and Matrices* (Rauan, Almaty, 1999).
7. G. Ya. Popov, *Elastic Stress Concentration near Dies, Cuts, Thin Inclusions and Fastenings* (Nauka, Moscow, 1982).
8. G. Ya. Popov, Dokl. Akad. Nauk **356**, 47 (1997) [Phys. Dokl. **42**, 511 (1997)].

Translated by V. Bukhanov